# NUMERICAL MODELING OF THE

# HALL THRUSTER  DISCHARGE

**Final  report**

**April 1, 2005**

E. Ahedo, F. I. Parra, D. Escobar,
V. Lapuerta, A. Molina, J. Rus

*E.T.S.I. AERONAUTICOS, UNIVERSIDAD POLITÉCNICA
DE MADRID, SPAIN*

| | | | Form Approved OMB No. 0704-0188 |
|---|---|---|---|

# Report Documentation Page

| 1. REPORT DATE **25 APR 2005** | 2. REPORT TYPE **N/A** | 3. DATES COVERED **-** |
|---|---|---|

| 4. TITLE AND SUBTITLE **Numerical Modeling of the Hall Thruster Discharge** | 5a. CONTRACT NUMBER |
|---|---|
| | 5b. GRANT NUMBER |
| | 5c. PROGRAM ELEMENT NUMBER |
| 6. AUTHOR(S) | 5d. PROJECT NUMBER |
| | 5e. TASK NUMBER |
| | 5f. WORK UNIT NUMBER |

| 7. PERFORMING ORGANIZATION NAME(S) AND ADDRESS(ES) **Universidad Politecnica de Madrid ETSI Aeronautics Plaza Cardenal Cisneros Madrid 28040 Spain** | 8. PERFORMING ORGANIZATION REPORT NUMBER |
|---|---|

| 9. SPONSORING/MONITORING AGENCY NAME(S) AND ADDRESS(ES) | 10. SPONSOR/MONITOR'S ACRONYM(S) |
|---|---|
| | 11. SPONSOR/MONITOR'S REPORT NUMBER(S) |

| 12. DISTRIBUTION/AVAILABILITY STATEMENT **Approved for public release, distribution unlimited** |
|---|

| 13. SUPPLEMENTARY NOTES **The original document contains color images.** |
|---|

| 14. ABSTRACT |
|---|

| 15. SUBJECT TERMS |
|---|

| 16. SECURITY CLASSIFICATION OF: | | | 17. LIMITATION OF ABSTRACT | 18. NUMBER OF PAGES | 19a. NAME OF RESPONSIBLE PERSON |
|---|---|---|---|---|---|
| a. REPORT **unclassified** | b. ABSTRACT **unclassified** | c. THIS PAGE **unclassified** | **UU** | **124** | |

The Contractor, UNIVERSIDAD POLITECNICA DE MADRID, hereby declares that, to the best of its knowledge and belief, the technical data delivered herewith under Grant No. FA8655-04-1-3003 is complete, accurate, and complies with all requirements of the contract.

We certify that there were no subject inventions to declare as defined in FAR 52.227-13, during the performance of this contract.

April 1, 2005

Eduardo Ahedo                           Gonzalo de León
Main investigator                       Vice Rector for Research

# FINAL REPORT

## Original statement of work (August 2003)

1. Development of more advanced numerical models of the discharge

   1.1. Development of a time-dependent axial model.

   1.2. Studies with the HPHall hybrid code.

       1.2.1. Update of the code with a new model for the lateral sheaths.

       1.2.2. Comparison of the hybrid and macroscopic codes.

       1.2.3. Discussion of non-stationary and stationary regimes.

       1.2.4. Application of the hybrid code to a real thruster.

2. Advances on the understanding of the discharge physics

   2.1. On the energy balance in the near-plume.

   2.2. Mutual influence of the electron distribution function on the plasma-wall interaction.

   2.3. Influence of the electrical conductivity of the wall on the radial and axial responses.

   2.4. Effects of multiple ionization.

# Modified statement of work (as submitted in the progress report)

1. HPHall-2: A new version of the HPHall hybrid code **(Docs. 1 to 3)**

    1.1.    Improvements on the PIC subcode for heavy species

        1.1.1.  Implementation of ion-neutral collisions.

        1.1.2.  Weighting at the boundaries. Fulfillment of the Bohm condition.

        1.1.3.  Cylindrical effects on weighting algorithms.

        1.1.4.  Computation of temperature (tensors) and other higher order magnitudes

        1.1.5.  Local tests of conservation of particles and energy

        1.1.6.  Implementation of new algorithms/models for particle injection

    1.2.    Improvements on the fluid subcode for electrons

        1.2.1.  Update of the code with a new model for the lateral sheaths.

        1.2.2.  New wall collisionality model

    1.3.    Testing and discussion of HPHall-2

        1.2.1. Analysis of results

        1.2.2. Comparison with the macroscopic code.

        1.2.3. Suggestion of further improvements.

2. Advances on the understanding of the discharge physics

    2.1.    On the energy balance in the near-plume

    2.2.    Parametric studies on control and design parameters **(Doc. 4)**

    2.3.    Influence of the electrical conductivity of the wall on the radial and axial responses **(Doc. 5)**

    2.4.    Studies of the near anode region **(Docs. 6 and 7)**

## Attached documents

1. F. Parra, E. Ahedo, M. Martínez-Sánchez, and J.M. Fife, 'Improvement of the plasma-wall model on a fluid-PIC code of a Hall thruster', in SP-555: 4th Spacecraft Propulsion Conference, Sardinia (Italy), European Space Agency, Noordwijk, The Netherlands (2004)

2. F.I. Parra and E. Ahedo, 'Fulfillment of the Bohm condition on the HPHall fluid-PIC code', paper AIAA 2004-3955, American Institute of Aeronautics and Astronautics, Washington, DC (2004)

3. F. Parra, E. Ahedo, M. Martínez-Sánchez, and J.M. Fife, 'A two-dimensional hybrid code of the Hall thruster discharge', in preparation for J. Applied Physics

4. E. Ahedo and D. Escobar, 'Influence of design and operation parameters on Hall thruster performances', J. Applied Physics, Vol. 96, (2004)

5. E. Ahedo and F.I. Parra, 'A model of the two-stage Hall thruster discharge', to be published in J. Applied Physics.

6. J. Rus and E. Ahedo, 'A no-anode-sheath regime of the Hall thruster discharge', in SP-555: 4th Spacecraft Propulsion Conference, Sardinia (Italy), European Space Agency, Noordwijk, The Netherlands (2004).

7. E. Ahedo, 'On the near anode region of the Hall thruster discharge', paper AIAA 2004-3774, American Institute of Aeronautics and Astronautics, Washington, DC (2004)

## HPHall.v2 code

An electronic version of the code is delivered with this report. The new version is based on the original one received by us from M.Fife and M. Martínez Sánchez. An expertise on running HPHall is required, since no tutorial is included. Questions about this electronic version should be submitted to F. Parra (fparra@mit.edu).

# Summary

The original statement of work was submitted to EOARD in August 2003. The first notification of the approval of the project was received in February 2004 and the Award was signed in March 2004. However, since there were positive expectations on the approval of the project and this required the cooperation of several students (during the academic period), work on the project was initiated in November 2003.

As part of the previous award, F. Parra stayed the summer '03 at MIT learning the use and the intrinsic features of the HPHall code. As a consequence of that analysis and revision, and the experience of J.M Fife and other users at MIT with the code, it was concluded that a larger set of improvements than expected initially in our proposal, should be implemented in the code. In addition, we were aware that HPHall was considered a very useful instrument by AFRL. Therefore, we decided that the development of an improved version of HPHall would become the center of the present project.

This justifies the differences between the original and modified plans of work, included in the previous pages. Part 1 of the modified statement of work explicits all the activities we have carried out in relation to the new HPHall version (called HPHall.v2). The improvements of this new version are summarized in the statement of work and explained in documents 1 to 3 attached to this report.

The development of HPHall.v2 has taking about 2/3 of the total work dedicated to the project. This has implied to renounce to significant advances on other subjects proposed initially, mainly on the macroscopic time-dependent model (1.1), the electron distribution function near the walls (2.2), and the effects of multiple ionization for high discharge potentials (2.4). On the other hand, two new items (2.2 and 2.4) were added to the statement of work.

Part 2 of the proposal was dedicated to theoretical studies of different aspects of Hall thruster physics. No success or results worth to mention was attained on item 2.1. The parametric studies on control and design parameters (item 2.2 and Doc. 4) completed previous work to the level of being published in a major scientific journal. The work on item 2.3 was dedicated to the effects of introducing emissive electrodes inside the thruster chamber. The resulting document 5 completes works initiated in previous projects. Finally, the analysis of the near-anode region (item 2.4 and Docs. 6 and 7) was found necessary in order to close consistently both the hybrid and macroscopic codes at the anodic end of the chamber. Further work on this subject is foreseen.

# IMPROVEMENT OF THE PLASMA-WALL MODEL ON A FLUID-PIC CODE OF A HALL THRUSTER

**Félix I. Parra[1], Eduardo Ahedo[1], Manuel Martínez-Sánchez[2], and John Michael Fife[3]**

[1]E.T.S.I. Aeronáuticos, Universidad Politécnica, 28040 Madrid, Spain
[2]Massachusetts Institute of Technology, Cambridge, USA
[3]Air Force Research Laboratory, Edwards AFB, California, USA

## ABSTRACT

Two issues are discussed. First, a new sheath model that takes into account charge-saturation is implemented in HPHall. Second, the transition between the quasineutral solution and the sheaths at the lateral walls is found to be treated deficiently in the original code. The use of finer meshes yields better solutions but do not solve the problem completely.

Key words: Hall thrusters; particle-in-cell codes; sheaths.

## 1. INTRODUCTION

The HPHall hybrid code started to be developed ten years ago (Fife & Martínez-Sánchez 1995; Fife 1998). HPHall analyzes the two-dimensional (2D) (azimuthal symmetry is assumed) structure of the plasma discharge in a Hall thruster chamber by treating (i) ions and neutrals with particle-in-cell(PIC) plus Montecarlo methods and (ii) electrons with macroscopic equations. Hybrid codes represents a good trade-off between fully macroscopic and fully PIC codes if we take into account (a) the disparate length and time scales of electrons and heavy species, (b) the treatment of complex geometries and magnetic field topographies, and (b) the execution time.

The HPHall has been proved very helpful in the analysis of the response of the SPT-70 and other Hall thrusters. Nonetheless, in order to deliver a valid first version of the code within a reasonable time, some parts of it were deliberately underdeveloped. In addition, important advances on the understanding of the multiple discharge phenomena have been made in the last years, and better or new models of these phenomena are available today. All this has motivated to launch a program to improve (i) the numerical tools and outputs of HPHall and (ii) the underlying physics implemented on it. A lateral goal of the program is the comparison and mutual validation of HPHall and the macroscopic code developed by Ahedo et al. (2003).

In this paper, two specific subjects related to the plasma interaction with the lateral walls are discussed and improved:

1. Implementation of the charge-saturation sheath model developed by Ahedo (2002b).

2. Fulfillment of the Bohm condition at the plasma/sheath transition (Ahedo 2002a).

## 2. HPHALL FUNDAMENTALS

The reader is referred to Fife (1998) for a detailed account of HPHall. In particular, Fig. 3.9 of that work shows the code computation diagram. The geometric mesh and the magnetic field are obtained in a pre-process. Figure 1 shows the first ('coarse') mesh and the magnetic field used in the present work. Parameters correspond to a SPT-70 thruster. In order to better compare with the model of Ahedo et al., the B-field has been assumed to have no axial component ($B_z = 0$) so that B-lines are along the radial direction. For the radial component we take $B_r \propto 1/r$. In this way we are fulfilling $\nabla \cdot \boldsymbol{B} = 0$, but not $\nabla \wedge \boldsymbol{B} = \boldsymbol{0}$.

The PIC and fluid parts of the code are separated. The PIC algorithms yield the motion of ion and neutral macroparticles (about 60.000 and 30.000,
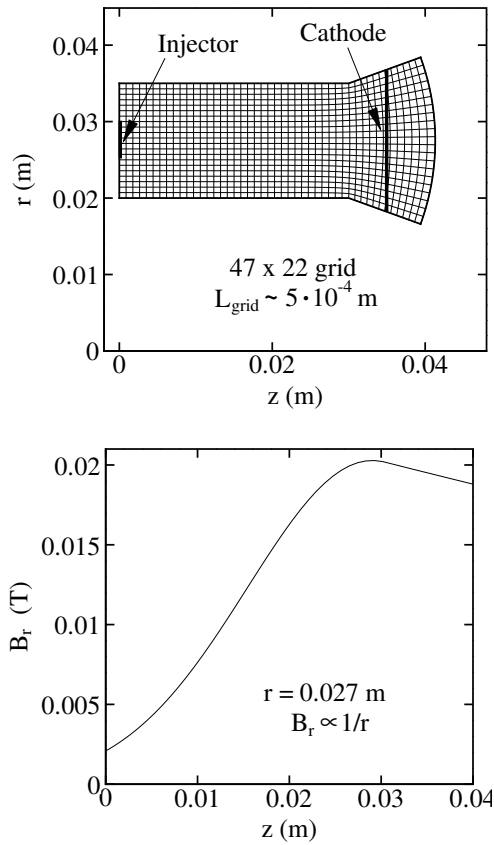
*Figure 1. 'Coarse' mesh and B-field used in this work. For the magnetic field, one has $B_z = 0$ and $B_r(r, z) = B_r(r_0, z)r_0/r$.*

respectively, for the above mesh). This motion is collisionless except for ionization (by electron-neutral impact) and recombination processes at the walls. These are treated with Montecarlo methods. Linear weighting is used to define macroscopic magnitudes (like densities, fluxes, and temperatures) at the mesh nodes.

Electrons dynamics are modelled by 2D macroscopic equations based on a closed-drift, diffusive model. The electron equations are solved by finite element methods. The strong magnetic field introduces a high anisotropy on the electron momentum equations, which leads to a Maxwell-Boltzmann equilibrium along the magnetic lines and a generalized Ohm law in the direction perpendicular to them. Then, the best volume elements to integrate the electron equations have the magnetic lines as boundaries.

The Hall thruster discharge is quasineutral except for very thin Debye sheaths tied to the lateral walls and the anode. The macroscopic modelling of the electrons dynamics makes possible to apply plasma quasineutrality within the code. This avoids to solve Poisson equation for the electrostatic potential, $\phi$, and consequently to use the small time and length scales associated to that equation (i.e. the inverse of plasma frequency and the Debye length). This reduces largely the code execution time.

Because of quasineutrality, the plasma density, $n_e$, is determined by the PIC computations on the ions. Then, the Maxwell-Boltzmann equilibrium law relates $n_e$ and the electron temperature, $T_e$, to the electrostatic potential. The electron energy equation, the Ohm law perpendicular to magnetic lines, and the electrical current conservation are needed to compute $T_e$. (This constitutes the main part of the electron-related part of the code.) The electric field is computed subsequently from $\boldsymbol{E} = -\nabla\phi$ and used in the next time step of the PIC code.

The main inconvenient of using quasineutrality is that the computation domain does not end at the thruster walls but at the transitions to the quasineutral sheaths. This means that (i) sheaths must be solved separately and (ii) wall conditions must be substituted by sheath transition conditions. We will see below that this last point is a rather problematic issue in HPHall.

## 3. PLASMA-WALL INTERACTION FUNDAMENTALS

SPT discharge chambers use ceramic materials. The behavior of the plasma in their vicinity defines the particle and energy losses to them, so a correct modelling is necessary for a valid simulation. In this section we resume the basic features of the plasma-wall interaction as were established recently by Ahedo (2002a,b).

For a dielectric material, the plasma structure near the wall is a consequence of the local zero-current condition. The disparate electron and ion random fluxes make impossible to satisfy that condition by the quasineutral plasma so a non-neutral sheath is formed, Fig. 2. In a two-scale asymptotic analysis, based on (Debye length) $\ll$ (channel width), the plasma sheath transition (point Q) is *perfectly defined* and the quasineutral and sheath regions are solved independently. The sheath is planar and collisionless, and the sheath potential drop, $\phi_{WQ}$, is self-adjusted in order to satisfy the zero-current condition. The analyses of the quasineutral and sheath regions demonstrate that the transition between the two regions is possible only if the plasma satisfies the (sonic) Bohm condition. The functional form of this condition depends on the particular plasma characteristics. For a simple two
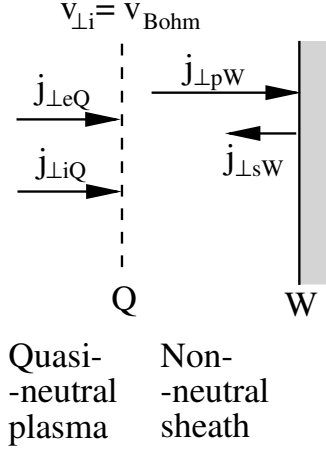
$v_{\perp i} = v_{Bohm}$

$j_{\perp eQ}$   $j_{\perp pW}$

$j_{\perp iQ}$   $j_{\perp sW}$

Q   W

Quasi-
-neutral
plasma

Non-
-neutral
sheath

*Figure 2. Sketch of the presheath/sheath model. Q is the sheath transition, and W is the wall. p and s represent primary and secondary electrons in the sheath. e represents electrons in the presheath. $j_{\perp}$ are currents perpendicular to the wall.*

species plasma, the Bohm condition states that the ion (macroscopic) velocity perpendicular to the wall (and sheath) is sonic,

$$v_{\perp iQ} = v_{Bohm} = \sqrt{\frac{kT_{eQ} + kT_{iQ}}{m_i}}. \qquad (1)$$

For dielectric materials, such as Boron Nitride composites used in Hall thrusters, secondary electron emission (SEE) by electron impact is high. SEE can modify largely the sheath structure (Hobbs & Wesson 1967). The account for SEE within a consistent sheath/presheath/sheath model for a plasma flowing between two walls was achieved by Ahedo (2002b). A central idea of the model was to distinguish between primary ($p$) and secondary ($s$) electrons within the sheath, but to consider a single electron population ($e$) in the quasineutral or presheath region. The temperatures of populations $p$ and $e$ in the model differ up to a 15% for high SEE. The presence of secondary electrons has a small impact within the presheath structure.

When SEE is present, the zero-current condition reads

$$g_{\perp iW} = g_{\perp iQ} = g_{\perp pW} + g_{\perp sW},$$
$$g_{\perp sW} = -\delta_w(T_p)g_{\perp pW}, \qquad (2)$$

where $g_{\perp}$ represent particle fluxes perpendicular to the walls, and $\delta_w(T_p)$ is the effective SEE yield,

which depends, at least, on the temperature of primary electrons and the wall material. For a Maxwellian population, the primary flux is

$$g_{\perp pW} = n_{pQ} \exp\left(-\frac{e\phi_{WQ}}{kT_p}\right)\sqrt{\frac{kT_p}{2\pi m_e}} \qquad (3)$$

and applying Eq. (2) the sheath potential drop satisfies

$$\frac{e\phi_{WQ}}{kT_p} = \ln\sqrt{\frac{m_i}{2\pi m_e}} + \ln(1-\delta_w) + \ln\frac{n_{pQ}\sqrt{kT_p/m_i}}{n_{eQ}v_{\perp iQ}}; \qquad (4)$$

the first term on the right-hand side is 5.28, and the last term is practically zero, even for $\delta_w \sim 1$. As $\delta_w$ increases, $e\phi_{WQ}/kT_p$ decreases and the electric field at the wall decreases too. For $\delta_w = \delta_w^* = 0.983$ (and xenon), this electric field becomes zero, that is, the charge saturation limit (CSL) is reached. The potential drop in the CSL is $e\phi_{WQ}/kT_p \simeq 1.02$ and the *p-e* temperature ratio is $T_p/T_e \simeq 0.86$ (Ahedo 2002b). For higher values of $\delta_w$ we are within the charge saturation regime (CSR). A small potential well (of the order of the wall temperature, $T_w$) is formed in order to turn back part of the secondary emission. As a consequence, the secondary flux that crosses the sheath and reaches the presheath continues to be $j_{\perp sQ} = -\delta_w^* j_{\perp pW}$. If $T_w \ll T_p$, the potential well is negligible and the CSL dimensionless solution represents the whole CSR.

The electron energy flux into the wall is

$$q_{\perp pW} = g_{\perp pW}2T_p = \frac{g_{\perp iQ}}{1-\delta_w}2T_p \qquad (5)$$

For a quasineutral code, it is more important the electron energy flux into the sheath (at point Q):

$$q_{\perp eQ} = q_{\perp pQ} + q_{\perp sQ} = g_{\perp iQ}\left(\frac{2T_p}{1-\delta_w} + e\phi_{WQ}\right) \qquad (6)$$

Here the ion (and electron) flux into the sheath, $g_{\perp iQ}$, depends almost exclusively on the plasma evolution within the quasineutral region, whereas the energy losses per electron, $q_{\perp eQ}/g_{\perp iQ}$, depend on the sheath physics, that is on the SEE.

SEE depends on the specific material. In general the experimental data provides the SEE yield for a monoenergetic beam of energy $E$. At present, there are no accurate measurements of $\delta_w(E)$ for low beam energies. This justifies that existing models opt for either potential laws: $\delta_w(E) = (E/E_1)^B$, or linear laws, $\delta_w(E) = \delta_0 + (1-\delta_0)E/E_1$; in both cases $E_1$ is the energy for 100% SEE. Here, we will use the potential law implemented in the HPHall. For a Maxwellian distribution of primary electrons, the effective SEE yield is obtained from averaging
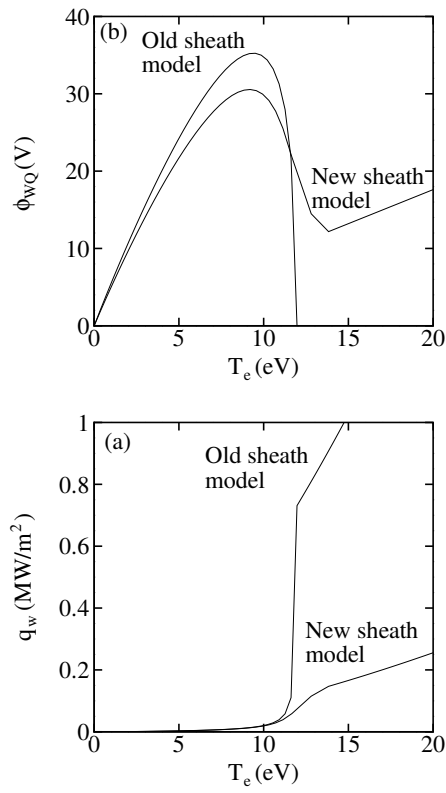
*Figure 3. Comparison between the old and new sheath models for a ceramic material with $E_1 = 21.68$ eV and $B = 0.576$. (a) Sheath potential drop. (b) Electron energy flux into the sheath for $n_{eQ} = 2 \cdot 10^{17}$ m$^{-3}$.*

$\delta_w(E)$ over the different energies. This yields (Fife et al. 1997)

$$\delta_w(T_p) = (T_p/T_1)^B, \qquad (7)$$

with $T_1 = E_1/\Gamma(2 + B)^{1/B}$. For usual ceramics, it is $E_1 \sim 15 - 50$eV.

## 4. IMPLEMENTATION OF A NEW SHEATH MODEL

When HPHall was developed, the charge saturation of the sheath was unknown to researchers on Hall thruster physics. It was first noted to this community by Jolivet & Roussel (2000). Previous models (Morozov 1991; Fife et al. 1997) considered that the sheath vanishes for SEE yields close to 100%. In particular, in the model that was implemented in HPHall the electron-repelling sheath vanishes for $\delta_w \simeq 0.997$. No-sheath and ion-repelling sheath regimes follow for larger $\delta_w$. Since $T_w \ll T_e$, the
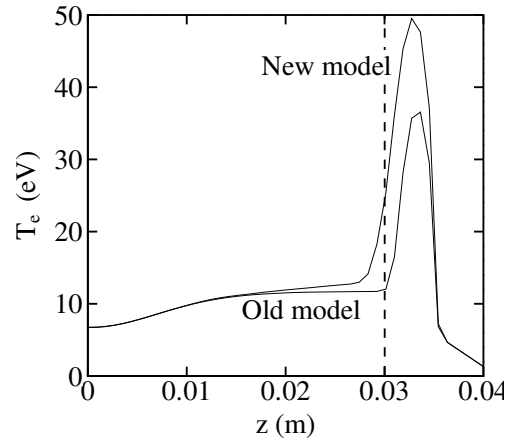


*Figure 4. Temperature profiles along the chamber obtained from HPHall for $V_d = 600$ V and the two sheath models of Fig. 3.*

potential drop for the ion-repelling sheath can be neglected (but a Bohm condition on the attracted electron flux still applies). The sheath vanishing implies much larger electron fluxes to the wall, Eq. (3), and consequently, larger energy losses.

Figure 3(a) compares, for a particular material, the original (old) sheath model of HPHall and the correct (new) one. Apart from the main difference (sheath charge-saturation versus sheath vanishing), the two models present some differences in the way they compute $T_p$ and $n_{eQ}$. The character of the sheath changes at $T_e = 12.0$ eV for the old model, and at $T_e = 13.6$ eV ($T_p = 11.7$ eV) for the new model. Figure 3(b) compares the electron energy fluxes into the sheath for the two models. Notice that for high temperatures the energy losses are almost one order of magnitude larger in the old model.

The HPHall code has been run to compare the discharge response when the old and new sheath models are used. Figure 4 depicts the temperature profiles, $T_e(z)$, ($T_e$ is constant radially) for a discharge voltage of 600 V (and parameters of Figs. 1 and 3). In both cases, high energy losses take place in a region near the chamber exit, due to either charge saturation or vanishing of the sheath, depending on the sheath model. The lower energy losses at the same temperature in the new model lead to a higher peak temperature, while the total energy lost into the walls remains similar in both models: 611 W in the old one versus 586 W in the new one. Heat conduction effects push the temperature peak outside the chamber exit. Notice that the temperature profile is practically the same with both models in the inner part of the chamber (that is for values of
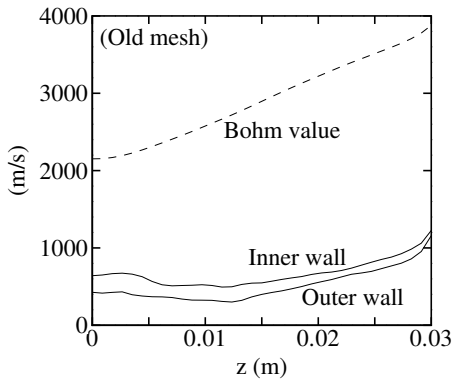
*Figure 5. Ion perpendicular velocity at the lateral ends of the domain and the Bohm velocity, along the chamber.*

$T_e$ below 11 eV) where differences between the two models are not large. [This example with a high discharge voltage has been chosen to stand out the differences between the two models, and no attempt has been made to adjust parameters to obtain a solution with high efficiency.]

## 5.    CORRECTION OF THE PLASMA/SHEATH TRANSITION

### 5.1.    The sheath transition problem

Figure 5 plots the distribution of radial ion (macroscopic) velocities at the inner and outer boundaries of the mesh as computed by HPHall for the case of Fig. 1. These velocities are much lower than the Bohm velocity. Eq. (1). Therefore, the radial ends of the computational domain (point T hereafter) are not coinciding with the sheath transition point Q. The sheath equations do not admit a valid solution departing from $v_{\perp iT} < v_{Bohm}$. Since radial gradients become very large near point Q, Fife assumed (more or less explicitly) that the ion acceleration to the sonic value took place in a thin quasineutral layer TQ; formally, the thickness of this layer, $l_{TQ}$, must satisfy

$$\lambda_D \ll l_{TQ} \ll l_{cell}, \qquad (8)$$

with $l_{cell}$ the thickness of the cell contiguous to boundary T. Figure 6 sketches this 'virtual' layer. Then, assuming free ion acceleration across this layer and $v_{\perp iT} \ll v_{Bohm}$, the potential and density drops across layer TQ satisfy

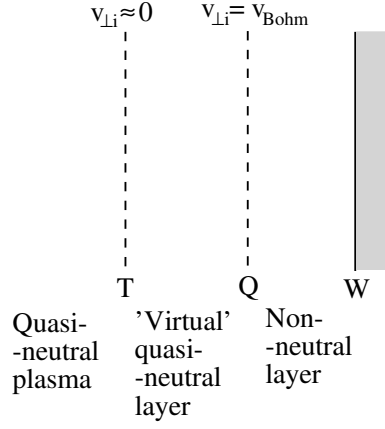$$\phi_{QT} = \frac{kT_e}{2e}, \qquad n_{eQ} = n_{eT}\exp(-1/2). \quad (9)$$



*Figure 6. Sketch of HPHall sheath transition. T is the end of the computational domain.*

HPHall uses these values to define the electron flux into the sheath (and the wall) as

$$g_{\perp eQ} = g_{Bohm} = n_{eT}\exp(-1/2)v_{Bohm}. \qquad (10)$$

However, this procedure is inconsistent:

1. One has $g_{Bohm} > g_{\perp iT}$, so that a plasma production mechanism should exist in layer TQ to provide the increment of plasma flux. The layer is too thin for ionization to be significant there. Furthermore, it would be inconsistent to have large ionization in layer TQ whereas ionization has been found small along the rest of the chamber width.

2. The PIC code ignores the existence of any added layer TQ. Then the ion flux actually delivered into the wall is $g_{\perp iW} = g_{\perp iT}$ and plasma recombination is based on that value. Thus, the recombined neutral flux is $g_{\perp nW} = -g_{\perp iW}$, much smaller than the expected value. [Observe the feedback mechanism that keeps $g_{\perp iT}$ low: low neutral recombination density yields low ionization, which yields low radial ion fluxes, and so on.]

3. The electron code uses condition (10) so that the zero current condition is not satisfied.

Therefore, the invocation of an extra layer between the computational domain and the sheath seems very dubious. The PIC code should be able to provide the Bohm flux at the inner and outer radial boundaries (that is point T must coincide with point Q). Three ways are being envisaged to correct this problem:
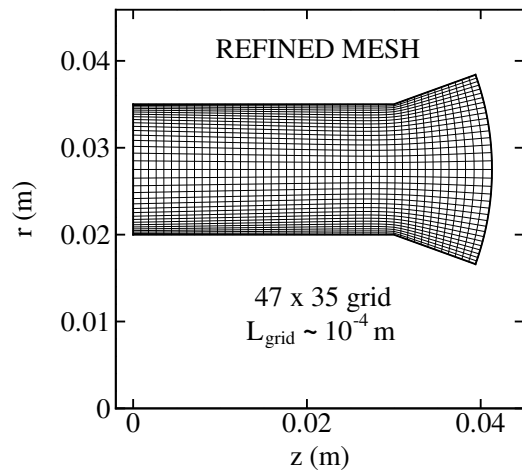
Figure 7. The refined mesh.

1. To use a refined mesh.

2. To modify the way ion magnitudes are weighed in the boundary nodes.

3. To implement somehow the (macroscopic) Bohm condition within the ion PIC code.

Here, only the first proposal is analyzed.

### 5.2. Solution with a refined mesh

A more refined mesh must provide more accurate results. In addition, it should give answers to two questions. The first one is whether the invocation of the above layer TQ has a physical sense. The second one is whether the PIC code tends to fulfill 'naturally' the Bohm condition at the radial boundaries (as it does happen, for instance, when it simulates a fluid discharge into the vacuum).

Figure 7 shows the new mesh we have used. The length of the cells close to the boundaries is five times less than in the old mesh. To maintain stability and statistical representativeness, the time step is divided by five and the particle number is multiplied by five. As a result, the execution time to obtain a stationary solution increases by about 20 times (from 50 minutes to 15 hours in a Pentium III 2.4 GHz).

Figure 8 shows radial profiles of several magnitudes at an intermediate axial position within the chamber, using the coarse and refined meshes. The comparison of results demonstrates that the radial structure varies significantly with the new mesh. Radial ion velocities and presheath potential drops
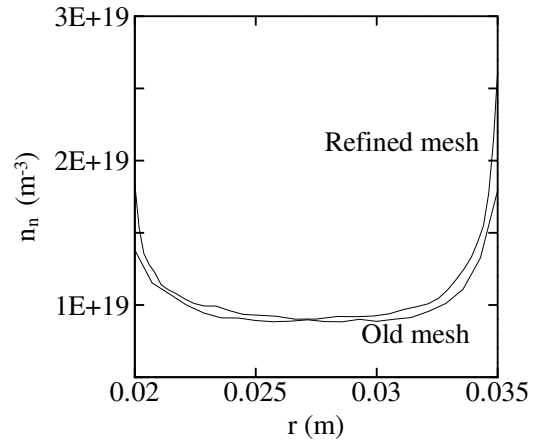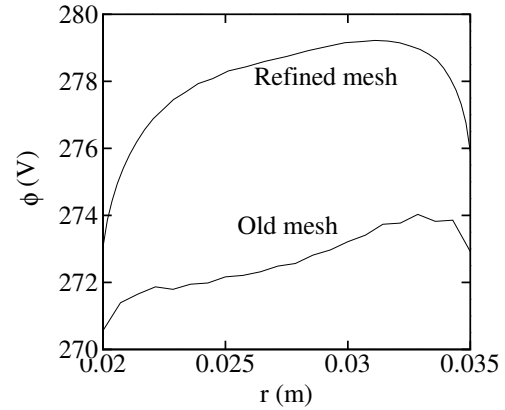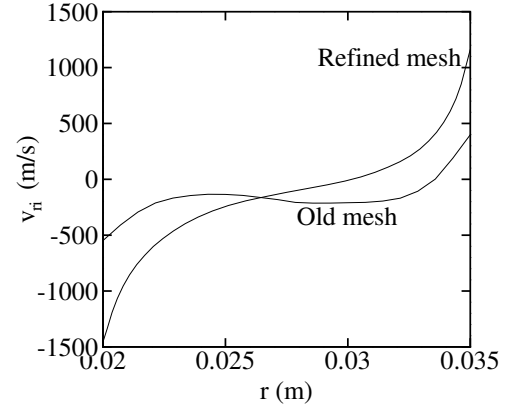


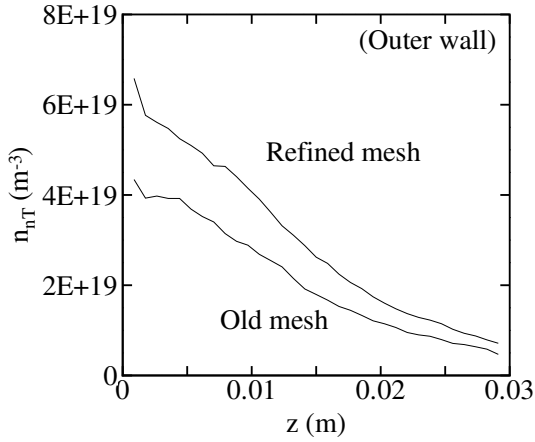Figure 8. Radial profiles at $z = 0.015$ m.

Figure 10. Ion perpendicular velocities at the domain boundaries and the Bohm velocity, for the refined mesh.
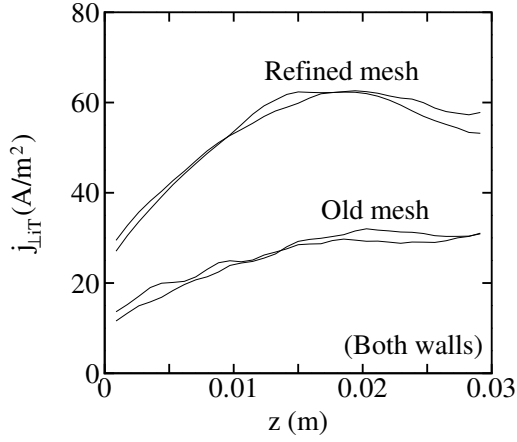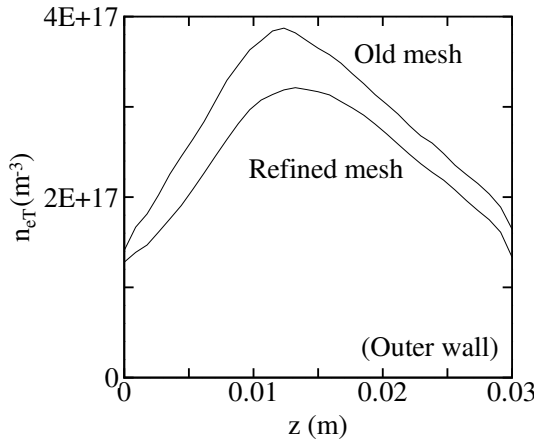


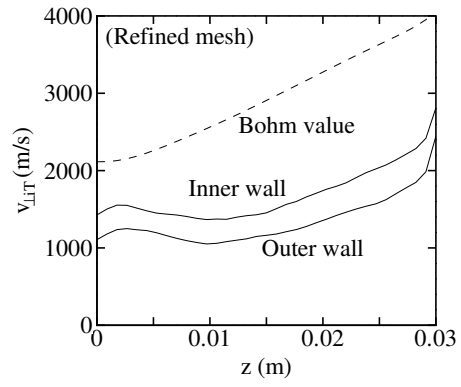*Figure 9. Axial profiles at the inner and outer boundaries for the old and refined meshes.*

are significantly larger with the new mesh. These changes are related to a better resolution of the code near the boundaries, where gradients are larger, but the differences in the spatial profiles with the old mesh are not limited to thin regions near the boundaries. Furthermore, the new mesh corrects the strange profiles of $\phi$ and $v_{ri}$ around the chamber mid-radius obtained with the old mesh.

Figure 9 plots axial profiles of different variables at the inner and outer boundaries using both meshes. The larger potential drops in the presheath with the new mesh lead to lower plasma densities at the domain boundaries, $n_{eT}$. The opposite trend was found for $v_{\perp iT}$ and the product of both, $j_{\perp iT} = en_{\perp eT}v_{\perp iT}$, turns out to increase with the new mesh. This is one of the main indications that the old mesh was computing incorrectly the ion radial fluxes. A larger $j_{\perp iT}$ means more wall recombination and thus larger neutral densities, $n_{nT}$, which finally is the required feedback to have a larger $j_{\perp iT}$. Also, the radial potential drop across half channel increases with ionization (Ahedo 2002a).

This comparison has demonstrated that the old mesh was too coarse to give acceptable radial structure of the plasma. The refined (and high-time consuming) mesh yields much more convincing results. In spite of these very positive results, Fig. 10 shows that the new mesh is still far from satisfying the Bohm condition on the radial velocities at the boundaries: the radial ion Mach number at the boundaries is about 0.5-0.6, compared to 0.2-0.3 in the old mesh. In terms of the radial kinetic energy, the figures are worse, since, with the new mesh, the ions have only about 30-40% of the required Bohm energy. If we consider that the execution time has been increased by 20 times and the high resolution of the new mesh, a Mach number of 0.6 is very disappointing.

## 6. CONCLUSIONS

An improved sheath model, which treats more correctly regions with high secondary electron emission, has been implemented in HPHall. This affects mainly the electron energy balance.

The fulfillment of the Bohm condition at the plasma-sheath transition has been shown to be a real and difficult problem to solve. The comparison of computations with two different meshes has demonstrated large differences in the radial structure of the plasma, which is more underveloped in coarse meshes. The resort to a virtual quasineutral layer between the computational domain and the sheath has proven to be incorrect.

In spite of the positive results obtained with the refined mesh, the radial ion velocity continues to be well below the Bohm value for a valid sheath transition. It is unclear to us whether an infinite mesh refining (without modifying any other algorithm in the PIC code) would lead to the fulfillment of the Bohm condition. But taking into account the alarming increment of the excution time and the moderate advance on fulfilling the Bohm condition, alternative ways of solving this issue must be found. To end, we want to emphasize that this is a central issue for the reliability of the simulation model since (i) the Bohm condition is unavoidable in a quasineutral-plus-sheath formulation and (ii) the radial plasma fluxes have a direct impact on the plasma global balances of currents and energies and the thruster performances.

## REFERENCES

Ahedo E., 2002a, Physics of Plasmas, 9, 3178

Ahedo E., 2002b, Physics of Plasmas, 9, 4340

Ahedo E., Gallardo J., Martínez-Sánchez M., 2003, Physics of Plasmas, 10, 3397

Fife J., Martínez-Sánchez M., 1995, In: 24th International Electric Propulsion Conference, Moscow, Russia, IEPC 95-240, Electric Rocket Propulsion Society, Cleveland, Ohio

Fife J., Martínez-Sánchez M., Szabo J., 1997, In: 33rd Joint Propulsion Conference, Seattle, WA, AIAA 97-3052, American Institute of Aeronautics and Astronautics,Washington, DC

Fife J.M., 1998, Hybrid-PIC Modeling and Electrostatic Probe Survey of Hall Thrusters, Ph.D. thesis, Massachusetts Institute of Technology

Hobbs G., Wesson J., 1967, Plasma Physics, 9, 85

Jolivet L., Roussel J.F., 2000, In: SP-465: 3rd Spacecraft Propulsion Conference, Cannes(Francia), 367–376, European Space Agency, Noordwijk, The Netherlands

Morozov A., 1991, Sov. J. Plasma Physics, 17, 393

# Fulfillment of the Bohm condition on the 'HPHall' fluid-PIC code

F.I. Parra and E. Ahedo

*E.T.S.I. Aeronáuticos, Universidad Politécnica de Madrid, Spain*

**Abstract**

HPHall is a quasineutral code and cannot solve the Debye sheaths at the walls of the discharge chamber. Bohm-type transition conditions, instead of wall conditions, must be implemented at boundaries of the computational domain. It was realized that HPHall does not fulfill these conditions even when fine meshes are used. The cause is found to be on the high sensitivity of the solution to the value of the ion density at the boundary nodes. The HPHall weighting method overestimates that density. Two methods to correct that weighting are proposed and validated.

## 1 Introduction

Hybrid fluid/particle-in-cell(PIC) codes represent a good trade off between macroscopic-continuous codes and fully kinetic ones for the analysis of Hall thruster discharges. They can deal, within reasonable execution times ($\sim$ hours), with the disparate dynamic scales of electrons and ions, and relatively complex geometries and magnetic field topographies.

The HPHall was developed at the Massachusetts Institute of Technology by M. Fife and M. Martínez-Sánchez [1, 2, 3]. It is a hybrid two-dimensional (2D) code where ions and neutrals are modelled as macro-particles of variable mass and electrons behave as a fluid. Ionization and wall recombination of heavy species are treated with Montecarlo methods. The high anisotropy introduced by the magnetic field, $\boldsymbol{B}$, on the electrons is used to solve separately (by finite elements) the electron motions perpendicular- and parallel- to $\boldsymbol{B}$.

HPHall was completed six years ago and has been proved very useful in the analysis of several thrusters. However, recent theoretical advances on Hall thruster physics and the experience obtained on running the code, have made convenient to revise and improve it. An improvement program was started last year at the Universidad Politécnica de Madrid. The subjects that have been revised or are under revision are the following.

1. Implementation of charge-exchange (CEX) collisions.

2. New accommodation model for wall recombination.

3. Checking of conservation of heavy species magnitudes (mass, energy, etcetera).

4. Comparison with the fully macroscopic model of Ahedo et al. [4].

5. Implementation of the charge-saturated sheath model of Ahedo [5] at the lateral boundaries.

6. Fulfillment of Bohm condition at the lateral domain boundaries.

7. New modelling of wall-collisionality effects on the electron equations.

Points 1 and 2 were commented in internal reports to the program's main sponsor. Point 3 and 4 are being used to validate the code, understand the plasma response, and identify improvements to be done on the fully macroscopic code. Point 5 and initial steps on point 6 were presented in a recent conference [6]. The subject of this paper is point 6. Point 7 will be started next.

A short account of HPHall fundamentals was presented in Ref. [6]. Figure 1 shows the three test meshes and the magnetic field profile to be used in this work. Parameters correspond to a SPT-70 thruster. In order to facilitate the comparison with the macroscopic model of Ref. [4] we are using a rather simple geometry and a B-field satisfying $B_z = 0$ and $B_r \propto 1/r$; in this way $\nabla \cdot \boldsymbol{B} = 0$,
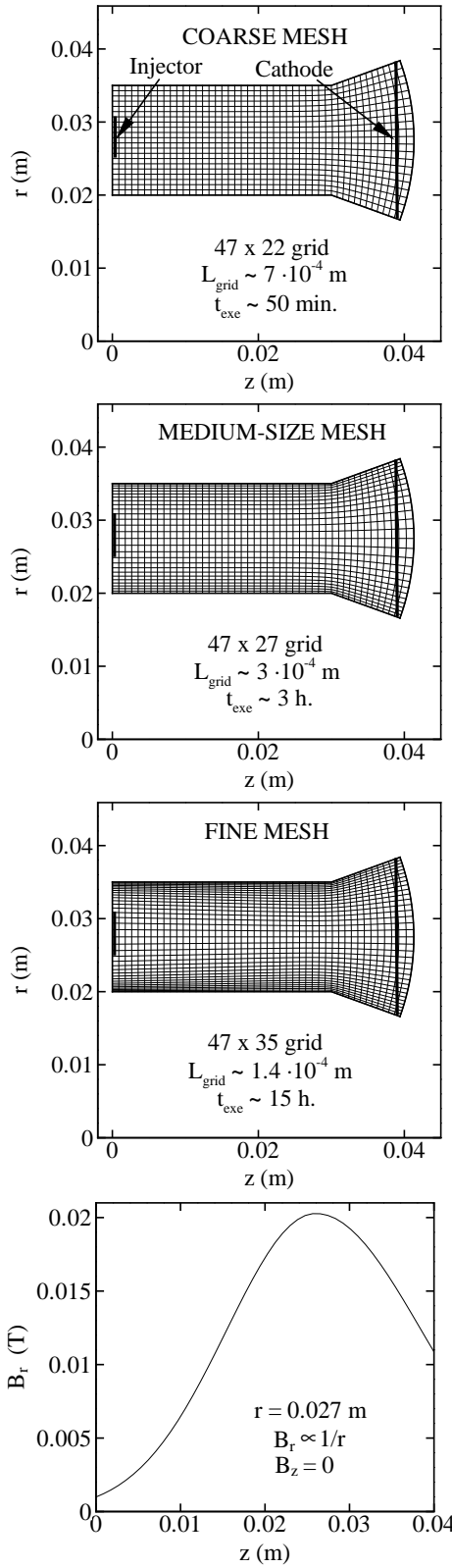
Figure 1: Typical execution times to reach a steady-state response are included.

but $\nabla \wedge \boldsymbol{B} \neq \boldsymbol{0}$. The typical execution times of the coarse(C), medium-size(M) and fine(F) meshes reported in the figure are for a Pentium III at 2.4 GHz.

## 2 The plasma-wall problem

HPHall is a quasineutral code. Plasma density is computed from a first-order weighting at each mesh node on the surrounding ion macroparticle distribution. The particle density, $n_e = n_i$ (multiple ionization is being disregarded provisionally), and the ion current density, $\boldsymbol{j}_i$, are used as input on the electron equations in order to determine the profiles of the electric potential, $\phi$, and the electron temperature, $T_e$. A good weighting of the plasma density is essential to obtain a reliable plasma response, since $\phi$ is determined from a Maxwell-Boltzmann law on $n_e$, and the electric field, which moves the ion particles, is computed from $\phi$.

Quasineutrality allows the code to avoid the very short length and time scales associated to the Poisson equation, thus explaining the fast computational time. On the other hand, the main handicap of quasineutrality is that HPHall cannot treat the Debye sheaths surrounding the chamber walls. As a consequence, Debye sheaths must be solved separately and the conditions to be imposed on those boundaries of the computational domain that are next to chamber walls, *are not the wall conditions but the transition conditions to the Debye sheaths.*

SPT thrusters have dielectric walls with high secondary electron emission (SEE). Consistent pre-sheath (quasineutral) and sheath models for this case were developed by Ahedo [5, 7]. The sheath model was implemented in HPHall recently [6]. The solution of the sheath is important mainly to compute electron energy losses, which affect the temperature profile. Here, our interest is on the implementation of the correct condition for the sheath transition, which is known as the Bohm condition.

Figure 2 shows a sketch of the lateral plasma wall interaction, with points W, Q, and T, representing the wall, the sheath transition, and the domain boundary, respectively. Points T and Q should coincide. For the classical case ($T_i \ll T_e$, negligible SEE, and a fluid ion model), the Bohm condition reads

$$v_{riQ} = v_{Bohm} \simeq \sqrt{\frac{kT_e}{m_i}}, \qquad (1)$$

where $v_{ri}$ must be interpreted as the macroscopic velocity component perpendicular to the wall. The
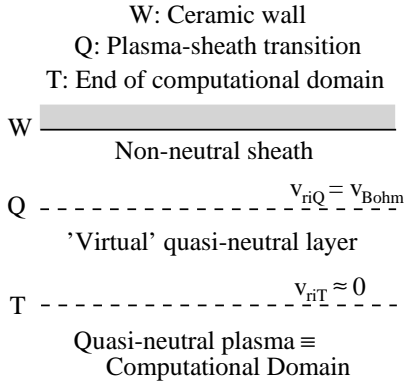
Figure 2: Sketch of the sheath-presheath regions, including the virtual layer assumed implicitly in the original version of the code.



Figure 3: Coarse mesh. Radial ion velocities at the inner and outer boundaries of the computational domain, and the Bohm velocity, $v_{Bohm} \simeq \sqrt{kT_e/m_i}$. Unless otherwise stated, plotted magnitudes in all figures correspond to time-averaged values.

.

thin Debye sheath is collisionless and quasiplanar. Thus, the ion and electron currents are constant along the sheath,

$$j_{r\alpha Q} = j_{r\alpha W}, \quad \alpha = i, e, \qquad (2)$$

with $j_{r\alpha} = en_\alpha v_{r\alpha}$. In addition, for a dielectric wall, the two currents must be the same,

$$j_{reW} = j_{riW}, \quad \alpha = i, e. \qquad (3)$$

The ion magnitudes at the domain boundary, point T, are obtained from the PIC part of the code. Figure 3 shows that the usual coarse mesh of HPHall yields perpendicular ion velocities (and currents) at the boundaries much smaller than the Bohm value, $v_{riT} \ll v_{Bohm}$. It is well known that plasma velocities and densities present large gradients in the vicinity of the sheath transition. Based on this fact, the original version of HPHall assumed the existence of a quasineutral layer TQ, thinner than the cell radial length but still much thicker than the Debye sheath, where $v_{riT}$ would reach the Bohm value. However, Ref. [6] showed that this layer is inconsistent physically. Therefore, a correct formulation of the HPHall must fulfill necessarily the Bohm condition at the domain boundaries (i.e. T=Q).

The importance of the problem was more evident when the results obtained with the coarse and fine meshes were compared [6]. Figures 4 and 5 illustrate them. [Differences with Figs. 8 to 10 of Ref. [6] are due to improving the re-emission of wall-recombined particles into the chamber.] It was found that:

- The radial plasma structure is much more developed in the fine mesh.

- Differences with the coarse mesh are not limited to a thin region around the boundaries.

- The radial ion current (which is PIC-computed) is typically twice larger with the fine mesh.

- The radial ion velocity is still far from reaching the Bohm value.

The trends of these results suggest that finer meshes would yield larger ion currents and perpendicular ion velocities closer to the Bohm value. However, this does not seem a practical procedure, taking into account the modest advance made from the coarse to the fine mesh, and the cell size and execution time of the fine mesh. Therefore, we decided to investigate directly the way HPHall computes plasma conditions near the boundaries.

# 3 Fulfillment of the Bohm condition

## 3.1 Original weighting at boundary nodes

HPHall determines most ion magnitudes (density, velocity, ...) at a mesh node by weighting that magnitude among the particles lying, at each time step, within the volume of influence of that node. For instance, the ion density at a generic node N is determined from

$$(n_{eN})_{weigh} = \frac{1}{\Delta V_N} \sum_p \frac{m_p}{m_i} S_N(r_p, z_p), \qquad (4)$$

3

Figure 4: Radial profiles for coarse(C) and fine(F) meshes at $z = 0.015$ m.



Figure 5: Axial profiles of boundary magnitudes for coarse(C) and fine(F) meshes.
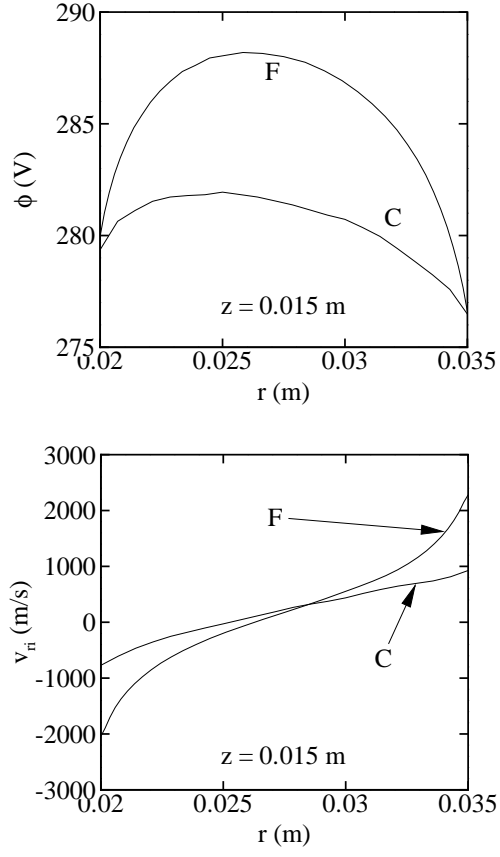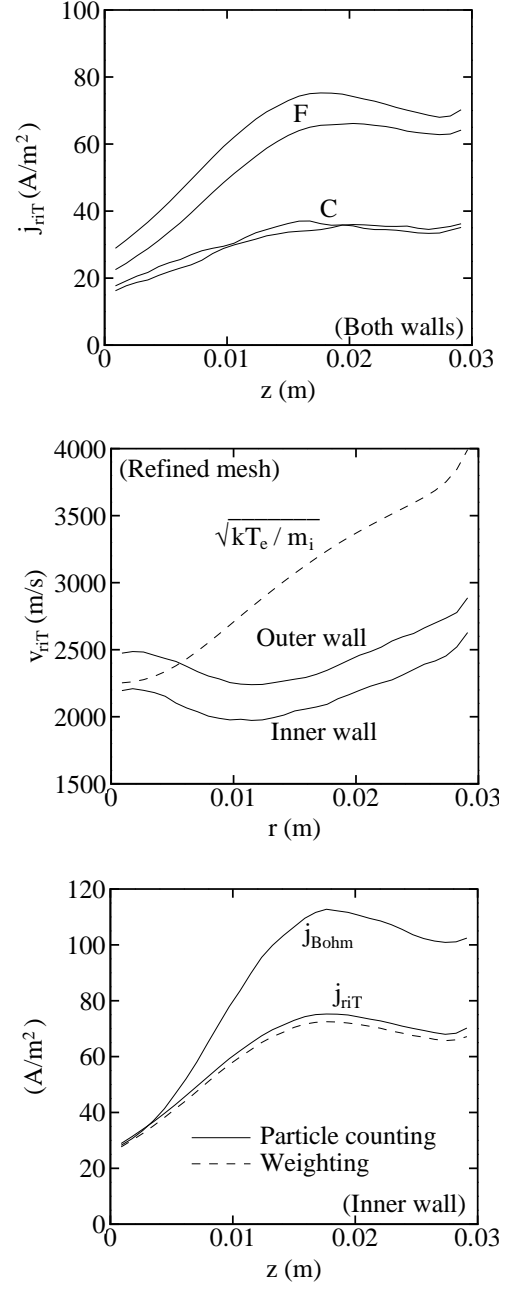
4

where $\Delta V_N$ is the volume associated to node N, $p$ refers to a particle being within the volume of influence of the node, $m_p$ and $(r_p, z_p)$ are particle mass and position, and $S_N(r_p, z_p)$ is a bi-linear type weighting function for node N. Figure 6 sketches the volume of influence of non-boundary and boundary nodes. For the particular case of a rectangular, uniform mesh, with cell sizes $\Delta r$ and $\Delta z$, the volume $\Delta V_N$ is 1/4 of the volume of influence, and the weighting function takes the simple form

$$S_N(r_p, z_p) = S_{1N}(r_p) S_{2N}(z_p), \qquad (5)$$

with

$$S_{1N}(r_p) = 1 - \frac{|r_p - r_N|}{\Delta r}$$

and a similar function for $S_{2N}(z_p)$.

Although HPHall weighting favors particles closer to the node, the one-side weighting at the boundary nodes tends to underestimate/overestimate magnitudes that increase/decrease toward the anode. Figure 5 illustrated this point for $j_{riT}$ (a magnitude that increases towards the wall). That current can be computed in two ways: by one-side weighting, $(j_{riT})_{weigh}$, and by counting the particles that cross the boundary,

$$(j_{riT})_{part} = \frac{1}{\Delta t \Delta A_T} \sum_p \frac{e m_p}{m_i}, \qquad (6)$$

with $\Delta t$ and $\Delta A_T$ the simulation time step and the area of the wall panel associated to the node, respectively. Systematically, $(j_{riT})_{part}$, which yields the most correct estimate, is larger than $(j_{riT})_{weigh}$. The error is small for $j_{riT}$ but can be much higher for magnitudes with strong gradients near the sheath transition, like $n_{eT}$ and $v_{riT}$. Fig. 6(b) illustrates the problem of one-side weighting on $n_{eT}$.

## 3.2 Forcing of the Bohm condition

In order to determine whether the no fulfillment of the Bohm condition by HPHall could be due to errors associated to one-side weighting at the lateral boundaries, we decided to modify the computation of the plasma density at a generic boundary node T. The new algorithm would be

$$n_{eT} = \min \left\{ \frac{(j_{riT})_{part}}{e v_{Bohm}}, (n_{eT})_{weigh} \right\} \qquad (7)$$

or, equivalently,

$$v_{riT} = \max \left\{ v_{Bohm}, \frac{(j_{riT})_{part}}{e (n_{eT})_{weigh}} \right\}. \qquad (8)$$
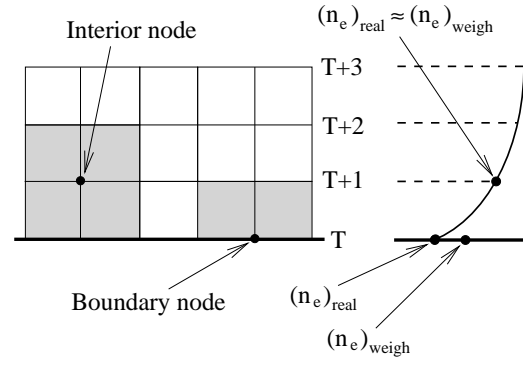


Figure 6: (Left) Shady regions represent the volumes of influence (azimuthal symmetry applies) to weight the heavy-species magnitudes at non-boundary and boundary nodes. (Right) Illustration of errors due to one-side weighting at boundary nodes.

In this way we are forcing the ions to fulfill the Bohm velocity whenever the weighted value of the ion velocity is smaller. With the new definition, $n_{eT}$ is smaller (in most points and instants) than in the original version and, therefore, the electric field is larger near the boundaries.

Figure 7 shows the radial profiles obtained with this method. The local change at the boundary has modified the whole radial profile. The comparison with the original case is really amazing, particularly for the case of the coarse mesh. Applying the Bohm-condition-forcing(BCF), radial profiles are more developed for both meshes. Furthermore, the profiles with BCF are practically identical for the coarse and fine meshes, which gives reliability to this procedure.

Figure 8 shows axial profiles of $j_{riT}$ and $v_{riT}$ at the inner wall (and time-averaged) for the three meshes with BCF. The temperature profiles for the three meshes are practically the same. The fact that $v_{riT} > v_{Bohm}$ is the consequence of temporal fluctuations on the instantaneous value of Eq. (8), and of a non-zero ion temperature. Deviations from the Bohm value are larger for the fine mesh because the instantaneous values of $(v_{riT})_{weigh}$ are larger for that mesh. The differences on the three profiles of $j_{riT}$ and $v_{riT}$ are due to the temporal averaging, mainly.

## 3.3 Corrected weighting

Bohm condition forcing has demonstrated that correct values of plasma magnitudes at the boundary nodes are essential for a valid solution. At the

5

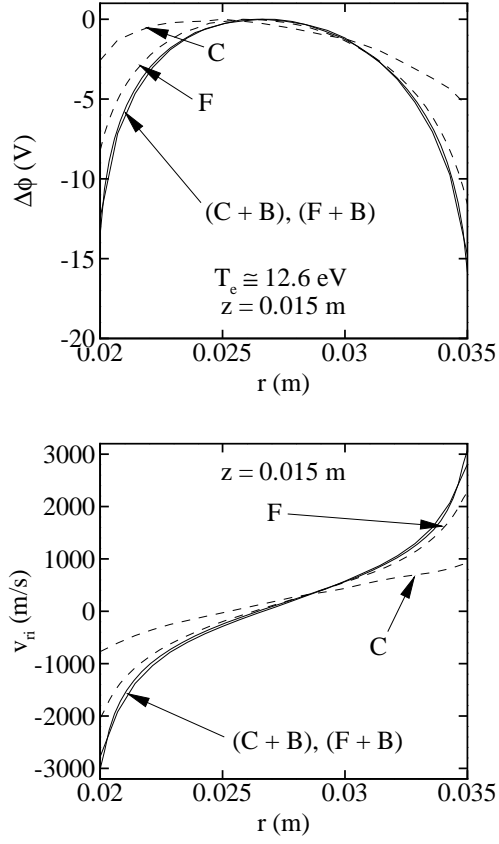Figure 7: Radial profiles at $z = 0.015$ m for coarse(C) and fine(F) meshes. (+B) means that Bohm condition forcing is applied.
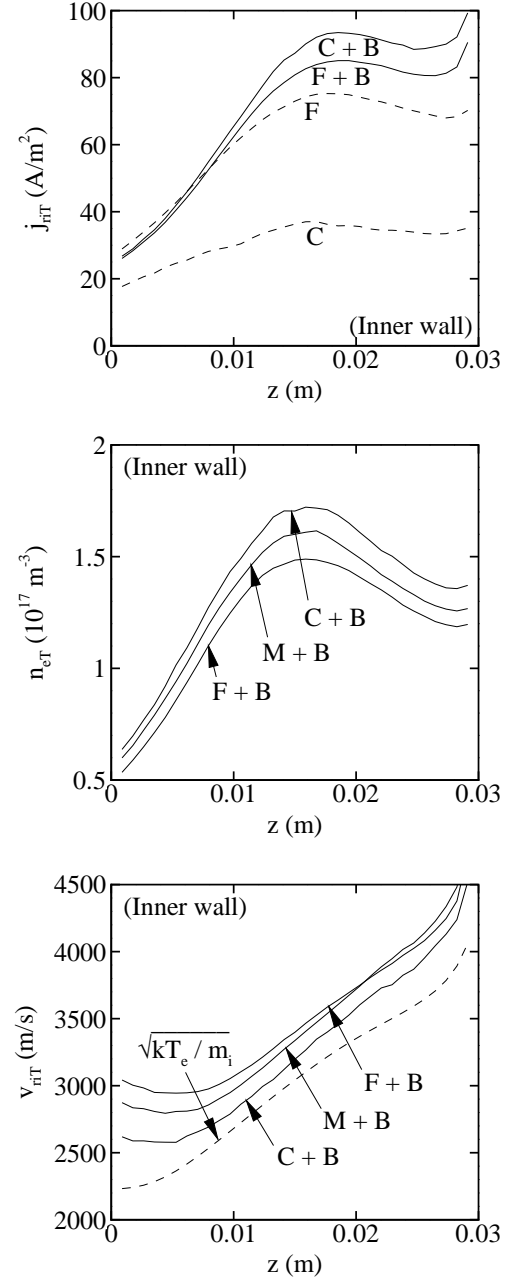


Figure 8: Axial profiles for the three meshes, with(+B) and without Bohm condition forcing.

same time, BCF is an intrusive way to define ion magnitudes, since it relies on a result external to the PIC formulation. Since the domain boundaries of HPHall act as vacuum (ions are lost without any feedback), a well-formulated PIC code should satisfy the Bohm/sonic condition naturally, without forcing it (and, hopefully, without using an infinitely thin mesh).

These considerations leaded us to try to correct the one-side weighting used at the boundary nodes. The idea of our corrected weighting(CW) algorithm is the following. Let us consider that the number of ion macroparticles is high enough, so that the ion density can be represented by a continuous function $n_{e,real}(r, z)$. Near the boundary node T, this function can be expanded as

$$n_{e,real}(r) = (n_{eT})_{real} + m\ (r - r_T) + O[(r - r_T)^2], \quad (9)$$

where $m = (\partial n_{e,real}/\partial r)_T$ (and, for sake of clarity, we omit the dependence on $z$ and, when necessary, we consider a uniform mesh). Equating now the linear weighting of both $n_{e,real}(r)$ and the actual PIC macroparticles, yields the following relation:

$$(n_{eT})_{weigh} = \frac{2}{\Delta r} \int_{r_T}^{r_{T+1}} n_{e,real}(r) S_{1T}(r) dr =$$
$$(n_{eT})_{real} + \frac{m}{3}\Delta r + O(\Delta r^2). \quad (10)$$

Applying the same action to the neighbor point T+1 (Fig. 6), one has

$$(n_{e,T+1})_{weigh} = (n_{eT})_{real} + m\Delta r + O(\Delta r^2). \quad (11)$$

Solving linear equations (10) and (11), the corrected weighting value of $n_{eT}$ is

$$(n_{eT})_{real} \simeq \frac{3}{2}(n_{eT})_{weigh} - \frac{1}{2}(n_{e,T+1})_{weigh} + O(\Delta r^2), \quad (12)$$

which is smaller than $(n_{eT})_{weigh}$ for usual conditions. This correction lies on internal (PIC-computed) magnitudes only, but, at the same time, it depends on a second, neighbor node.

Figure 9 shows radial profiles for the three meshes when CW is used for $n_{eT}$ and $v_{riT}$. There is a clear improvement with respect to the results with the original weighting. However, the corrected weighting works better the finer is the mesh; in fact, results for the coarse mesh are far from satisfying Bohm condition. This behavior with the mesh size is due to the non-local character of the CW, which presents errors of the order of the square of the cell radial size, $O(\Delta r^2)$.

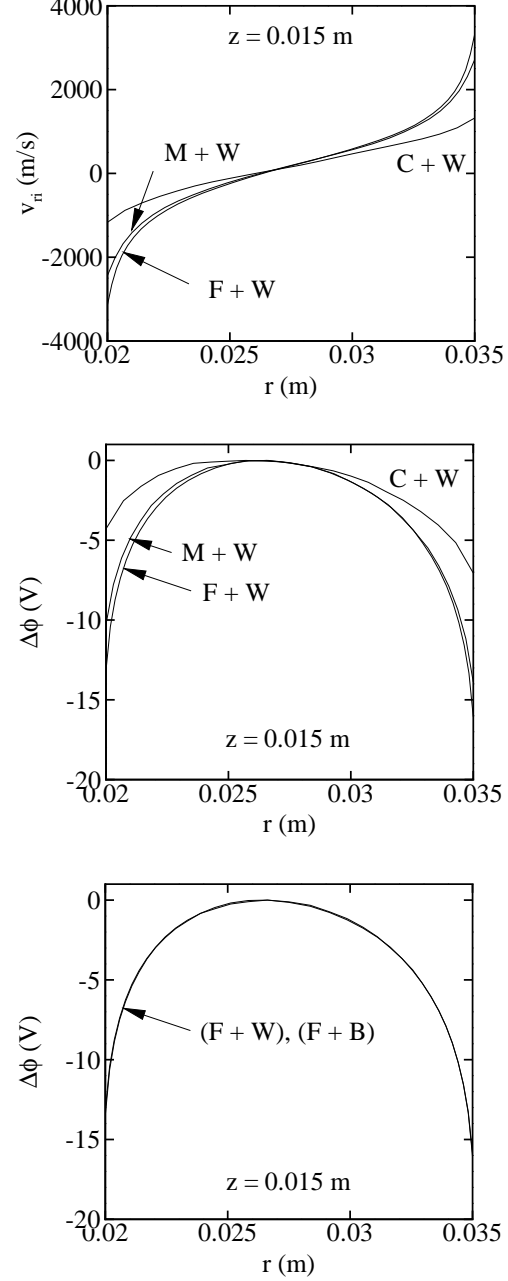The comparison of radial profiles when applying BCF and CW to the fine mesh, at the bottom



Figure 9: Radial profiles for the three meshes, with(+W) and without application of the corrected weighting algorithm. The bottom figure compares radial profiles when the BCF or the CW are applied together with the fine mesh.
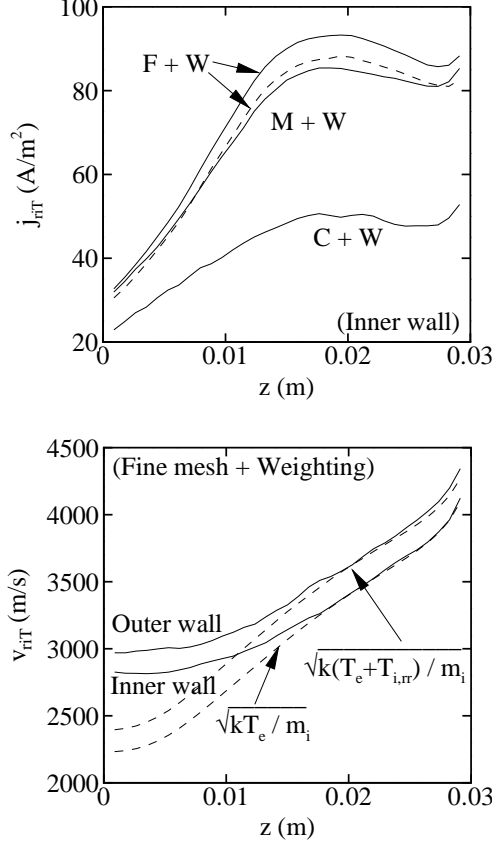
Figure 10: Axial profiles for the three meshes, with (+W) and without application of the corrected weighting algorithm. (Top) Solid lines represent $(j_{riT})_{part}$ and the dashed line shows $e(n_{eT})_{real}(v_{riT})_{real}$ for F+W. (Bottom) $(v_{riT})_{real}$.

of Fig. 9, is excellent, which augments the reliability and accuracy of the methods we are testing. Also, these radial profiles compared very well with those obtained with the radial macroscopic model of Ahedo [7].

Figure 10 depicts axial profiles of boundary magnitudes. It is seen that (for this thruster conditions) the intermediate mesh plus CW yields valid enough results. There are other observations worth to mention. First, there are differences between the radial velocities at the inner and outer walls (in spite of the same electron temperature). These can be due to cylindrical effects on the weighting [8], which are not taken into account in HPHall. Second, the ion velocity at the outer wall seems to include the effect of the ion temperature or, more exactly, of the $rr$-component of the (weighted) ion pressure tensor, $kT_{i,rr} = P_{i,rr}/n_i$. Third, $v_{riT}$ tends to exceed clearly the Bohm value in the near anode region. This could be related to larger temporal fluctuations or the low ion fluxes in that region.

## 4  Final comments

HPHall is a quasineutral code that must satisfy sonic Bohm conditions at the domain boundaries next to chamber walls. The original version of the code was unable to meet this condition even when fine meshes were used. The way of weighting ion magnitudes at the boundary nodes has been identified as the cause of that malfunction of the code.

The problem has been solved with both a one-node, external method (Bohm condition forcing) and a two-node, internal method (corrected weighting algorithm). BCF turns out to be very effective, yielding valid solutions even for coarse meshes. CW works well only for fine enough meshes. For fine meshes both methods yield similar results. These conclusions suggests that BCF should be ordinarily used, whereas CW and fine meshes could be reserved to validate BCF results.

In spite of the very positive results, some improvements on both methods should still be made. First, the general weighting algorithm should take into account cylindrical effects. Second, BCF should try to compensate the effect of temporal fluctuations, which tends to overestimate ion velocities. Third, BCF should include the effect of the ion temperature. Four, a further analysis of the plasma behavior in the near anode region is necessary in order to understand the significant deviations of the radial ion velocity from the Bohm condition.

The ideal solution with respect to the BCF al-

|  | C MESH | | F MESH | | |
| --- | --- | --- | --- | --- | --- |
|  | None | BCF | None | CW | BCF |
| $F$(mN) | 29 | 28 | 30 | 31 | 29 |
| $P_d$(W) | 510 | 489 | 503 | 504 | 475 |
| $P_{use}$(W) | 254 | 222 | 244 | 238 | 221 |
| $\eta$(%) | 40 | 38.9 | 43 | 46.1 | 42.8 |
| $\eta_u$(%) | 75.2 | 70.6 | 72.4 | 70.9 | 67.7 |
| $P_{ion}$(W) | 46 | 55 | 53 | 57 | 53 |
| $P_{wall}$(W) | 176 | 171 | 170 | 173 | 162 |

Table 1: HPHall performances for different simulation cases. $V_d = 300$ V, $\dot{m} \simeq 2.1$ mg/s, and $B_{max} \simeq 200$G. This is just an example to compare performances. No attempt to optimize the magnetic field has been made.

gorithm would be to determine the 'internal' Bohm condition from a sheath model based on the actual ion macroparticles that are crossing the sheath.

The Bohm condition must also be satisfied at the anode side of the HPHall domain. BCF and CW algorithms have not been implemented yet at the anode. The implementation is simple for the one-dimensional magnetic field profile considered in this work. On the contrary, for the usual two-dimensional magnetic topography near the anode, the treatment of the whole near-anode region requires a deep revision.

To end, Fig. 11 compares the two-dimensional profiles with and without Bohm condition fulfillment. The larger development of the radial structure of the plasma in the new version of the code is clearly observed. The quasi-symmetry of the profiles with respect to the chamber mid-radius in the new version is another positive feature. However, these important improvements of the code have modest consequences on the computed thruster performances, as Table 1 shows. Two are the reasons: (1) in general, radial gradients are much less significant than axial gradients, (2) the computation of the electron losses at the walls, which dominate the total energy losses, is made by HPHall with an expression independent of the ion flux reaching the walls. The consequences should be larger when wall losses play a lesser role, like for lower discharge voltages, and short and metallic chambers.

## Acknowledgments

## References

[1] J.M. Fife and M. Martínez-Sánchez. Two-dimensional hybrid particle-in-cell (PIC) modelling of Hall thrusters. In *24th International Electric Propulsion Conference, Moscow, Russia*, IEPC 95-240. Electric Rocket Propulsion Society, Cleveland, Ohio, 1995.

[2] J.M. Fife, M. Martínez-Sánchez, and J. Szabo. A Numerical Study of Low-Frequency Discharge Oscillations in Hall Thrusters. In *33rd Joint Propulsion Conference, Seattle, WA*, AIAA 97-3052. American Institute of Aeronautics and Astronautics, Washington, DC, 1997.

[3] J. M. Fife. *Hybrid-PIC Modeling and Electrostatic Probe Survey of Hall Thrusters*. PhD thesis, Massachusetts Institute of Technology, 1998.

[4] E. Ahedo, J.M. Gallardo, and M. Martínez-Sánchez. Effects of the radial-plasma wall interaction on the axial Hall thruster discharge. *Physics of Plasmas*, 10(8):3397–3409, 2003.

[5] E. Ahedo. Presheath/sheath model of a plasma with secondary emission from two parallel walls. *Physics of Plasmas*, 9(10):4340–4347, 2002.

[6] F. Parra, E. Ahedo, M. Martínez-Sánchez, and J.M. Fife. Improvement of the plasma-wall model on a fluid-PIC code of a Hall thruster (to be published). In *SP-555: 4th Spacecraft Propulsion Conference, Sardinia (Italy)*, Noordwijk, The Netherlands, 2004. European Space Agency.

[7] E. Ahedo. Radial macroscopic model of a plasma flowing along annular dielectric walls. *Physics of Plasmas*, 9(7):3178–3186, 2002.

[8] J.P. Verboncoeur. Symmetryc spline weighting for charge and current density in particle simulation. *J. Computational Physics*, 174:421 –427, 2001.
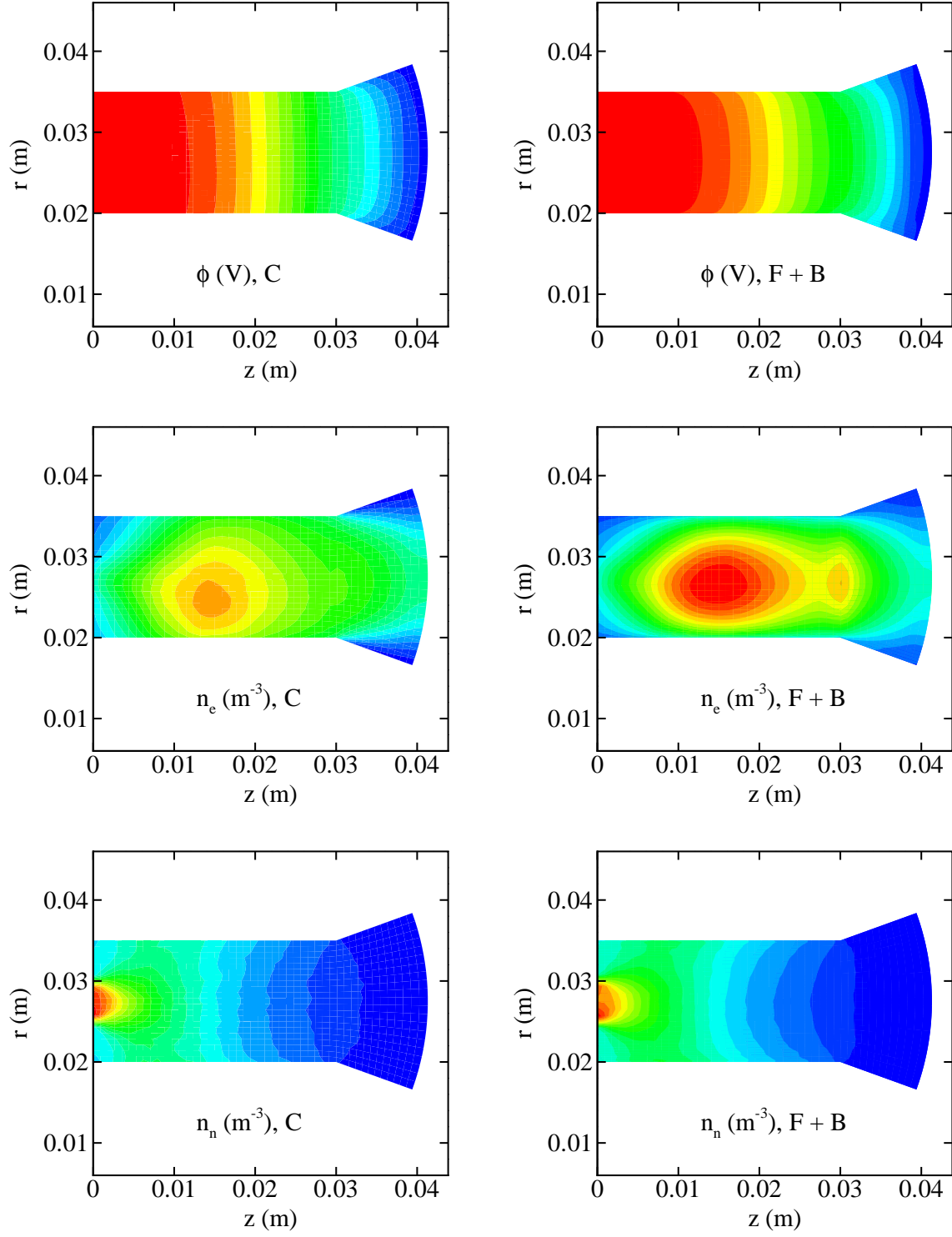
Figure 11: Comparison of two-dimensional contours of the electric potential (top), the plasma density (middle), and the neutral density (bottom), for the coarse mesh (left) and the fine mesh plus Bohm condition forcing (right).

# A two-dimensional hybrid code of the Hall thruster discharge

F.I. Parra and E. Ahedo

*E.T.S.I. Aeronáuticos, Universidad Politécnica de Madrid, 28040 Madrid, Spain*

M. Martínez-Sánchez

*Massachusetts Institute of Technology, Cambridge, USA*

J.M. Fife

*Air Force Research Laboratory, Edwards AFB, California, USA*

## 1   Introduction

There is a strong scientific and technological interest in Hall thrusters. Many models on the plasma discharge have been proposed in recent years. They can be classified in three groups: macroscopic models [1, 2], particle models [3], and hybrid fluid/particle models [4, 5]. Kinetic models are used only for particular aspects of the discharge (like the plasma-wall interaction).

Hybrid fluid/particle-in-cell(PIC) codes represent a good trade off between macroscopic-continuous codes and fully kinetic ones for the analysis of Hall thruster discharges. They provide solutions in relatively short times, despite the disparate dynamic scales of electrons and ions, and relatively complex geometries and magnetic field topographies.

HPHall is a hybrid two-dimensional(2D) code, developed by Fife and Martínez-Sánchez [4, 6, 7]. Heavy species (ions and neutrals) are modelled with Particle In Cell plus MonteCarlo-type (PIC-MC) methods, whereas electrons are modelled as a fluid. Electrons are strongly magnetized and the high anisotropy introduced by the magnetic field $\boldsymbol{B}$ permits independent solution of perpendicular- and parallel-to $\boldsymbol{B}$ electron motions.

HPHall was completed in 1998 and has been proved very useful in the analysis of several thrusters. However, the large experience obtained on running the code and recent advances

on modelling the Hall thruster physics have made necessary to revise and improve the code. This paper presents the main features of the new version, which we call HPHall-2.

The changes implemented on HPHall-2 can be classified in two categories. The main category comprises improvements related to the plasma interaction with the lateral walls and are introduced in Sec. 2. These changes were necessary to assure the consistency of the model. The second category consists of improvements which do not affect the fundamentals of the code. The main ones are: (a) implementation of ion-neutral collisions; (b) new algorithms for injection, reflection, and recombination of neutrals at the walls; and (c) development of routines to check the local conservation of heavy species magnitudes, like mass and energy.

## 2  Issues on modelling the plasma-wall interaction

A key feature of HPHall is to take advantage of the small Debye length of the plasma, $\lambda_D$, to work with a quasineutral model. This approximation minimizes computation time by avoiding the very short spatial and temporal scales associated with space-charge fields, thus requiring a relatively small computational time. For example, a typical stationary solution takes around $10-100$ minutes. A quasineutral code, however, presents its own disadvantages: it is impossible to solve the space-charge sheaths formed around the chamber walls. These sheaths must solved separately and the plasma conditions to be imposed on the plasma at the near-wall boundaries of the computational domain of HPHall *are not* the wall conditions but the transition conditions to the Debye sheaths.

In the original HPHall, we identified three subjects related to sheath and wall interaction and requiring improvements:

(a) the correct matching at the plasma/sheath transition

(b) the sheath model for high secondary electron emission

(c) the modelling of wall collisionality

## 2.1 Plasma/sheath transition

It is well known that the only possible transition between a subsonic plasma and a collisionless, electron-repelling sheath corresponds to the Bohm sonic condition for the ion flow. In a kinetic model, the Bohm condition is defined in Equation (1):

$$\int_0^\infty \frac{Z_i f_i(v_N)}{m_i v_N^2} dv_N \leq \frac{n_e}{T_e} \tag{1}$$

with $f_i(v_N)$ the one-dimensional ion distribution function, $v_N = \boldsymbol{v} \cdot \boldsymbol{1}_N$ the velocity perpendicular to wall (and sheath), Fig. 1, $Z_i$ the charge number, and $n_e$ and $T_e$ the local plasma density and electron temperature.

The Bohm condition is applied differently on different kind of models. For example, in a fluid ion model, to close both the quasineutral and sheath problems, the ion macroscopic velocity perpendicular to the boundary is established as a boundary condition. The value depends mainly on the temperatures, according to Equation (2)

$$u_{Ni} \equiv \boldsymbol{u}_i \cdot \boldsymbol{1}_N \geq \sqrt{\frac{Z_i T_e + T_i}{m_i}} \tag{2}$$

with $\boldsymbol{u}_i$ and $T_i$ the ion local *macroscopic* velocity and temperature.

In PIC ion models, the ions are represented by using macroparticles and no with average velocities and temperatures. Therefore, the Bohm condition cannot be imposed. It must be achieved by the code in a natural way. The mechanism for this can be explained as it follows: an electron-repelling sheath returns back no ion, thus acting as vacuum; as a natural effect of this vacuum, a sonic ion flow at the sheath boundary *should* arise naturally.

However, HPHall has been shown to yield, for usual mesh sizes, very subsonic ion flows at the boundaries with lateral walls [8]. Consistent with it, the radial structure of the quasineutral plasma is very underdeveloped. The inaccuracy of that solution became evident in Ref. [8] when a finer mesh is used: the ion flow at the boundary increases and larger plasma gradients over the whole radial section are found. But the disappointing conclusion is that for practical mesh sizes the ion flow remains well subsonic, making evident that other methods should be

used in HPHall in order to satisfy the Bohm condition. Next, Ref. [9] demonstrates that the problem lies in the way plasma magnitudes are computed by the PIC code at the boundaries of the quasineutral domain. Among the plasma magnitudes, the density seems to have the most important effect on the Bohm condition. Two alternative methods to compute them are proposed and validated. Both are implemented in HPHall-2 and commented in Sec. 4.6.

## 2.2 Secondary Electron Emission

The second main modification on HPHall is the sheath model. HPHall is designed for Hall thrusters with long ceramic chambers. These can present high secondary electron emission (SEE), which affects strongly the sheath structure [10]. Fife et al. [7] used a sheath model where the sheath changed from being electron-repelling to ion-repelling when the SEE was near 100%. But it was pointed out later [11] that the sheath becomes charge-saturated within the electron-repelling regime. This effect yields lower energy losses at high SEE. Ahedo [12] modified the sheath model of Fife et al. in order to take into account charge saturation and to address the fact that primary and secondary electron populations are used within the sheath but a single electron population is used generally for the quasineutral plasma. The model of Ahedo has been matched to the electron submode of HPHall-2.

## 2.3 Wall collisionality

The third important improvement of HPHall-2 is related to what is known as 'wall collisionality'. It turns out that SEE is important also when considering cross field electron transport. Secondary electrons enter radially from the sheath into the quasineutral plasma as a monoenergetic beam without any $E \times B$ drift, and this amounts to increased electron mobility in the axial direction near the wall [13]. For HPHall, Fife et al. computed the net secondary flux *near* each lateral wall and include it as extra terms in the total electron current *only*. In HPHall-2 we have opted for the alternative derivation of 'wall mobility' proposed by Ahedo et al. [1]. In that derivation, the effect of SEE in the momentum equation is not based on the local behavior of the secondary flux near the walls but on the reduction of the macroscopic electron azimuthal velocity, $u_{\theta e}$. The secondary electrons are injected in the main population

of the quasineutral plasma with $u_{\theta e} = 0$, and they reduce the average $u_{\theta e}$ in the flow. Also, and of more relevance on the results, HPHall-2 includes the contribution of the secondary flux to the electron energy equation, a point missed in the original formulation.

## 3 General features of the code

HPHall-2 is an axisymmetric and quasineutral code, which simulates the plasma discharge from the anode to the cathode neutralization surface. The magnetic field $\boldsymbol{B}$ in the chamber is generated externally by the thruster magnetic circuit and is implemented into the code in a pre-process. The small magnetic field induced by the thruster discharge is disregarded.

The structure of the code consists of a PIC subcode for the heavy species and a macroscopic subcode for the electrons. After each time interval, $\Delta t$, the main outputs of the PIC subcode are the plasma density, $n_e = Z_i n_i$, (with $Z_i$ the average ion charge number) and the ion flux density, $\boldsymbol{g}_i \equiv n_i \boldsymbol{u}_i$, whereas the main outputs of the electron subcode are the electric potential, $\phi$, and the electron temperature, $T_e$.

Cylindrical variables $(z, r, \theta)$ are used for the physical space. The PIC subcode uses a simulation mesh in the plane $(z, r)$, Fig. 1. This mesh is rectangular in variables $(\xi, \eta)$ and nodes of the cells, denoted generically by $jk$, correspond to integer values of these variables:

$$j = \mathrm{ip}(\xi), \quad k = \mathrm{ip}(\eta), \tag{3}$$

[ip() means integer part]. Each cell is denoted by the name of the node with lowest indexes. For a conventional thruster geometry, the anode sheath boundary is at $\xi = 1$, and the inner and outer lateral surfaces are at $\eta = 1$ and $\eta = k_{max}$, respectively. These lateral boundaries consist of Debye sheaths next to chamber walls, the plume/atmosphere interface, or the axis of symmetry.

The simulation mesh is created in a pre-process and the code stores the values at the nodes of the transformation $(z, r) = H(\xi, \eta)$ and of its Jacobian matrix, $JH(\xi, \eta)$. A bilinear function is used to determine $H$ and $JH$ at a cell interior points; for instance, for cell $jk$ and

5

$r(\xi, \eta)$ one has

$$r(\xi, \eta) = \xi'\big[\eta' r_{j+1,\,k+1} + (1 - \eta') r_{j+1,\,k}\big] + (1 - \xi')\big[\eta' r_{j,\,k+1} + (1 - \eta') r_{jk}\big], \qquad (4)$$

with $r_{jk} = r(j, k)$,

$$\xi' = \xi - j, \quad \eta' = \eta - k. \qquad (5)$$

Electrons are strongly magnetized so that a collisional-diffusive model is used with very different dynamics in directions parallel and perpendicular to the magnetic field. The magnetic streamlines, indeed streamsurfaces when gyrated over $\theta$, $S : \lambda(z, r) = \text{const}$, satisfy

$$\partial\lambda/\partial z = rB_r, \qquad \partial\lambda/\partial r = -rB_z, \qquad (6)$$

The integration of these equations places the surface $\lambda = 0$ adjacent to the anode; the cathode streamsurface is represented by $\lambda = \lambda_{cat}$. The electron subcode uses a mesh of streamlines $\lambda_l, l = 1, 2, ...$, Fig. 1. In addition to $\lambda$, it is convenient to define an arc variable $\chi$ *along each streamline*, which satisfies

$$(\partial z/\partial\chi, \partial r/\partial\chi) = (B_z, B_r)/B. \qquad (7)$$

The unit vectors in the directions parallel and perpendicular (in a meridian plane) to the magnetic field, $\mathbf{1}_\parallel$ and $\mathbf{1}_\perp$ (Fig. 1), satisfy

$$\frac{\partial}{\partial\mathbf{1}_\perp} = rB\frac{\partial}{\partial\lambda}, \qquad \frac{\partial}{\partial\mathbf{1}_\parallel} = \frac{\partial}{\partial\chi}. \qquad (8)$$

## 4    The heavy species subcode

The version of the code presented in this paper includes only neutrals and singly-charged ions. Thus, the quasineutrality condition reads $n_e = n_i$. Looking for a valid compromise between good statistics and the strong inhomogeneity of plasma densities along the chamber, the code uses $N_\alpha^{cell} \sim 20 - 50$ (super)particles per cell and species $\alpha$ ($\alpha = i$ and $n$ stands for ions and neutrals, respectively). Since ion and neutral densities differ typically by two

orders of magnitude, the mass $M_n$ of a superneutral is much larger than the mass $M_i$ of a superion. This has consequences for the collisional processes, particularly for ionization: a single ionizing event cannot transform one superneutral on one superion.

The timestep $\Delta t$ used by the PIC subcode to move heavy particles is selected in order that one particle advances, in general, no more than one cell per timestep. Departing from the plasma state at instant $t$, the process to determine the number of particles, their mass, position, and velocity at $t + \Delta t$ includes several stages, which are commented next.

## 4.1 Particle advancement

Let us consider that, at instant $t$, we know: the position, $\boldsymbol{x}$, and velocity, $\boldsymbol{v}$, of all superparticles; the plasma density, $n_e = n_i$ (from the particle subcode too); the electric potential $\phi$ and the temperature $T_e$ (from the electron subcode); and the magnetic field $\boldsymbol{B}(z, r)$.

The equation of force on each superparticle is integrated using a leapfrog scheme, which is conservative and minimizes the data storage [14]. The displacement equations, centered at instant $t$, are

$$\boldsymbol{v}_{+1/2} - \boldsymbol{v}_{-1/2} = \Delta t \left[ \frac{q}{m} \left( \boldsymbol{E}_0 + \boldsymbol{v}_{-1/2} \wedge \boldsymbol{B} \right) + \boldsymbol{R}_0 \right] \tag{9}$$

$$\boldsymbol{x}_1 - \boldsymbol{x}_0 = \Delta t \, \boldsymbol{v}_{+1/2} \tag{10}$$

Here, $q/m$ is the particle charge-to-mass ratio (zero for neutrals and $e/m_i$ for ions), $\boldsymbol{E}$ is the electric field, $\boldsymbol{R}$ is any non-electromagnetic force (like charge-exchange collision effects on neutrals), and a numerical subscript $a$ refers to the instant $t + a\Delta t$ [for instance, $\boldsymbol{v}_{+1/2} \equiv \boldsymbol{v} \left( \boldsymbol{x}(t + \Delta t/2), t + \Delta t/2 \right)$]. The code uses a three-dimensional velocity vector for particles. Although ions are weakly unmagnetized, the inclusion of magnetic effects in Eq. (3) has only a small computational cost and presents some potential benefits.

In order to avoid large errors on the position of particles that are close to the axis of symmetry, $r = 0$, Eqs. (9) and (10) are solved, for each particle, in a cylindrical frame of reference centered at the position of the particle at instant $t$ [14].

Once we know the physical position of a particle at $t + \Delta t$, that is $(z, r, \theta)_1$, the position

in the simulation grid at that instant, $(\xi, \eta, \theta)_1$, is determined using a Newton's algorithm on function $(z, r) = H(\xi, \eta)$, departing from positions $(z, r)_0$ and $(\xi, \eta)_0$ (at instant $t$).

## 4.2  Ionization

Ionization takes place by electron impact on the neutrals. DSMC (Direct Simulation Monte Carlo) methods are not applicable to simulate ionization because of the electrons are treated as a fluid [15]. Standard MCC(Monte Carlo Collisions) methods are applicable neither since (i) neutral particles are the dominant species, (ii) the neutral flux is highly reduced along the chamber, and (iii) ion and neutral particles have very different masses. Therefore, a particular method was developed for ionization in HPHall [4], which consists in the following.

First, the single-charge ionization rate is obtained assuming a Maxwellian electron distribution function and using the Drawin formula for the ionization cross-section [16]. Adjusting the parameters of that formula for xenon, the ionization rate can be expressed as

$$\dot{n}_i = n_n n_e \zeta(T_e/E_i), \tag{11}$$

with

$$\zeta(\theta) = \frac{Q_i}{\theta^{3/2}} \int_1^\infty du \exp\left(-\frac{u}{\theta}\right) \frac{u-1}{u} \ln u, \tag{12}$$

$E_i = 12.1\text{eV}$ as the first ionization energy, and $Q_i = 4.13 \cdot 10^{-13}\text{m}^3\text{s}^{-1}$.

Second, the decay of the mass $M_n$ of a super-neutral, because of ionization, follows

$$\frac{dM_n}{dt} = -M_n n_e \zeta(T_e), \tag{13}$$

which, discretized, becomes

$$M_n(t + \Delta t) = M_n(t)[1 - \Delta t\ \dot{n}_i/n_n]. \tag{14}$$

Third, the number of superions that are created at a generic cell $jk$ during a time interval

$\Delta t$ is based on the quantity

$$N_{jk,\text{ioniz}} = \frac{m_i}{M_i} < \dot{n}_i > V_{jk}\Delta t \tag{15}$$

where $M_i$ is the mass of a new superion, $V_{jk}$ is the cell volume, and $< \dot{n}_i >$ is the average ionization rate within the cell. The effective (integer) number of new super-ions is determined from a probability algorithm applied on $N_{jk,\text{ioniz}}$. The position (at $t + \Delta t$) within the cell and the velocity (at $t + \Delta t/2$) of these superions are selected randomly. For the velocity, we use a drifted Maxwellian distribution, based on the *local* fluid velocity and temperature of the neutrals, $\boldsymbol{u}_n$ and $T_n$, respectively.

## 4.3 Ion-neutral collisions

The main phenomenon here are charge-exchange(CX) collisions. Their principal effect uses to be in the plume, where low-velocity ions can be trapped by spacecraft potential, hitting it and producing damages.

Charge-exchange collisions keep constant the ion and neutral densities but modify their momentum. Considering the mass difference between superions and the superneutrals ($M_n \gg M_i$), a MonteCarlo Collision Model seems a good option to treat this phenomenon. Light superions will suffer these collisions individually but heavy superneutrals will feel them only in an average way.

The basic magnitude modelling CX collisions is the volumetric rate

$$\zeta_{cx}(c_{ni}) = \sigma_{cx}(c_{ni})c_{ni}, \quad \boldsymbol{c}_{ni} = \boldsymbol{u}_i - \boldsymbol{u}_n \tag{16}$$

based on the $\sigma_{cx}$ the CX cross-section and the average drift velocity, $\boldsymbol{c}_{ni}$. The probability that a superion suffers a CX collision is

$$P_{cx} = 1 - \exp(-n_n\zeta_{cx}\Delta t). \tag{17}$$

Using a random number, the code decides if the collision takes place. In the affirmative case,

the new velocity of the superion is obtained randomly from the drifted Maxwellian function for neutrals already used in the preceding subsection. The effect of CX collisions on each superneutral is the resistive force

$$\boldsymbol{R}_{cx} = M_n n_i \zeta_{cx} \boldsymbol{c}_{ni}. \tag{18}$$

## 4.4  Injection of neutrals at the boundaries

Three different processes inject neutrals at different boundaries of the simulation domain: net injection of propellant from the feeding system at the anode, reflection of neutrals at the walls and recombination of ions at the walls. In addition, at the plume boundaries, there are losses of ions and neutrals and possible injection of ambient neutrals. For each process, wall panel, and time-step, HPHall-2 uses probability algorithms to determine the number of injected super-neutrals, and the location and injection velocity of each of them. Algorithm improvements have been implemented for the first three processes and are commented briefly next.

### 4.4.1  Injector

In general, the gas injector occupies several panels of the anode surface. The number of injected neutrals per panel is proportional to the anode gas flow $(\dot{m}_a)$, the time-step, and the area of the panel, and is inversely proportional to the total surface of the injector and the mass of a super-neutral at injection $(M_{n,\mathrm{inj}})$. At the injector, the gas distribution function is assumed to be a drifted Maxwellian of temperature $T_{\mathrm{inj}}$ and average velocity (normal to the injector) $u_{\mathrm{inj}}$. Then, the probability function for the velocity tangential to the injection surface is

$$p_t(\boldsymbol{v}_t) = \frac{m_i}{2\pi T_{\mathrm{inj}}} \exp\left(-\frac{m_i\|\boldsymbol{v}_t\|^2}{2T_{\mathrm{inj}}}\right), \qquad \boldsymbol{v}_t \in \mathbb{R}^2, \tag{19}$$

whereas the probability function for the normal velocity is based on the normal gas flux, [14, 15]

$$p_N(v_N) = \frac{\dfrac{m_i}{T_{\text{inj}}} v_N \exp\left(-\dfrac{m_i(v_N - u_{\text{inj}})^2}{2T_{\text{inj}}}\right)}{\exp\left(-\bar{u}_{\text{inj}}^2\right) + \sqrt{\pi}\bar{u}_{\text{inj}}\text{erfc}\left(-\bar{u}_{\text{inj}}\right)}, \qquad v_N \in [0, \infty[, \tag{20}$$

with $\bar{u}_{\text{inj}} = \sqrt{m_i u_{\text{inj}}^2/2T_{\text{inj}}}$.

### 4.4.2 Reflection and recombination at the walls

The distribution function for a neutral reflected from a wall panel is a semi-Maxwellian distribution of temperature

$$T_{emi} = a_w T_{wall} + (1 - a_w)T_{imp}, \qquad 2T_{imp} = \frac{\sum_p M_p v_p^3}{2\sum_p M_p v_p}, \tag{21}$$

where $a_w$ is an accommodation coefficient ($a_w = 0.8$ in the simulation examples of this paper), $T_{wall}$ is the wall temperature, $T_{imp}$ is the 'temperature' of the neutrals impacting the panel, and the summation index extends to all neutrals impacting the panel within a time-step.

Due to the mass disparity, the recombination of one superion at the wall cannot lead to the creation of one superneutral. Instead, HPHall-2 defines the probability of injecting back a super-neutral as the total mass of ions impacting one panel within a given timestep divided by $M_{n,\text{inj}}$. The point of injection within the panel is decided randomly and the probability function for the injection velocity is the same than for the reflection of neutrals, except that $T_{imp}$ in Eq.(21) is based now on the flux of impacting ions.

### 4.5 Weighting of plasma magnitudes

Once the mass, position and velocity of all ions and neutrals are known at instants $t + \Delta t$ or $t + \Delta t/2$, HPHall-2 proceeds to weight macroscopic magnitudes for each species at each node of the simulation grid. In order to distribute the properties of each superparticle among the

neighboring nodes, the code uses the weighting function

$$S_{jk}(\xi, \eta) = \begin{cases} (1 - |\xi'|)(1 - |\eta'|), & (\xi', \eta') \in I, \\ 0, & (\xi', \eta') \notin I, \end{cases} \tag{22}$$

with $\xi'$ and $\eta'$ defined in Eq. (5), and $I = [-1, 1] \times [-1, 1]$.

Density, particle flux, macroscopic velocity, pressure (tensor), and temperature (tensor) of a given species (ions or neutrals) at node $jk$ are computed from

$$n_{jk} = \frac{1}{m_i \Omega_{jk}} \sum_p S_{jk}(\xi_p, \eta_p) M_p, \tag{23}$$

$$\boldsymbol{g}_{jk} = \frac{1}{m_i \Omega_{jk}} \sum_p S_{jk}(\xi_p, \eta_p) M_p \boldsymbol{v}_p, \tag{24}$$

$$\boldsymbol{u}_{jk} = \boldsymbol{g}_{jk}/n_{jk}, \tag{25}$$

$$\bar{\bar{P}}_{jk} = \frac{1}{\Omega_{jk}} \sum_p S_{jk}(\xi_p, \eta_p) M_p (\boldsymbol{v}_p - \boldsymbol{u}_{jk})(\boldsymbol{v}_p - \boldsymbol{u}_{jk}), \tag{26}$$

$$\bar{\bar{T}}_{jk} = \bar{\bar{P}}_{jk}/n_{jk}, \tag{27}$$

respectively. Here, the summation index $p$ applies to all particles of the given species, $M_p$ is the mass of the superparticle, and

$$\Omega_{jk} = \int \int S(\xi, \eta) 2\pi r \left| \frac{\partial(z, r)}{\partial(\xi, \eta)} \right| d\xi d\eta, \tag{28}$$

is a volume associated to node $jk$. A new advantage of HPHall-2 is that $\Omega_{jk}$ takes cylindrical effects into consideration, thus avoiding errors at cells with small $r$ [17]. Some remarks must be made on the instant the above magnitudes are computed. The density $n_{jk}$, in Eq.(23), is computed at $t+\Delta t$, and the rest of magnitudes, Eqs.(24)-(27), are computed at $t+\Delta t/2$. When necessary, values of $n_{jk}$, $(\xi_p, \eta_p)$, and $M_p$ at $t + \Delta t/2$ are obtained from a linear interpolation between values at $t$ and $t + \Delta t$.

## 4.6 Definition of magnitudes at the boundaries

The original code HPHall used the same weighting function, $S_{jk}(\xi, \eta)$, Eq.(22), to compute magnitudes at nodes placed along the domain boundaries, but substituting interval $I$ by interval $J = I \cap D$, with $D$ the simulation domain (see Fig. 6 of Ref. [9]).

In Ref. [8] we showed that this one-side weighting yields ion velocities at the sheath boundaries much lower than the Bohm velocity and, as a consequence, very undeveloped radial profiles. In Ref. [9] we proposed two methods to define correctly magnitudes at the nodes:

(i) to correct the weighting algorithm,

(ii) to force the fulfillment of the Bohm condition.

In order to explain briefly these two procedures, let us determine the plasma density at a node of the inner-wall boundary, $(j, k) = (j, 0)$.

The corrected weighting algorithm is based on the fact that the linear one-side weighting does not yield $n_e|_{k=0}$ but $n_e|_{k=1/3}$ [9]. Assuming a linear variation of $n_e$ within the cells adjacent to the nodes, HPHall-2 computes the density at the boundary as

$$n_e|_{k=0} = n_e|_{k=1/3} - \frac{1}{2}(n_e|_{k=1} - n_e|_{k=1/3}). \tag{29}$$

The validity of this new weighting was demonstrated in Ref. [9]. However, it was also found that, since most plasma profiles present large gradients near the sheath boundaries, fine meshes must be used in order to obtain these large gradient profiles (and fulfill the Bohm condition on the ion flow).

The second algorithm proposed by Ref. [9] defines the density at the boundary as

$$n_e|_{k=0} = \frac{g_{Ni}|_{k=0}}{v_{Bohm}}, \tag{30}$$

where $g_{Ni}$ is the ion flux perpendicular to the wall and $v_{Bohm}$ is the Bohm velocity. In the present, provisional formulation, $g_{Ni}$ is obtained from a corrected weighting algorithm and the Bohm velocity is defined simply as $v_{Bohm} = \sqrt{T_e|_{k=0}/m_i}$. In spite of using such an

approximate expression for $v_{Bohm}$, Ref. [9] showed that Eq. (30) yields very good results even with coarse meshes. This suggests that accurate formulations of the Bohm-condition-forcing algorithm are the best way to compute plasma magnitudes at the nodes.

Koo et al. presented an alternative method to satisfy the Bohm condition in a similar hybrid code. In their model, the correction is only established in the anode, where the 1D electron fluid model, very similar to the one of HPHall, has difficulties. The main goal of their algorithm is satisfying the most general form of Bohm condition, Eq. (1), over the anode in a global way, not point by point. The algorithm is a linear controller that lows the potential near the anode in proportion to the difference between the right-hand side and the left-hand side of Equation (1). The necessary particle average is carried along all the program, and not each time step, in order to have enough statistical representativeness. This method has two main disadvantages when compare with the algorithms described in [9]. First, it is necessary to adjust the proportionality constant of the linear controller. If this method is applied to the lateral walls, it is possible that the constant should vary along the lateral walls. Second, it does not fix the origin of the problem, which is the incorrect weighting on the boundaries of the computational domain.

## 5    The electron subcode

The axisymmetric macroscopic equations of the electrons correspond to the strongly-magnetized, diffusive limit, which requires that

$$\omega_e \gg \nu_e, D/Dt, \tag{31}$$

where $\omega_e = eB/m_e$, $\nu_e$ is the effective collision frequency (defined below), and $D/Dt$ is the electron total time derivative.

The electron macroscopic model in HPHall2 is the one proposed by Fife [4] except for improvements on the sheath wall-collisionality models, based on the works of Ahedo [12] and Ahedo et al. [1], respectively. These are adapted to HPHall-2 in Appendixes A and B. The magnetic field introduces a large anisotropy in the transport properties of electrons. In order

to take advantage of it, vectorial variables and equations for electrons are projected in the directions parallel and perpendicular (in a meridian plane) to the magnetic field, $\mathbf{1}_{\parallel}$ and $\mathbf{1}_{\perp}$, defined in Eq. (8).

For the time interval $[t, t + \Delta t]$, the inputs of the electron subcode are the plasma and neutral densities, $n_e(z, r)$ and $n_n(z, r)$, and the ion flux density, $\boldsymbol{g}_i(z, r)$. The main outputs of the subcode are the electric potential and field, $\phi(z, r)$ and $\boldsymbol{E}(z, r)$, and the electron temperature, $T_e(z, r)$, within that time interval.

## 5.1 Ohm's and Fourier's laws

In the diffusive limit, the momentum equation reflects the equilibrium between the electric and magnetic forces, the electron pressure, and the resistive forces. In the magnetic-related reference frame, the three scalar momentum equations are

$$0 \simeq -\frac{\partial n_e T_e}{\partial \chi} + e n_e \frac{\partial \phi}{\partial \chi}, \tag{32}$$

$$0 = -m_e(\omega_e g_{\perp e} + \nu_{en} g_{\theta e}) + F_{\theta,ano} + F_{\theta,wall}, \tag{33}$$

$$0 = -r B \frac{\partial n_e T_e}{\partial \lambda} + e n_e r B \frac{\partial \phi}{\partial \lambda} + m_e \omega_e g_{\theta e}. \tag{34}$$

Here: $\boldsymbol{g}_e = n_e \boldsymbol{u}_e$ is the electron flux density; $\nu_{en}$ is the electron-neutral collision frequency (electron-ion collisions are disregarded); and $F_{\theta,ano}$ and $F_{\theta,wall}$ model the effects on the electron velocity of correlated plasma fluctuations (i.e., Bohm diffusion) and wall collisionality, respectively [1, 13, 18]. These two effects and the classical collisional forces are assumed smaller than the main forces, $|\nabla(n_e T_e) + e n_e \nabla \phi|$, and have thus been neglected in Eqs. (32) and (34).

Wall collisionality is commented in Appendix B. Exchanges of magnetized, primary electrons by unmagnetized, secondary ones at the lateral walls lead to a resistive force on the azimuthal electron flux, which can be expressed as

$$F_{\theta,wall} = -\nu_{wm} m_e g_{\theta e}, \tag{35}$$

with the characteristic frequency $\nu_{wm}$ defined in Eq. (A.17).

Janes and Lowder [18] showed that correlated fluctuations on the plasma density and the electric field leave an average azimuthal effect on the electrons, $F_{\theta,ano} \equiv < en'_e E'_\theta >$, and suggested that this is proportional to the main, axial force. Then, using Eq. (34) to substitute the axial force by $m_e \omega_e g_{\theta e}$, one has [1]

$$F_{\theta,ano} \simeq -\alpha_{ano} \omega_e m_e g_{\theta e}, \tag{36}$$

with $\alpha_{ano}$ the proportionality constant, which represents the relative level of fluctuations. Since there is yet no established theory of this anomalous diffusion phenomenon, $\alpha_{ano}$ is taken as an empirical parameter by HPHall-2.

Defining

$$\nu_e = \nu_{ano} + \nu_{wm} + \nu_{en} \tag{37}$$

as the total momentum collision frequency, Eq. (33) becomes

$$0 \simeq -\omega_e g_{\perp e} - \nu_e g_{\theta e}, \tag{38}$$

which relates $g_{\theta e}$ and $g_{\perp e}$. Substituting $g_{\theta e}$ into Eq. (34) one has

$$eg_{\perp e} = \frac{r\nu_e}{\omega_e} \left( -\frac{\partial n_e T_e}{\partial \lambda} + en_e \frac{\partial \phi}{\partial \lambda} \right), \tag{39}$$

which is the Ohm's law for the electron axial motion.

The vectorial equation for heat conduction, $\boldsymbol{q}_e$, is treated similarly to the momentum equation. Assuming that the mass and thermal diffusitivities are the same, and after some algebraic manipulation the heat conduction equation reduces to

$$0 \simeq -\omega_e q_{\perp e} - \nu_e q_{\theta e}, \tag{40}$$

$$q_{\perp e} = -\frac{5}{2} n_e T_e \frac{r\nu_e}{e\omega_e} \frac{\partial T_e}{\partial \lambda}. \tag{41}$$

$$0 \simeq -\frac{\partial T_e}{\partial \chi}, \tag{42}$$

Equation (40) relates $q_{\theta e}$ and $q_{\perp e}$, Eq. (41) is the Fourier's law for the perpendicular dynamics, and Eq. (42) sets that $T_e$ is constant along any magnetic streamline.

Using this last result, we obtain a first integral of Eq. (32):

$$e\phi(\lambda, \chi) = e\phi^*(\lambda) + T_e(\lambda) \ln \frac{n_e(\lambda, \chi)}{n_0} \tag{43}$$

where $\phi^*$ is called the thermalized electric potential [13] and $n_0$ is a convenient constant. The substitution of $\phi$ into the Ohm's law (39) yields

$$g_{\perp e} = n_e \frac{r\nu_e}{e\omega_e} \left[ (\ln \frac{n_e}{n_0} - 1)\frac{\partial T_e}{\partial \lambda} + e\frac{\partial \phi^*}{\partial \lambda} \right], \tag{44}$$

which relates $g_{\perp e}$ to the derivatives of $T_e(\lambda)$ and $\phi^*(\lambda)$.

## 5.2  Conservation of particles and energy

The conservation equations for the electrical current can be written as

$$\nabla \cdot (\boldsymbol{g}_i - \boldsymbol{g}_e) = 0 \tag{45}$$

The present version of HPHall-2 admits only dielectric lateral walls. Then, the integration of Eq. (45) across any streamsurface connecting the inner and outer walls, $S : \lambda = \text{const}$, yields

$$\int_S e(g_{\perp i} - g_{\perp e})dS = \text{const} = I_d, \tag{46}$$

where $I_d(t)$ is the discharge current (which is a given parameter here). Substituting $g_{\perp e}$ from Eq. (44), one has

$$e\frac{\partial \phi^*}{\partial \lambda} \int_S n_e \frac{r\nu_e}{\omega_e}dS = \frac{\partial T_e}{\partial \lambda} \int_S n_e \frac{r\nu_e}{\omega_e}(1 - \ln \frac{n_e}{n_0})dS + \left( \int_S eg_{\perp i}dS - I_d \right), \tag{47}$$

which yields $\partial \phi^*/\partial \lambda$ in terms of $\partial T_e/\partial \lambda$ and $I_d$.

Finally, the electron energy equation is written as

$$\frac{\partial}{\partial t}\left(\frac{3}{2}n_e T_e\right) + \nabla \cdot \boldsymbol{q}_e^{tot} = -e\boldsymbol{g}_e \cdot \boldsymbol{E} - \dot{n}_i \alpha_i E_i, \tag{48}$$

where $\boldsymbol{q}_e^{tot} = \frac{5}{2}T_e\boldsymbol{g}_e + \boldsymbol{q}_e$ is the total (convective plus conductive) flux of enthalpy, and

$$\alpha_i(T_e/E_i) = 2.0 + 0.254 \exp\left(0.677 E_i/T_e\right) \tag{49}$$

is Dugan's expression of the ionization cost factor (for xenon), which takes into account excitation/radiation processes. Electron energy losses due to elastic collisions are much lower than Joule heating and have been disregarded in Eq. (48).

A partial differential equation for $T_e(\lambda, t)$ is obtained by integrating the energy equation on finite volume elements centered on the streamlines, $\lambda_l, l = 1, 2, \dots$. Using the nomenclature of Fig. 1, one has

$$\int_{\Delta V} dV \left(\frac{3}{2}\frac{\partial n_e T_e}{\partial t} - eg_{\perp e}rB\frac{\partial \phi}{\partial \lambda} + \dot{n}_i \alpha_i E_i\right) + \int_{S_3 \cup S_4} q_{Ne}^{tot} dS =$$
$$- \int_{S_1 \cup S_2} q_{\perp e}^{tot}\boldsymbol{1}_\perp \cdot \boldsymbol{dS}, \tag{50}$$

where the direction of $\boldsymbol{dS}$ is outwards of the volume element,

$$q_{\perp e}^{tot} = \frac{5}{2}n_e T_e \frac{r\nu_e}{e\omega_e}\left[(\ln \frac{n_e}{n_0} - 2)\frac{\partial T_e}{\partial \lambda} + e\frac{\partial \phi^*}{\partial \lambda}\right], \tag{51}$$

and $q_{Ne}^{tot}$ measures the energy lost at the lateral boundaries per unit of area. Inside the chamber, this is the energy lost into the lateral sheaths, and is given by Eq. (A.8).

The work of the electric field along the magnetic lines $eg_{\parallel e}\partial\phi/\partial\chi$ has been neglected in Eq. (50) since it is much smaller than $q_{Ne}^{tot}$ and the work of the perpendicular component $E_\perp$. [An additional, practical reason to disregard it, is to avoid the cost of computing $g_{\parallel e}$ and $\partial\phi/\partial\chi$ at each timestep.]

## 5.3 Integration procedure

The substitution of Eqs. (41),(43),(44), and (47), into Eq. (50) yields an integral equation involving only $T_e(\lambda, t)$, its derivatives, and parameters and variables that are inputs of the particle subcode. Equation (6) provides the variable transformation needed to solve the volume and surface integrals. Volume integrals use the value of the integrand at the intermediate surface $S : \lambda = \lambda_l$, Fig. 1. Thus, one ends with an equation of the form

$$\left[ C_1 + C_2 \frac{\partial T_e}{\partial t} + C_3 T_e \frac{\partial T_e}{\partial \lambda} + C_4 \left( \frac{\partial T_e}{\partial \lambda} \right)^2 \right]_S = \left[ C_5 T_e + C_6 T_e \frac{\partial T_e}{\partial \lambda} \right]_{S_1} + \left[ C_7 T_e + C_8 T_e \frac{\partial T_e}{\partial \lambda} \right]_{S_2} \quad (52)$$

where the coefficients $C_j, (j = 1, ..., 8)$ are integrals involving plasma variables at $S$, $S_1$, or $S_2$. For instance

$$C_2(\lambda) = \frac{3}{2} \int_{\Delta V} n_e dV. \quad (53)$$

Equation (52) is discretized and solved as in Ref. [4]. Finite-differences evolution equations for $T_e$ at the selected mesh of $\lambda_l$ lines are obtained. Numerical stability reasons dictate that the timestep used to integrate these equations in one PIC time-interval, $\Delta t$, is $\delta t \sim 10^{-3} - 10^{-2} \Delta t$. However, coefficients $C_j$, $\phi^*(\lambda)$ [Eq. (47)], and $\phi(\lambda, \chi)$ [Eq. (43)], although dependent on $T_e$, are computed only once for the whole interval $\Delta t$.

The above scheme yields $T_e$ and $\phi$ between two magnetic streamlines, one intersecting the cathode and the second one close to anode. If the first magnetic streamline is curved, between it and the anode, there are a quasineutral region and a space-charge sheath. The sheath potential drop, $\phi_{AB} = \phi_B - \phi_A$, satisfies [19]

$$\phi_{AB} = \frac{T_{eB}}{2e} \ln \frac{T_{eB} n_{eB}^2}{2\pi m_e g_{NeB}^2} \quad (54)$$

where magnitudes at B represent average values at the anode boundary of the numerical domain, and $g_{Ne}$ means flux perpendicular to the anode. Then, linear interpolations of are used to define plasma magnitudes in the near-anode quasineutral region [4].

The discharge potential, $V_d(I_d)$, fulfills

$$V_d = \phi_B - \phi_{cat} - \phi_{AB}. \tag{55}$$

If $V_d$ is an input parameter (and invariant with $t$, commonly), the discharge current, $I_d$, is an output parameter (and changes with $t$) and a Newton's iteration algorithm must be used on $I_d$. In each iteration, Eq. (52) must be integrated again for the interval $\Delta t$; in general, 2 or 3 of these iterations are enough to converge.

## 6    Results

This section presents computational results obtained with HPHall-2 for two cases: Case 1 corresponds to the same thruster geometry and magnetic field topology defined in Fig. 1 of our previous work, Ref. [9]. This case uses a simple geometry and takes $B_z = 0$ (violating irrotationality) in order to isolate 2D effects due exclusively to the plasma-wall interaction and to facilitate the comparison with the macroscopic model of Ahedo et al. [1]. Case 2 is sketched in Fig. 1 and corresponds to the SPT-70 thruster as modelled by Fife in Ref. [4]. Figures 2-7 are for Case 1 and Figures 8 and 9 are for Case 2. Spatial plots correspond to time-averaged values over an intervals that exclude initial transients. Table 1 shows control parameters and (time-averaged) thruster performances for both cases. Cases 1 and 2 are just for demonstration of the last advances made on the code, its capabilities, and its limitations. In particular, Case 2 has not been either adjusted or checked to reproduce a real operation condition.

Figures 2-7 complete the results shown in Ref. [9], which were dedicated mainly to the fulfillment of the Bohm condition at the lateral walls Figure 2 illustrates the same issue at the anode sheath transition (that is, $\xi = 1$ or point B). As for the lateral walls, the correct weighting of ion magnitudes at point B leads to larger reverse ion velocities and lower plasma densities than in the original version of the code. Consistent with this, the point of maximum electric potential moves away from the anode sheath and the ion backflow region becomes clearly observable. The sheath potential drop is now about 3V, instead of $\sim 15$ V with the

20

original version, the difference being due to the different value of $n_{eB}$ and to use a more correct expression, Eq. (54) for $\phi_{AB}$. Although the improvement of the near-anode region is relevant locally, it has a weak global effect (in this case) on the time-averaged thruster performances. The relevance of that zone on thruster oscillations remains to be studied.

Since the code does not use symmetric algorithms for creation/destruction of superneutrals and superions [for instance, see Eqs. (14) and (15) for ionization], the conservation of the plasma mass along the thruster channel must be checked. Figure 3 shows the ion and neutral flows at different axial locations along the chamber, $\dot{m}_i$ and $\dot{m}_n$. The sum of both is the total mass flow $\dot{m}(z)$ and we verify that it is practically conserved inside the thruster; the defect of neutrals in the near-plume is due to losses into the vacuum. The reverse ion flow to the anode is just a small fraction of the emitted mass flow, $\dot{m}_A$. The dashed line of Fig. 3 plots the cumulative ion losses due to recombination at the lateral walls, $\dot{m}_{i,\text{wall}}(z)$. As we showed in Ref. [9], the correct weighting at the boundaries increases the ion losses to the lateral walls with respect to the original code (by a factor of 2.2 for this case).

When studying the effect of ion-neutral collisions, no major difference has been detected in the global performance of the thruster. This is in total agreement with the known data. However, it does not mean that simulating the collisions is not interesting; the influence of charge-exchange collisions must be more noticeable when HPHall is used as a source program for plume simulation [20].

Two dimensional contours of the electric potential, the plasma density, and the neutral density for Case 1 were shown in Fig. 11 of Ref. [9] Figure 4(a) shows the electron temperature, $T_e(z)$, and the outer-sheath potential drop, $\phi_{WQ}(z)$, when the improved sheath model is used. Figure 4(b) plots the axial distribution of the energies spent on the ion and electron interactions with the lateral walls, and on ionization. In the near-plume the inwards electron flow is Joule-heated. At the chamber exit, the large electron temperature brings the SEE yield to 95%, the lateral sheaths are near charge saturation, and electron energy losses are enormous there, and start to cool the electron fluid. Heat conduction effects are responsible of placing the electron temperature peak outside the chamber instead of at the exit. Notice the high sensitivity of energy wall losses to the electron temperature and the comparison with

ionization losses. For Case 1, energy wall losses represent a 39% of the available power, and ionization losses a mere 18%. The useful power is computed as the total energy flow of heavy species at the downstream end of the domain. The sheath potential drop, $\phi_{WQ}(z)$, is large even for a sheath near to charge saturation. Wall energy losses of ions and electrons take into account that the sheath potential increments the kinetic energy of the ions impacting the wall and, then, the wall erosion.

The effect of wall collisionality is evaluated in Fig. 5 where the different contributions to the effective electron collision frequency, $\nu_e(z)$ in Eq. 37, are compared at different axial locations. Contrary to particle and energy losses into the lateral walls, wall collisionality appears as a marginal effect even at the chamber exit where SEE is 95%. Classical collisions dominate near the anode and fluctuation-based diffusion in the rest of the chamber. These results are based on a value of $\alpha_{ano}$ which is impossible to confirm, but it must be noticed that the modification of the above conclusions would require to decrease $\alpha_{ano}$ by a factor of 10 roughly. Wall collisionality effects could be more relevant at high-potential operation, where SEE effects are even larger than here.

Figure 6(a) plots the scalar ion temperature, $T_i = \text{trace}(\overline{\overline{T_i}})/3$, as computed from the temperature tensor, $\overline{\overline{T_i}}$. The main contribution comes out from the zz-component: $T_i \sim T_{zz,i}/3$. The high value of this ion velocity dispersion contrasts with the results of the stationary, macroscopic model of Ref. [1]. The explanation is that the dispersion here is not caused by the extended ionization region but by the large temporal fluctuations of the electric potential at any spatial location. This is illustrated in Figure 6(b), which plots the temporal variation of $\phi$ at a particular point of the channel exit, and shows oscillations of 50V over a mean value of 150V, roughly.

Numerical codes are expected to be very useful to understand the mechanisms setting up the large variety of plasma oscillations arising in Hall thrusters. At the same time, caution must be taken in distinguishing numerical from physical fluctuations. Figure 7(a) and (b) illustrate these two aspects. The two curves plot the temporal variation of the discharge current when using either the corrected-weighting or Bohm-condition forcing algorithms at the domain boundaries. In both curves we identify a main oscillation mode of $\sim 16$ kHz,

a high-frequency mode of ∼150 kHz, and possibly a low-frequency mode of ∼1 kHz. No investigation has been made on the nature of these fluctuations, but it is very likely that the first two modes correspond to the well-reported, breathing and ion-transit instabilities, respectively [21]. A low-frequency mode, modulating the amplitude of the main mode, has been identified also with the time-dependent, macroscopic model of Ref. [22]. On the other hand, the two curves of Fig. 7 demonstrate that the fluctuation level can be very influenced by the numerical algorithm we are implementing (for the weighting at the boundaries, in this case). The relative amplitude of the high-frequency mode is a 15% when applying the Bohm-condition forcing and just a 5% with the corrected-weighting algorithm. The amplitude of the main mode is also slightly higher with the Bohm-condition forcing. This can be due to the more extrinsic character of this algorithm.

The computations for Case 2 confirm the trends and conclusions obtained for Case 1. Figure 8 plots 2D contour maps of the main plasma magnitudes. The irrotational magnetic field was plotted in Fig. 1; it presents a peak value of 350 Gauss near the the exit of the channel, and a value of the order of 10 Gauss at the anode. The 2D maps can be compared with figures 5.30 to 5.34 of Ref. [4]. The profiles here are more symmetrical with respect to the channel mid-section than in the original version. Here, the radial variation of the potential profile is more pronounced and more independent of the curvature of the magnetic streamlines. The correction of the plasma-wall interaction affects also the radial variation of $n_n$ too, which is more pronounced due to the larger ion recombination.

Figure 9 plots the $z - r$ projection of the ion velocity vectors, where we stand out (i) the region of ion backflow and (ii) the ions that are going to recombine at the lateral walls. Notice that we are plotting the ion velocities at the lateral boundaries of the domain, which are less than the velocity of impact at the walls because of the sheath radial acceleration (for instance, a sheath potential drop of 50V increases the ion radial velocity in more than 8 km/s).

## Acknowledgments

## A    The lateral sheath model

HPHall-2 implements the sheath model developed by Ahedo [12], which takes into account both the presence of secondary electron emission(SEE) and the sheath charge saturation on ceramic walls. The consequence of charge saturation is that the electron-repelling sheath vanishes never.

The collisionless sheath model is valid as long as the Debye length is the smallest length of the problem. Inside the sheath, only gradients perpendicular to the wall are relevant and magnetic field effects are negligible. Although the model of [12] was developed assuming a macroscopic model for the ions, it is fully applicable to the present case if the ion velocity dispersion at the entrance to the sheath is small compared to the electron temperature. A central feature of the model is to consider primary and secondary populations (subscripts $p$ and $s$) within the sheath but a single electron population (subscript $e$) in the quasineutral plasma (which implicitly means that secondary electrons are trapped and merged in the bulk of the discharge).

Figure 1 of Ref. [12] sketches the sheath model (for the common case of cylindrical walls). Point Q represents the sheath transition, which is the boundary of the (quasineutral) simulation domain. As input parameters at Q, the sheath model needs the plasma density $n_{eQ}$, the electron temperature $T_{eQ}$, and the ion flux perpendicular to wall and sheath, $g_{NiQ}$, with subscript $n$ meaning perpendicular to the lateral boundary.

In addition the present model assumes that the distribution function of the $p$-population at Q, $f_{pQ}$, is Maxwellian (except for the tail of electrons non-reflected from the wall W). At

the wall W, the effective SEE yield function is

$$\delta_w \equiv \frac{g_{sW}}{g_{pW}} = \frac{\int_{w_N>0} \bar{\delta}_w(w) w_N f_{pW}(\boldsymbol{w}) d^3\boldsymbol{w}}{\int_{w_N>0} w_N f_{pW}(\boldsymbol{w}) d^3\boldsymbol{w}} \qquad (A.1)$$

where $f_{pW}$ is the distribution function close to the wall, $\bar{\delta}_w(w)$ is the yield of particles of velocity $w$. Expressions of the form

$$\bar{\delta}_w(w) = \delta_{w0} + (1 - \delta_{w0}) \left( \frac{m_e w^2}{2E_1} \right)^p \qquad (A.2)$$

are used generally [2, 7], with parameters $\delta_{w0}$, $p$, and $E_1$ (energy yielding 100% SEE) modeling the properties of the wall material. For $f_{pW}$ semi-Maxwellian of temperature $T_p$, one has

$$\delta_w(w) = \delta_{w0} + (1 - \delta_{w0})(T_p/T_1)^p \qquad (A.3)$$

with $T_1 = E_1/\Gamma(2+p)^{1/p}$ [7]. The energy of secondary electrons, when emitted by the wall, is considered negligible compared to the energy they acquire from the sheath potential, $e\phi_{WQ}$.

For a ceramic wall, the zero net current condition applies at point Q. Therefore, the electron fluxes at the sheath boundary satisfy

$$g_{NeQ} = g_{NpQ} + g_{NsQ} = g_{NiQ}. \qquad (A.4)$$

To evaluate the rest of quantities, let us consider first the regime without charge saturation. The expressions for the sheath potential drop, the density of secondary electrons at point Q, and the temperature of the $p$-population are [12]

$$\phi_{WQ} \simeq \frac{T_p}{e} \ln \left[ (1 - \delta_w) \sqrt{\frac{m_i}{2\pi m_e}} \right], \qquad (A.5)$$

$$n_{sQ} \simeq \frac{\delta_w g_{NiQ}}{(1 - \delta_w)\sqrt{2e\phi_{WQ}/m_e}}, \qquad (A.6)$$

$$T_p = T_{eQ} \left[ 1 - \frac{n_{sQ}}{n_{eQ}} \left( 1 + \frac{T_p}{2e\phi_{WQ}} \right) \right], \qquad (A.7)$$

respectively; an iterative process on $T_p$ is needed in order to solve these equations.

The electron (total) energy flux *into the sheath* can be expressed as

$$q_{Ne}^{tot} = g_{NiQ}T_{eQ}\beta_e, \qquad \beta_e(T_{eQ}) = \frac{T_p}{T_{eQ}}\left(\frac{2}{1-\delta_w} + \frac{e\phi_{WQ}}{T_p}\right). \tag{A.8}$$

(The energy flux *into the wall* does not include the term $e\phi_{WQ}g_{NeQ}$, which is the energy transmitted to the ions within the sheath.)

The sheath saturates when the electric field at the wall becomes zero. This takes place at [10]

$$\delta_w = \delta_w^* \equiv 1 - 8.3\sqrt{m_e/m_i}, \tag{A.9}$$

which yields $\delta_w^* \simeq 0.983$ for xenon. The rest of magnitudes at the charge-saturation limit (superscript $^*$) are obtained from substituting $\delta_w^*$ in preceding expressions. Thus, one has

$$\frac{g_{NsQ}^*}{g_{NiQ}} \simeq 60, \qquad \frac{T_{eQ}^*}{T_p^*} \simeq 1.16, \qquad \frac{e\phi_{WQ}^*}{T_{eQ}^*} \simeq 0.88, \tag{A.10}$$

and $T_p^*(T_1)$ comes from Eq. (A.3).

For $T_{eQ} > T_{eQ}^*$, the sheath is charge-saturated. A potential well is formed near the wall in order to reflect back the 'excess' of secondary flux, $(\delta_w - \delta_w^*)g_{spW}$. Since the potential well is of the order of the local energy of the secondary electrons, it can be neglected. As a consequence the relations

$$\frac{g_{NsQ}}{g_{NiQ}} \simeq 60, \qquad \frac{e\phi_{WQ}}{T_{eQ}} \simeq 0.88, \qquad \frac{q_{Ne}^{tot}}{g_{NiQ}T_{eQ}} \simeq 105, \tag{A.11}$$

apply for the charge saturation regime. and the sheath vanishes never. Instead, in the charge saturation regime the sheath potential grows linearly with $T_{eQ}$.

For the computations of this work we used $\delta_{w0} = 0$, $p = 0.576$ and $E_1 = 47.6$ in Eq. (A.2). This yields $T_1 = 26.4\text{eV}$, $T_p^* = 25.6\text{eV}$, and $T_e^* = 29.8\text{eV}$.

# B    Wall collisionality

Secondary-emitted electrons enter into the quasineutral plasma with no azimuthal velocity, whereas the plasma losses the azimuthal momentum of primary electrons collected by the walls. This modifies the azimuthal velocity of the total electron population ($e$) in two ways: first, there is a reduction of the average value of $u_{\theta e}$ over any streamline; and second, there is a modulation of $u_{\theta e}$ as the magnetic field modifies the radial trajectory of the secondary electron beams, an effect known as near-wall conductivity [23]. Here, only an estimate of the first effect is presented.

The azimuthal component of the momentum equation (divided by $m_e$) can be expressed as

$$\frac{\partial g_{\theta e}}{\partial t} + \nabla \cdot \boldsymbol{u}_e g_{\theta e} + \frac{u_{re} g_{\theta e}}{r} = -\omega_e g_{\perp e} - \nu_{en} g_{\theta e}. \tag{A.12}$$

Integrating it over the finite volume elements of Fig. 1, one has

$$\int_{S_3 \cup S_4} \frac{g_{\theta e} g_{Ne}}{n_e} dS + \int_{S_1 \cup S_2} \frac{g_{\theta e} g_{\perp e}}{n_e} \boldsymbol{1}_\perp \cdot \boldsymbol{dS} = -\int \left[ \omega_e g_{\perp e} + \nu_{en} g_{\theta e} + \frac{u_{re} g_{\theta e}}{r} + \frac{\partial g_{\theta e}}{\partial t} \right] dV. \tag{A.13}$$

Neglecting what we expect to be second order effects in this equation, one has

$$g_{\theta e} \left[ \frac{g_{Np} \Delta A}{n_e} \right]_{S_3 \cup S_4} + g_{\theta e} \int_{S_1 \cup S_2} \frac{g_{\perp e}}{n_e} \boldsymbol{1}_\perp \cdot \boldsymbol{dS} \sim -[\omega_e g_{\perp e} + \nu_{en} g_{\theta e}] \Delta V, \tag{A.14}$$

where $\Delta A$ and $\Delta V$ mean area and volume. For the remaining integral, the continuity equation yields

$$\int_{S_1 \cup S_2} \frac{g_{\perp e}}{n_e} \boldsymbol{1}_\perp \cdot \boldsymbol{dS} \sim -\left[ \frac{g_{Ne} \Delta A}{n_e} \right]_{S_3 \cup S_4}. \tag{A.15}$$

Notice in Eq. (A.14) that only $p$-electrons contribute to the net azimuthal momentum lost into the lateral walls, whereas the net electron flux to the walls is present in Eq. (A.15). Using these two last equations, one has

$$0 = -m_e(\omega_e g_{\perp e} + \nu_{en} g_{\theta e}) + F_{\theta,wall}, \tag{A.16}$$

27

where losses of azimuthal flux are represented by the force $F_{\theta,wall} = -\nu_{wm} m_e g_{\theta e}$ with

$$\nu_{wm} \sim \frac{1}{\Delta V} \left[ \frac{g_{Ns}\Delta A}{n_e} \right]_{S_3 \cup S_4}. \tag{A.17}$$

This expression confirms that there is no effect of the walls on $g_{\theta e}$ when there is no secondary emission.

## References

[1] E. Ahedo, J. Gallardo, and M. Martínez-Sánchez, Physics of Plasmas **10**, 3397 (2003).

[2] S. Barral, Z. Peradzynski, K. Makowski, and M. Dudeck, An alternative theory of transit-time oscillations in Hall thrusters, in *28th International Electric Propulsion Conference, Toulouse, France*, IEPC 03-, Electric Rocket Propulsion Society, Cleveland, OH, 2003.

[3] J. J. Szabo, *Fully kinetic numerical modeling of a plama thruster*, PhD thesis, Massachusetts Institute of Technology, 2001.

[4] J. M. Fife, *Hybrid-PIC Modeling and Electrostatic Probe Survey of Hall Thrusters*, PhD thesis, Massachusetts Institute of Technology, 1998.

[5] G. Hagelaar, J. Bareilles, L. Garrigues, and J. Boeuf, Journal of Applied Physics **91**, 5592 (2002).

[6] J. Fife and M. Martínez-Sánchez, Two-dimensional hybrid particle-in-cell (PIC) modelling of Hall thrusters, in *24th International Electric Propulsion Conference, Moscow, Russia*, IEPC 95-240, Electric Rocket Propulsion Society, Cleveland, Ohio, 1995.

[7] J. Fife, M. Martínez-Sánchez, and J. Szabo, A Numerical Study of Low-Frequency Discharge Oscillations in Hall Thrusters, in *33rd Joint Propulsion Conference, Seattle, WA*, AIAA 97-3052, American Institute of Aeronautics and Astronautics,Washington, DC, 1997.

[8] F. Parra, E. Ahedo, M. Martínez-Sánchez, and J. Fife, Improvement of the plasma-wall model on a fluid-PIC code of a Hall thruster (to be published), in *SP-555: 4th Spacecraft*

*Propulsion Conference, Sardinia (Italy)*, Noordwijk, The Netherlands, 2004, European Space Agency.

 [9] F. Parra and E. Ahedo, Fulfillment of the bohm condition on the HPHall fluid-PIC code, in *40th Joint Propulsion Conference, Fort Lauderdale, FL*, AIAA 2004-3955, American Institute of Aeronautics and Astronautics,Washington, DC, 2004.

[10] G. Hobbs and J. Wesson, Plasma Physics **9**, 85 (1967).

[11] L. Jolivet and J.-F. Roussel, Effects of the secondary electron emission on the sheath phenomenon in a Hall thruster, in *SP-465: 3rd Spacecraft Propulsion Conference, Cannes(Francia)*, pp. 367–376, Noordwijk, The Netherlands, 2000, European Space Agency.

[12] E. Ahedo, Physics of Plasmas **9**, 4340 (2002).

[13] A. Morozov, Y. Esipchuk, G. Tilinin, A. Trofimov, Y. Sharov, and G.Y.Shchepkin, Soviet Physics-Tech. Physics **17**, 38 (1972).

[14] C. Birdsall and A. Langdon, *Plasma Physics via Computer Simulation*, Institute of Physics Publishing, Bristol, 1991.

[15] G. Bird, *Molecular gas dynamics and the direct simulation of gas flows*, Clarendon Press, Oxford, 1994.

[16] M. Mitchner and C. K. Jr., editors, *Partially ionized gases*, Wiley, 1973.

[17] J. Verboncoeur, J. Computational Physics **174**, 421 (2001).

[18] G. Janes and R. Lowder, Physics of Fluids **9**, 1115 (1966).

[19] E. Ahedo, J. Gallardo, and M. Martínez-Sánchez, Physics of Plasmas **9**, 4061 (2002).

[20] M. Celik, M. Santi, S. Cheng, M. Martínez-Sánchez, and J. Peraire, Hybrid-PIC simulation of a Hall thruster plume on an unstructured grid with DSMC collisions, in *28th International Electric Propulsion Conference, Toulouse, France*, IEPC-03-134, Electric Rocket Propulsion Society, Cleveland, OH, 2003.

[21] S. Barral, K. Makowski, Z. Peradzynski, N. Gascon, and M. Dudeck, Phys. Plasmas **10**, 4137 (2003).

[22] A. Molina, V. Lapuerta, and E. Ahedo, Time-dependent model of the Hall thruster discharge, in *39th Joint Propulsion Conference, Huntsville, AL*, AIAA 2003-4856, American Institute of Aeronautics and Astronautics, Washington, DC, 2003.

[23] A. Bugrova, A. Morozov, and V.K.Kharchevnikov, Sov. J. Plasma Physics **16**, 849 (1990).

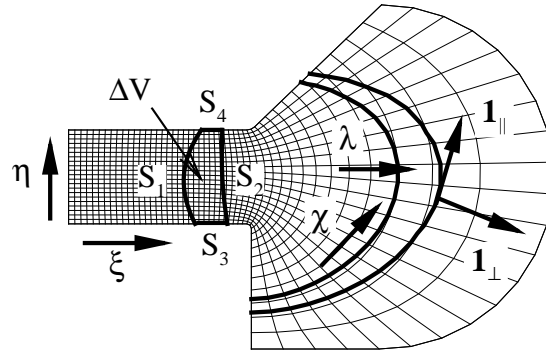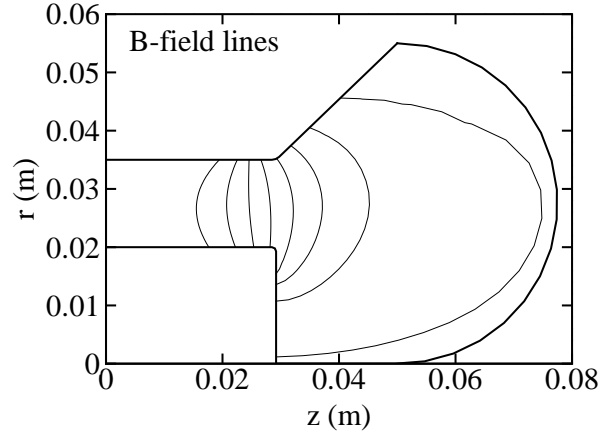| | |
|---|---|
| $I_d V_d$ | 535 W |
| $P_{\text{wall}}$ | 206 W |
| $P_{\text{ion}}$ | 64 W |
| $P_{\text{use}}$ | 234 W |

Table 1: Power losses and useful power.





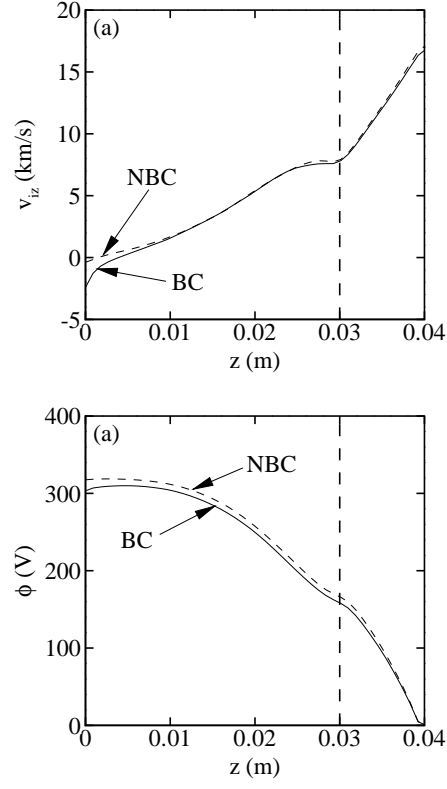Figure 1: Meshes, unit vectors, variables.

Figure 2: Effects of correcting the weighting of ion magnitudes at the anode boundary. The vertical dashed line represents the exit of the chamber. Solid and dashed lines correspond to the present and original code, respectively. Axial profiles at $r = 0.027$ m of (a) the ion axial velocity and (b) the electric potential.
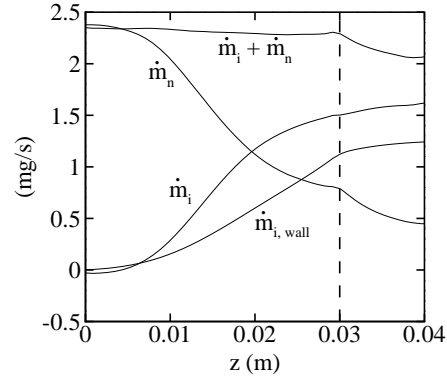


Figure 3: Axial variation of ion and neutral flows. The dashed line shows the cumulative ion flow lost to the lateral walls.
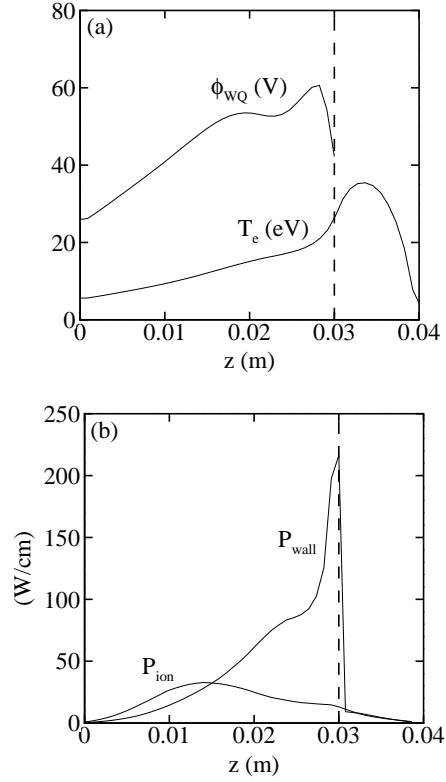
Figure 4: Axial profiles of the electron temperature, $T_e$, the potential drop at the outer sheath, $\phi_{WQ}$, the energy losses at the walls of ions and electrons, $Q_{wall,i}$ and $Q_{wall,e}$, and the ionization losses, $Q_{ion}$.
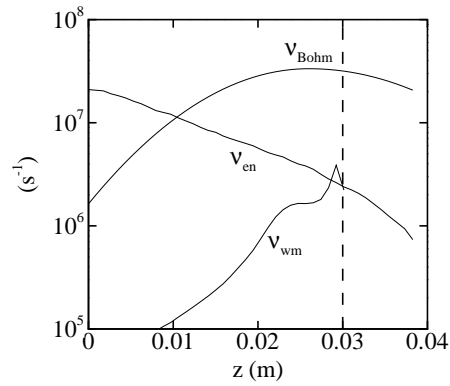


Figure 5: Axial profiles of the different contributions to the total collision frequency of the electron fluid at the channel radial mid-section. The anomalous diffusion parameter is $\alpha_{ano} = 1/80$.
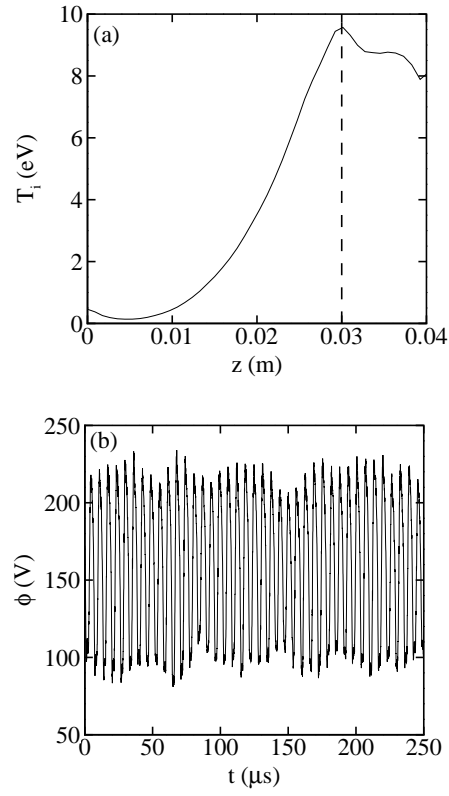
Figure 6: (a) Axial profile of the ion scalar temperature. (b) Temporal behavior of the electric potential at $z = 0.03$ m and $r = 0.0275$ m.
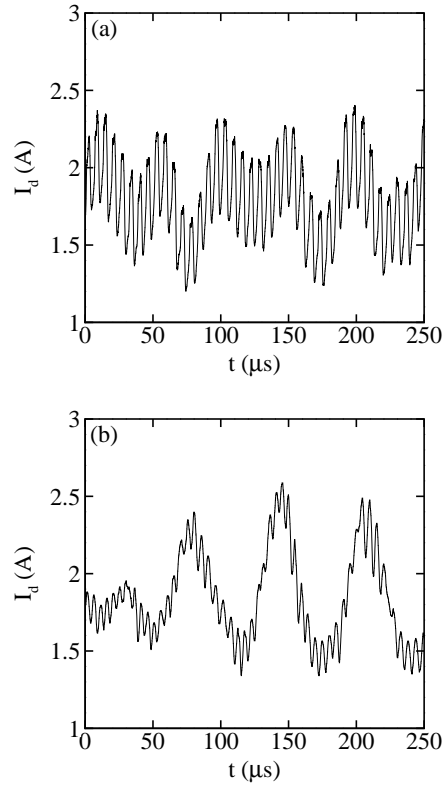
Figure 7: Temporal evolution of the discharge current when (a) the Bohm condition forcing or (b) the corrected weighting algorithm are used by the code.
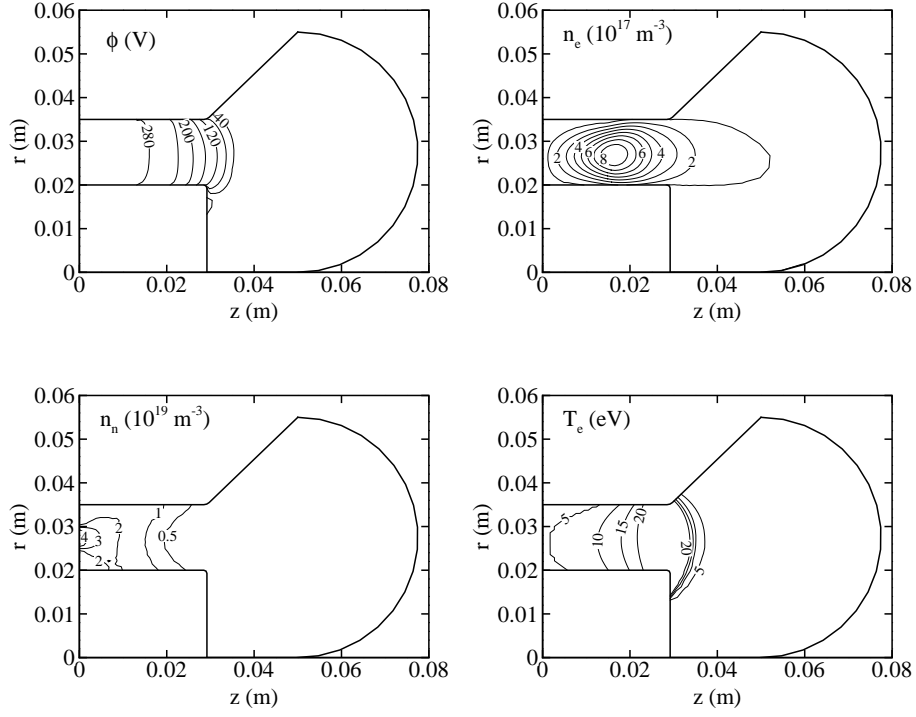
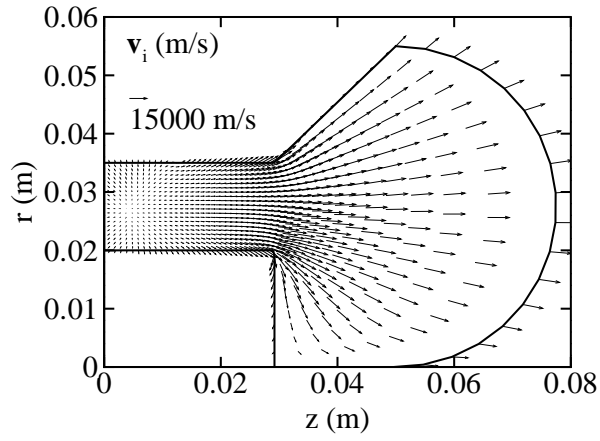Figure 8: Two dimensional contour levels for the SPT-70 thruster, as modelled in Ref. [4].



Figure 9: Ion velocity vectors (projected on the $z-r$ plane) for Case 2.

# Influence of design and operation parameters on Hall thruster performances

E. Ahedo and D. Escobar

*ETSI Aeronáuticos, Universidad Politécnica de Madrid, 28040 Madrid, Spain*

A stationary, macroscopic model [E. Ahedo, J. Gallardo, and M. Martínez-Sánchez, Phys. Plasmas 10, 3397 (2003)] is used to carry out parametric investigations on the effects of (i) the discharge voltage, (ii) the gas flow rate, (iii) the axial gradient of the magnetic field, and (iv) the chamber length on the Hall thruster performances and the axial structure of the plasma discharge. The high-thrust and high-specific-impulse modes for dual-mode thrusters are compared too. The results of the simulations agree well with the main tendencies observed in different experiments. The interaction among the several physical phenomena is discussed and useful scaling laws are proposed. Special attention is paid to understand (i) the adjustment of the magnetic field strength with the discharge voltage for optimum operation, (ii) the effect of the magnetic field shape, (iii) the dimensions of the different regions of the discharge, and (iv) the parameter trends needed to increment the propulsive and ionization efficiencies (the product of which determines the thrust efficiency). © *2004 American Institute of Physics.* [DOI: 10.1063/1.1759790]

## I. INTRODUCTION

Hall effect thrusters have flown on board USSR satellites since 1972.[1] With the fall of the USSR, the Western countries discovered the maturity of Soviet technology and its excellent suitability for secondary propulsion tasks on geostationary (GEO) satellites, and started to launch ambitious programs of research and development on Hall thrusters.[3–5,7] A significant part of this research has been directed to improve the knowledge of the physical processes and main parameters governing the thruster response. Although a fairly good understanding exists at present on its principles of operation,[8–10] there are still important uncertainties regarding both some plasma phenomena (such as the plasma interaction with the chamber walls, the anomalous electron mobility, and the stability of the discharge) and the influence of the different geometrical and operational parameters on the thruster performance. A consequence of these uncertainties is that most current prototypes still follow closely the basic design characteristics established by the flight-proven USSR thrusters.

Experimental tests have increased extraordinarily over the last decade and are providing very useful data.[11–14,16,17,19–24,26] However, it can be extremely difficult to obtain accurate and detailed measurements of some plasma magnitudes. Furthermore, the complexity of the phenomena involved and the technical constraints explain that the observed operational trends differ sometimes from one experiment to another. Therefore, theoretical and simulation efforts, as the one aimed with this paper, are needed to complement that empirical knowledge.

The work we present here is based on the model of the axial discharge on a Hall thruster presented in Ref. 27, which was shown to give reasonable results for thrusters with long, ceramic chambers [generally known as Stationary Plasma Thruster (SPT)-type thrusters]. The model is stationary, macroscopic, and operates with radially averaged plasma magnitudes. Compared to time-dependent, two-dimensional, particle-based models,[28–30] the characteristics of our model make it fast to run and very suitable for systematic studies on the effects on the thruster response of the different design and operation parameters. In particular, in this paper we analyze in detail the influence of four central parameters of the discharge: the applied discharge voltage, the anode gas flow rate, the axial gradient of the (radial) magnetic field, and the axial length of the chamber. For each parameter, both parametric curves and axial profiles for disparate values of the parameter are presented. Whenever it is possible, the main trends of our simulations are compared with those most commonly observed in experiments. When the numerical and experimental behaviors agree, the main phenomena governing the observed response can be identified and, in some cases, parametric scaling laws can be proposed. When the two trends disagree, we can presume that the dominant physical process is lacking or implemented imperfectly in the model.

Since this paper is, in fact, an application of the work of Ref. 27, the reader is referred to that paper (and a previous one[31]) for the complete description of the principles of operation of a Hall thruster, the theoretical and numerical aspects of the model, and the comparison with related models. Here, Sec. II includes only a very succinct information of the model and the definition of the main variables used throughout the paper. Then, Secs. III–VI treat the influence of each of the four parameters enumerated above. Conclusions are given in Sec. VII. First parametric studies were presented in Ref. 32 and partial results of this work were presented in Refs. 33 and 34.

Section IV includes a section dedicated to the operation at constant electric power. This study is of interest to dual-mode Hall thrusters, which are receiving high attention in new designs for near-future applications.[3] Dual-mode thrusters are needed to carry out satisfactorily, at a nominal electric power, two disparate missions on GEO satellites: orbit top-
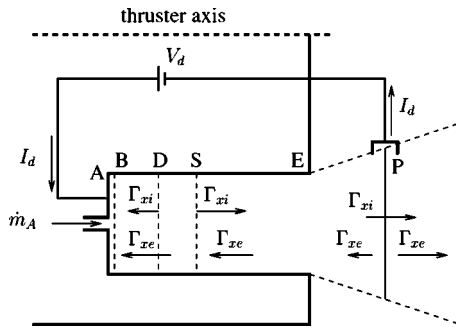
FIG. 1. Sketch of the discharge model. The anode is at point $A$ (with $x_A = 0$); the thruster exhaust at point $E$, and the cathode neutralization surface at point $P$, points $D$ and $S$ correspond to zero and sonic velocities of the ion flow, and are part of the solution. Point $B$ is the anode-sheath transition. Regions $AB$, $BD$, $DS$, $SP$ correspond to electron-repelling sheath, ion-backstreaming region, main ionization layer, and acceleration region. $\Gamma_{x\alpha} = An_\alpha v_{x\alpha}$, $\alpha = i,e,\dots$ are axial flows of particles of each of the plasma species.

ping and stationkeeping, which require high thrust $F$ and high specific impulse $I_{sp}$, respectively. Variable thrust operation has been proposed for drag compensation on low earth orbit (LEO) satellites too.[35]

## II. OVERVIEW OF THE MODEL

### A. Formulation

The model of the plasma discharge we are going to apply here is described in detail in Refs. 27 and 31; a sketch is shown in Fig. 1. The model consists basically of Eqs. (1)–(8) of Ref. 27; we omit to redefine here all the variables and parameters it needs. (There is only a minor change in the model we used here: In order to include the plasma losses to the front walls of the thruster, the terms accounting for particle and energy losses to the thruster walls have been extended to the near plume. The conclusion over this modification are that the energy losses to the external walls are marginal with respect to the total wall-energy losses, but are important to set the point where $T_e$ becomes maximum.)

Each stationary solution of the plasma equations corresponds to a given set of parameters related to the thruster geometry, the wall material, the magnetic field topology, the operational conditions, and the semiempirical models of certain phenomena. The list of such parameters is the following.

(1) The constants defining the ionization and collisional properties of the propellant (xenon, in the cases treated here).

(2) The chamber dimensions: length $L_c$, width $h_c$, and cross-section area $A_c$.

(3) The axial distance of the virtual neutralizer to the chamber exhaust, $L_{cat}$.

(4) The shape of the magnetic field profile. We take $\mathbf{B}(x) = B_r(x)\mathbf{1}_r$, and $B_r(x)$ is approximated by two semi-Gaussian curves of the form

$$B_r(x) = B_{max}\exp\left[-\frac{(x-x_M)^2}{L_b^2}\right], \tag{1}$$

with $B_{max}$ the (maximum) strength of the magnetic field, $L_b = L_{b1}$ for $x < x_M$ and $L_b = L_{b2}$ and for $x > x_M$. Point $M$ is generally placed around the chamber exit.

(5) The discharge voltage $V_d$.

(6) The flow rate and average axial velocity of the gas injected at the anode, $\dot{m}_A$ and $v_{xnA}$, respectively.

(7) The cross-over temperature $T_1$ of the electron fluid for a 100% secondary electron emission yield from the lateral ceramic walls, $\delta_w$. That temperature depends on the wall emission properties and the electron distribution function.[36] Equation (A12) of Ref. 27 [based on Eqs. (12) and (32) of Ref. 37] will be used for $\delta_w(T_e,T_1)$.

(8) The temperature of the electrons emitted by the cathode $T_{eP}$.

(9) The turbulent diffusion parameter $\alpha_{ano}$ defined in Eq. (A23) of Ref. 27, which measures the relative level of correlated electric fluctuations.

(10) The particle recombination factor at the lateral walls $\tilde{\nu}_w$ defined in Eq. (A6) of Ref. 27.

(11) The accommodation factor for the axial velocity of the neutrals recombined at the walls $a_w$ defined in Eq. (13) of Ref. 27.

The integration scheme of the plasma equations does not use all these parameters as input ones. As a consequence we must proceed numerically in two stages. First, an approximate solution is obtained for the set of input parameters required by the integration algorithm. Then, iterative continuation methods (on eight implicit conditions) are used to adjust the solution to the desired values of the above list of parameters.

As previous works, this one considers only stationary solutions of the *normal operation class* described by Russian authors.[8,9,38] The axial structure of the plasma discharge for this class of solutions consists of an electron-repelling anode sheath, an ion-backstreaming region, the main ionization layer, and internal and external acceleration regions. These are regions $AB$, $BD$, $DS$, $DE$ and $EP$, respectively, of Fig. 1, limited by distinguished points $A$ (the anode), $B$ (the sheath transition, characterized by a backward ion sonic flux), $D$ (the ion zero-velocity point), $S$ (the forward ion sonic flux point), $E$ (the chamber exit), and $P$ (the virtual neutralizer/cathode). Solutions without an electron-repelling sheath exist but, according to Ref. 9, they have larger heat depositions at the anode and can result in the discharge easily becoming extinguished.

Reference 27 found that the stationary model reproduces the normal operation class only within the narrow parametric range

$$0.514 \times 10^{-2} < -I_{iA}/I_d < 11.4 \times 10^{-2}, \tag{2}$$

with $I_{iA}$ the ion-backstreaming current reaching the anode and $I_d$ the total discharge current. This thin range for the relative ion back current implies a thin interval of possible values of the magnetic strength $B_{max}$ when the rest of input parameters are fixed. In other words, the *zero-fluctuation* normal operation class exists only within a narrow band of the parametric region $B_{max}(V_d,\dot{m}_A,L_c,\dots)$; see, for instance, Fig. 6 of Ref. 31. The thinness of this band justifies to select an intermediate value of $-I_{iA}/I_d$ to obtain a *single* curve $B_{max}(V_d,\dot{m}_A,L_c,\dots)$ which represents the *whole* band of the

normal operation class. In the computations here we used the value $-I_{iA}/I_d=3.93\times10^{-2}$ (which corresponds to a sheath potential jump of $\phi_{AB}=2T_{eB}/e$).

Finally, Ref. 27 suggests that the resulting curve for $B_{\max}(V_d,\dot{m}_A,L_c,...)$ corresponds to the optimum operational value of the magnetic strength determined experimentally. The practical experience with Hall thrusters shows that, for optimum operation, it is convenient to adjust the magnetic strength for each operational case and the optimum $B_{\max}$ corresponds generally to minimum values of the discharge current or the level of current oscillations. Although the present stationary model has no means to confirm it, Ref. 27 argued that the characteristics of the solutions of the normal operation class (such as its axial structure, zero fluctuations, and the behavior of $B_{\max}$ versus $V_d$) support its suggestion.

## B. Partial efficiencies

There is not in the literature a universal definition and nomenclature for the partial efficiencies characterizing the Hall thruster discharge. In addition, some modifications with respect to the nomenclature used in Ref. 27 have been found convenient to do here.

The (thrust) efficiency (based in the anode gas flow rate) is defined as

$$\eta=F^2/2\dot{m}_A P_d, \quad F\simeq\sum_{\alpha=i,n}\dot{m}_{\alpha\infty}v_{x\alpha\infty}, \tag{3}$$

and is simple to measure experimentally. Partial efficiencies of interest are the propellant utilization (or ionization efficiency), $\eta_u=\dot{m}_{i\infty}/\dot{m}_A$, the current utilization, $\eta_{cur}=I_{i\infty}/I_d$, and the voltage utilization, $\eta_{vol}=m_iv_{xi\infty}^2/2eV_d$, ($v_{xi}$, $\dot{m}_i$, and $I_i$ are ion axial velocity, flow, and electrical current, respectively; subscript $\infty$ refers to downstream conditions, which here are computed at the neutralization surface). The ratio $i_d=\eta_u/\eta_{cur}=m_iI_d/e\dot{m}_A$ is the dimensionless discharge current (or current parameters).

In addition, we define the propulsive efficiency as

$$\eta_{prop}=P_{use}/P_d, \quad P_{use}=\sum_{\alpha=i,n}\dot{m}_{\alpha\infty}v_{x\alpha\infty}^2/2, \tag{4}$$

with $P_{use}$ the useful power. The main contribution to $\eta_{prop}$ comes from the ion beam and satisfies

$$\dot{m}_{i\infty}v_{xi\infty}^2/2P_d=\eta_{cur}\eta_{vol}. \tag{5}$$

When the ionization is not total, the plasma discharge ejected by the thruster is constituted of two species with different velocities, and $\eta_{prop}$ and $\eta$ do not coincide. One has

$$\eta_{prop}-\eta=(1-\eta_u)\times\dot{m}_{i\infty}(v_{xi}-v_{xn})_\infty^2/2P_d. \tag{6}$$

Finally, it is useful to split the power losses as[27]

$$P_{loss}\equiv P_d-P_{use}=P_{ion}+P_{wall}+P_{anode}+P_{plu}, \tag{7}$$

where the four contributions correspond to ionization, heat deposition at the lateral walls and the anode, and losses within the plume region (this last contribution is not totally meaningful since the complete plume is not simulated).

## C. Scaling laws

The thickness of the anode sheath $L_{AB}$ is negligible in the chamber scale. Thus, the lengths of the three quasineutral regions of the discharge satisfy

$$L_{BD}+L_{DS}+L_{SP}=L_{AP}. \tag{8}$$

Scaling laws for the lengths of these three regions can be obtained from approximate analyses of the plasma equations in each region.[27,31,39,40]

The acceleration region is characterized by negligible net plasma production, supersonic ion motion, large electric fields, and a voltage drop taking most of the discharge voltage. Thus, approximate equations of the discharge in that region are

$$I_i(x)\simeq\text{const}=I_{iP},$$

$$-v_{xe}=v_{xi}(I_d-I_{iP})/I_{iP},$$

$$ed\phi/dx=m_ev_{xe}\omega_e^2/\nu_e,$$

$$-ed\phi/dx=m_iv_{xi}dv_{xi}/dx. \tag{9}$$

Operating with these equations and integrating for $v_{xi}$, one has

$$v_{xiP}-v_{xiS}=(I_d/I_{iP}-1)\int_S^P\bar{\nu}_ddx, \tag{10}$$

where $\bar{\nu}_d=m_e\omega_e^2/\nu_em_i$ represents the (normalized) axial diffusion frequency for electrons. When turbulent diffusion dominates over the rest of collisional effects, one has $\bar{\nu}_d\propto B(x)$. Substituting $v_{xi}$ in terms of $\phi$ and imposing that the voltage drop across the acceleration region is close to $V_d$, Eq. (10) yields

$$\sqrt{2eV_d/m_i}\simeq(\eta_{cur}^{-1}-1)\{\bar{\nu}_d\}_{SP}L_{SP}, \tag{11}$$

where $\{\}$ means an average value for the respective magnitude in region $SP$. Numerical results corroborate that the relative errors of this scaling law are below a 20%.[33]

The ion-backstreaming region is governed mainly by the electron dynamics, which are driven towards the anode by a large pressure gradient, whereas the electric field is negligible (except at the transition to the anode sheath). Reference 39 demonstrated that in order to determine the transition to the ionization region (and thus the length of the ion-backstreaming region, $L_{BD}$) small ionization effects must be taken into account. The approximate analytical solution of Ref. 39 for region $BD$ is basically applicable to the present model and yields

$$L_{BD}\propto\{T_e^{3/2}\bar{\nu}_d^{-1/2}\nu_i^{-1/2}\}_{BD}, \tag{12}$$

with $\nu_i=n_nR_i(T_e)$ the ionization frequency. In the ion-backstreaming region, $T_e$ is smaller than the ionization potential $E_i$ and the ionization rate depends exponentially on $T_e$,

$$R_i(T_e)\propto T_e^{1/2}\exp(-E_i/T_e), \tag{13}$$

which makes $L_{BD}$ very sensitive to the electron temperature in the region.
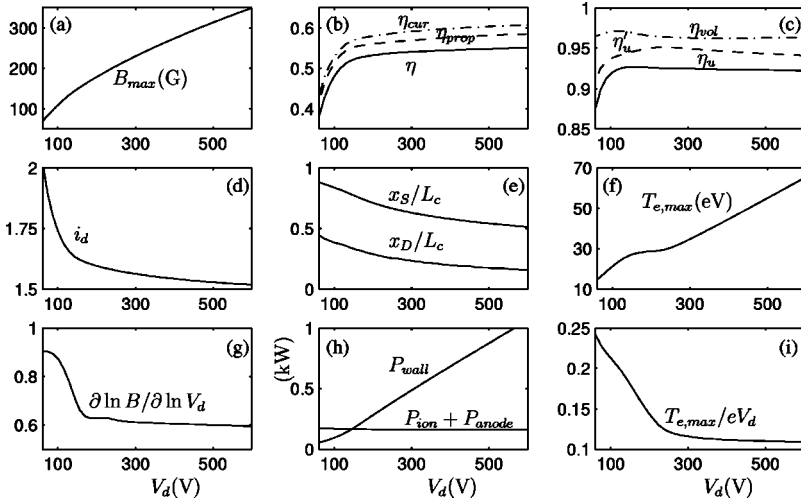
FIG. 2. Evolution of thruster performances with the discharge voltage. Geometrical and operating parameters are $L_c = 25$ mm, $A_c = 40.06$ mm$^2$, $h_c = 15$ mm, $L_{b1} = 15$ mm, $L_{b2} = 5$ mm, $x_M = x_E$, $T_1 = 30$ eV, $\dot{m}_A = 4.75$ mg/s. Other parameters of the model are $\alpha_{ano} = 9.45 \times 10^{-3}$, $\tilde{\nu}_w = 0.17$, $a_w = 0.85$. Plot (g) represents the slope of the curve $B_{max}(V_d)$ of plot (a). Plot (i) represents the ratio $T_{e,max}/eV_d$ of the curve of plot (f). In plot (h), the ratio $P_{anode}/P_{ion}$ is about 1/4. Partial efficiencies are defined in Sec. II B.

Finally, a simple dimensional analysis of the ionization region suggests that its length satisfies[39]

$$L_{DS} \sim \nu_{iS}^{-1} \sqrt{T_{eS}/m_i}. \tag{14}$$

This law is useful in this form since the temperature at the forward sonic point $T_{eS}$ is found to remain rather invariable (around 20 eV) for all the parametric conditions considered in the paper.

## III. INFLUENCE OF THE DISCHARGE VOLTAGE

Figures 2(a)–2(i) show the evolution of the main thruster parameters when the discharge voltage is varied over a large range. Geometrical and operation parameters are listed in the figure caption; they correspond to typical ones for an SPT-100 thruster and were used already in Ref. 27. Figures 3(a)–3(d) compare the axial profiles of the plasma magnitudes for two disparate values of $V_d$.
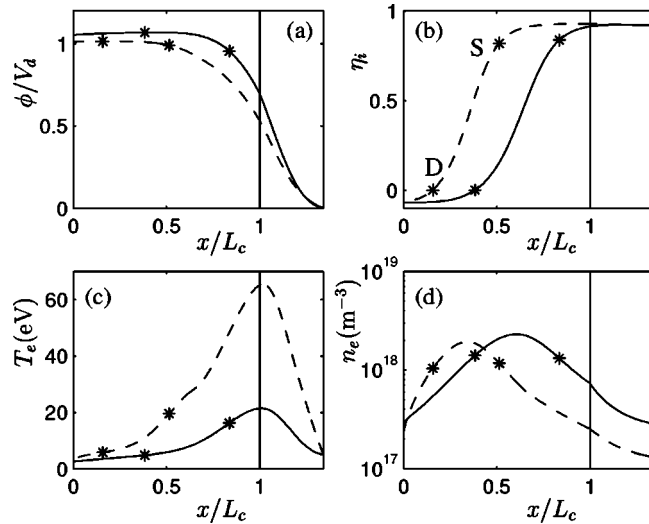


FIG. 3. Axial profiles of the discharge for two particular parametric cases of Fig. 2: $V_d = 100$ V (solid lines) and 600 V (dashed lines). In each curve, asterisks represent points $D$ (left) and $S$ (right). The chamber exit is at the intermediate vertical line, $x/L_c = 1$, and the cathode/neutralizer is placed at the right boundary of the plots.

Figure 2(a) shows the adjustment required by the magnetic field strength $B_{max}$ for optimum operation of the thruster as $V_d$ is changed. The necessity of scaling $B_{max}$ with $V_d$ is well known experimentally,[8] but there is some controversy on the value of the scaling rate $p = \partial \ln B_{max}/\partial \ln V_d$ (i.e., the exponent of the potential law $B_{max} \propto V_d^p$). The value proposed commonly is[8,19] $p \sim 0.5$, but other experiments suggest[16,41] $p \sim 1$ or even[21] $p \sim 1.2–1.5$. Figure 2(g) shows that $p(V_d)$ is not constant with the discharge voltage. For high voltages, $p$ tends to approach 0.5, whereas one has $p \sim 1$ for low voltages. The numerical simulations of Ref. 42 for a thruster with metallic walls propose $p \sim 1$, and those of Ref. 31 with zero wall losses model yield $p = 5/4$. Taking into account that, in our model, energy losses at the walls dominate except for low voltages, Fig. 2(h), the conclusion seems to be that one has $p \sim 0.5$ when wall-energy losses are relevant, and $p \sim 1$ otherwise.

Figure 2(d) plots the variation of the current parameter $i_d = m_i I_d/e\dot{m}_A$; the discharge current (in amperes) satisfies $I_d \simeq 0.731 \times i_d \dot{m}_A$, when $\dot{m}_A$ is given in mg/s. The experimental evidence on $I_d(V_d)$ is that: (a) at high voltages, $\partial I_d/\partial V_d$ is weakly positive; (b) at moderate voltages ($V_d \sim 200–400$ V, say), $\partial I_d/\partial V_d$ is small, but different experiments show different signs; and (c) at low voltages $I_d(V_d)$ presents a peak and then drops sharply as $V_d$ decreases. At moderate voltages, Refs. 20, 22 (for BNSiO$_2$), and 23 (for the SPT-140) report $\partial I_d/\partial V_d$ negative, Refs. 19, 23 (for the SPT-115), and 24 find positive that derivative, and Refs. 13 and 16 measure an intermediate minimum of $I_d$ in that voltage range. Our simulations yield a small negative slope of $I_d(V_d)$ over the whole voltage interval, which is the consequence of the positive slope for the propulsive efficiency, $\eta_{prop}(V_d)$, Fig. 2(b).

It is known experimentally that the operation at low voltages is highly oscillatory,[20,22] which would explain that our stationary model is unable to recover the sharp decrease of $I_d(V_d)$ at low voltages. In addition, our solutions for very low voltages require to decrease continuously $B_{max}$, while experiments could have kept $B_{max}$ too high, which is known to make the discharge unstable.[8,22] A large increase of $I_d$ for

J. Appl. Phys., Vol. 96, No. 2, 15 July 2004

E. Ahedo and D. Escobar    987

low values of $B_{\max}$, similar to ours at low $V_d$, is reported in Fig. 4(b) of Ref. 43.

The different partial efficiencies are plotted in Figs. 2(b) and 2(c). A high- and a low-efficiency regimes are observed. The high-efficiency regime corresponds to $V_d > 200$ V, roughly, and thus covers the nominal and high voltage ranges. This is the main regime of operation, when the thruster works at maximum (and almost constant) efficiency, and both thrust $F$ and specific impulse $I_{sp}$ increase as $\propto V_d^{1/2}$. Since the variation of $I_d$ with $V_d$ is weak in this regime, the discharge power $P_d = V_d I_d$ scales practically as $\propto V_d$ and the thrust-to-power ratio follows $F/P_d \propto V_d^{-1/2}$.

Figure 2(h) plots the main contributions to the energy losses $P_{loss}$, Eq. (7). We observe that $P_{wall} \propto P_d$ whereas $P_{ion} + P_{anode} \sim$ const. In the high-efficiency regime, heat deposition at the lateral walls are the main contribution to $P_{loss}$ and their evolution with $V_d$ makes the propulsive efficiency, $\eta_{prop}$ [Fig. 2(b)], almost constant. Gas ionization is very efficient in this regime and the propellant utilization, $\eta_u$ [Fig. 2(c)], is around its maximum value; this value is determined from the balance in the acceleration region between particle recombination at the walls and residual volume ionization.[27] In general, we find that the different efficiencies satisfy

$$\eta_{prop} \simeq \eta_{cur} \eta_{vol} \sim \eta_{cur}, \quad \eta \simeq \eta_u \eta_{prop}. \tag{15}$$

The ratio $\eta/\eta_{prop} \equiv \eta_u'$, an alternative measure of the propellant utilization, is plotted in Fig. 2(c).

Although not shown on Fig. 2, the parametric investigation on $V_d$ was continued up to 800 V. The results suggest that the efficiency $\eta(V_d)$ approaches asymptotically a maximum value (which is the product of the maxima of $\eta_{prop}$ and $\eta_u$). A monotonic evolution of $\eta(V_d)$ is found experimentally in Fig. 7 of Ref. 24, and in some of the curves of Fig. 6 of Ref. 23. However, most experimental data show a peak of the thrust efficiency for a moderate-to-high value of $V_d$ (in the interval 500–800 V typically).[13,16,19,23] This peak could be due to multiple ionization (which is not included in our model) or to phenomena, such as plasma-wall interaction or turbulent diffusion, which are still modeled imperfectly. The presence or lack of local extreme of $\eta(V_d)$ and $I_d(V_d)$ [Fig. 2(d)] at high voltages have likely the same cause.

Thruster performances deteriorate as $V_d$ enters into the low-efficiency regime ($V_d < 200$ V). The efficiency decreases quickly due to the added decrements of $\eta_{prop}$ and $\eta_u$. As $V_d$ is reduced,

(a) $P_{ion} + P_{anode}$ starts to dominate over $P_{wall}$, Fig. 2(h); since $P_{ion} + P_{anode}$ is almost independent of $V_d$, the propulsive efficiency decreases.

(b) The maximum plasma temperature $T_{e,\max}$, Fig. 2(f), and the ionization frequency $\nu_i$ decrease. This enlarges the effective ionization region and reduces the final propellant utilization, $\eta_u$.

The parametric investigation of Fig. 2 was continued down until $V_d \sim 20$ V, to corroborate that no physical limit changing the qualitative behavior of the discharge is reached yet. For a stationary operation at this extremely low voltage, $B_{\max}$ must be reduced to 23.3 G and $I_d$ increases up to 14.1 A. This implies that the current utilization $\eta_{cur}$ is very low

and, although the propellant utilization is still moderate ($\sim 65\%$), the thrust efficiency drops to a 14%. At $V_d \sim 20$ V, wall losses account only for a 10% of the total energy losses.

Figure 2(e) plots the evolution of the positions of the boundaries $D$ and $S$ of the main ionization region with $V_d$. That plot is complemented with Fig. 3(b) for the local ion flux fraction,

$$\eta_i(x) = \dot{m}_i(x)/\dot{m}_A; \tag{16}$$

notice that $\eta_i$ is negative to the left of point $D$. As $V_d$ increases, $\nu_i$ increases and the ionization region becomes shorter. The acceleration region moves slightly upstream and this reduces the axial electric field there, Fig. 3(a); this behavior agrees with the experimental observations of Ref. 24. Figure 3(b) shows that the division of the internal plasma structure on three quasineutral regions and the confinement of the effective ionization layer to region $DS$ is more correct at high voltages. For low voltages, the ionization of the gas extends to the whole discharge chamber (with maximum plasma production in region $DS$).

Further understanding on the interaction among the different processes and parameters is obtained from the scaling laws proposed in Sec. II. From Eq. (11), $B_{\max}(V_d)$ satisfies

$$B_{\max} \propto \frac{V_d^{1/2}}{L_{SP}} \frac{\eta_{cur}}{1 - \eta_{cur}} \sim \frac{V_d^{1/2}}{L_{SP}} \frac{P_{use}}{P_{loss}}. \tag{17}$$

The classical result of $B_{\max} \propto V_d^{1/2}$ is obtained when $L_{SP}(V_d)$ and $\eta_{cur}(V_d)$ are assumed constant.[8] This tends to be true in the high voltage range, because of $P_{loss}/P_d \sim$ const and the small margin of variation of $L_{SP}$. However, both $L_{SP}$ and $\eta_{cur}$ decrease as the discharge voltage is reduced. For low enough voltages, Eq. (17) becomes $B_{\max} \propto V_d^{1/2} L_{SP}^{-1} P_{use}$, and the product of the two last factors vary as $\sim V_d^{1/2}$ (or as $\sim V_d^{3/4}$ for zero-wall losses[31]).

As $V_d$ increases, the effective diffusion frequency, $\bar{\nu}_d$ in Eq. (10), increases and this explains the increment of $L_{BD}$ [Eq. (12) and Fig. 2(e)]. The effect of $V_d$ on $L_{DS}$ [Eq. (14) and Fig. 2(e)] is very small and is due to the weak variation of $\{T_e\}_{DS}$ with $V_d$ [Fig. 3(c)].

Figure 2(f) plots the evolution of the maximum plasma temperature $T_{e,\max}(V_d)$. Three different slopes are observed, which correspond to different regimes for the temperature profile: A nonsaturation regime at low $V_d$ ($V_d < 150$ V) with mild temperature gradients and energy losses at the walls; a saturation regime at moderate voltages $V_d$ (150 V $< V_d <$ 250 V), when space-charge saturation of the lateral sheaths near the chamber exit limits $T_{e,\max}$ to $T_1$ (=30 eV) approximately; and an over-saturation regime at high $V_d$ (250 V $< V_d$), when ohm heating is strong enough to heat the plasma above the temperature for charge saturation. The profiles of $T_e(x)$ in Fig. 3(c) correspond to the two extreme regimes.

The $V_d$ interval for each of these three regimes depends on the temperature $T_1$ characterizing the secondary electron emission yield of the walls.[33] Reference 26 reproduces experimentally the two first regimes of our curve $T_{e,\max}(V_d)$. The saturation temperature is higher than ours (50 eV instead of 30 eV), which shifts the saturation regime to larger volt-
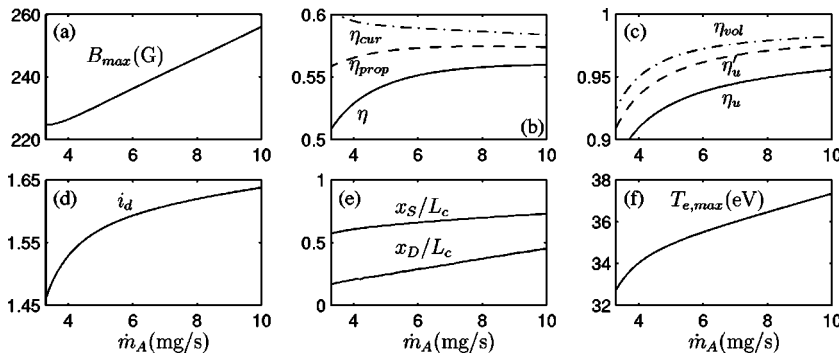
FIG. 4. Evolution of thruster performances with the gas flow rate. The discharge voltage is 300 V and the rest of geometrical and operating parameters are as in Fig. 2.

ages ($V_d > 500$ V) and would explain why the oversaturation regime is not reached in the experiments (which cover only the interval 200–600 V).

The energy balance of the axial discharge is too complex to obtain simple scaling laws for the temperature behavior, so numerical fits for the ratio $T_{e,\max}/eV_d$, Fig. 2(i), are useful. Reference 26 finds $T_{e,\max}/eV_d \sim 0.13$ for the low temperature regime. Our simulations yield $T_{e,\max}/eV_d \sim 0.15$–$0.20$ for the same regime, and $T_{e,\max}/eV_d \sim 0.11$ for the high temperature regime. The agreement with Ref. 26 is considered very promising if we take into account that several facts suggest that the model for the electron energy balance needs to be improved yet. [On the one hand, Ref. 27 had to introduce a reduction factor to avoid overestimation of particle and energy losses at the lateral walls; on the other hand, in all the plots of $T_e(x)$ shown in this paper the maximum electron temperature tends to be close to the chamber exit, whereas, in many experiments[26,44] this maximum is found inside the chamber, near the end of the ionization layer.]

## IV. INFLUENCE OF THE GAS FLOW RATE

This is the second main parameter governing the operation of the thruster. In this section we analyze the effects of modifying it while keeping $V_d$ constant. The main trends observed experimentally are the following. As the gas flow rate is incremented: (a) the magnetic field must be augmented in order to keep a good thruster operation;[19] (b) the propellant utilization and the thrust efficiency increase;[13,19,24] (c) the specific impulse increases slightly;[13,19] and (d) the acceleration layer drifts downstream.[14,17] As it happens with other parameters, the above tendencies are not universal; for instance, Ref. 16 does not find a monotonic trend for $\eta(\dot{m}_A)$.

Figures 4(a)–4(f) show the evolution of the main discharge parameters with the gas flow rate and Figs. 5(a)–5(d) plot axial profiles for two extreme values of $\dot{m}_A$. The simulation results agree totally with the experimental trends reported in the previous paragraph. Two main conclusions are extracted: (a) the discharge is more efficient at high gas flow rates; and (b) relative changes on the discharge magnitudes are larger at low flow rates.

A more detailed analysis of the discharge response to increments of $\dot{m}_A$ shows the following. First, the neutral density and the ionization frequency increase. This reduces the length of the ionization region [Eq. (14) and Fig. 4(e)], defines more clearly the boundaries of that region [Fig. 5(b)],

and increases $\eta_u$ [Fig. 4(c)]; also, a shorter ionization region implies a larger voltage utilization, $\eta_{vol}$. Second, a more efficient ionization implies lower temperatures on the ion-backstreaming region [Fig. 5(c)], which increases its length, $L_{BD}$ [Eq. (12) and Fig. 4(e)]. Third, $L_{BD}+L_{DS}$ increases, which makes the acceleration region shorter [Fig. 4(e)]. Four, the decrease of $L_{SP}$ is the main responsible of the moderate adjustment of $B_{\max}(\dot{m}_A)$, [Eq. (11) and Fig. 4(a)]. Five, a shorter acceleration region leads to lower wall losses and a higher $\eta_{prop}$ [Fig. 4(b)]. Six, the current utilization and the discharge current follow $\eta_{cur} \simeq \eta_{prop}/\eta_{vol}$ and $i_d = \eta_u/\eta_{cur}$; notice in Fig. 4(b) that the thrust efficiency decreases when the current utilization increases. And seven, Fig. 5(c) shows that the displacement of the ionization region towards the chamber exit leads to steeper profiles of $T_e(x)$.

Finally, stationary solutions become difficult to obtain for low flow rates. Indeed these solutions seem to fail to exist beyond a minimum value of $\dot{m}_A$.[34] Since similar losses of stationary solutions exist with two other parametric continuations, the discussion of this subject is postponed to Sec. VI A.

### Operation at constant power

In order to keep $P_d = $ const, the discharge voltage needs to be varied in the opposite direction to the gas flow rate. Whereas the two cases discussed before showed the indi-
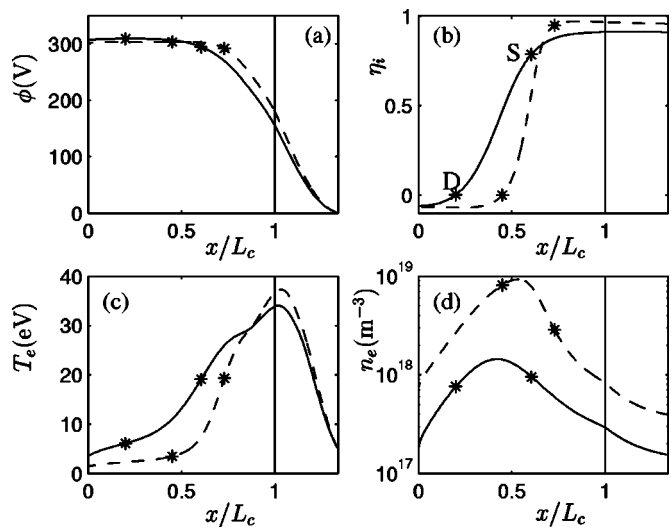


FIG. 5. Axial profiles of the discharge for two particular parametric cases of Fig. 4: $\dot{m}_A = 4$ mg/s (solid lines) and 10 mg/s (dashed lines).
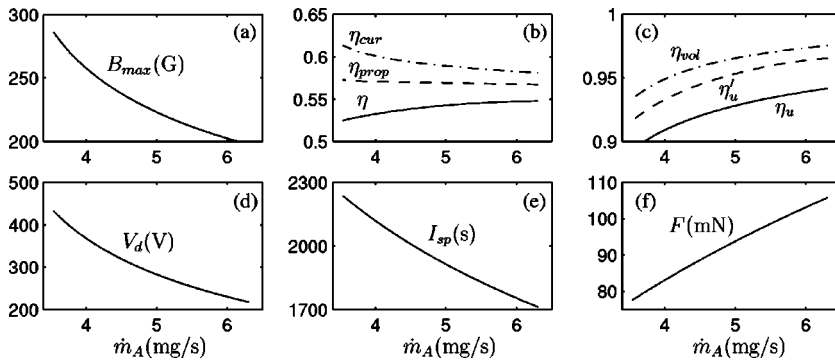
FIG. 6. Evolution of thruster performances with the gas flow rate and discharge voltage, keeping the discharge power constant at 1620 W. Rest of geometrical and operating parameters as in Fig. 2.

vidual effects of $V_d$ and $\dot{m}_A$ on the discharge, the present case allows us to compare the performances of the thruster when this is operated on the high-thrust (low $V_d$ and high $\dot{m}_A$) and the high-$I_{sp}$ (high $V_d$ and low $\dot{m}_A$) modes.

Figures 6(a)–6(f) show the evolution of the main discharge parameters in terms of the variation of $\dot{m}_A$. The corresponding variation of $V_d$ is plotted in Fig. 6(d) and the main output parameters: thrust efficiency, specific impulse, and thrust, are plotted in Figs. 6(b), 6(e), and 5(f). The evolution of the different parameters depends on whether the influence of $\dot{m}_A$ or $V_d$ is dominant. For instance, the adjustment of the magnetic field strength [Fig. 6(a)] is affected mainly by the variation of $V_d$, in agreement with Ref. 35, whereas $\eta_u$ and $\eta_{vol}$ [Fig. 6(c)] depend mainly on the changes of $\dot{m}_A$. The situation is more predictable for other parameters, such as the position of the acceleration region, which is known to move downstream when $\dot{m}_A$ increases of $V_d$ decreases [Figs. 2(e) and 4(e)].

Since heat deposition at the walls dominate the energy losses and scales as $\propto P_d$, the propulsive efficiency [Fig. 6(b)] remains practically constant. From $i_d \simeq \eta_u \eta_{vol} / \eta_{prop}$, it turns out that $i_d$ increases (mildly) with $\dot{m}_A$. The discharge voltage follows $V_d = P_d / i_d \dot{m}_A$ and is proportional to $\dot{m}_A^{-1}$, as a first approximation. The thrust and the specific impulse follow $F = I_{sp} \dot{m}_A \simeq (\eta_u \eta_{prop} \times 2 \dot{m}_A P_d)^{1/2}$; thus, one has $F \propto V_d^{-1/2}$ and $I_{sp} \propto V_d^{1/2}$, approximately. The main conclusion of this parametric study is that the thruster operates more efficiently at high mass flows (i.e., on the high-thrust mode) [Fig. 6(b)] which agrees with the experimental observations of Refs. 35 (for $V_d > 200$ V) and 24. In our model the increase of $\eta$ is due to a higher propellant utilization and not to lower wall energy losses, as suggested by Ref. 35. This ex-

planation would be consistent with the decrease of $\eta$ observed in this last paper for low discharge voltages ($V_d \sim 100$ V).

## V. INFLUENCE OF THE AXIAL GRADIENT OF THE MAGNETIC FIELD

It is universally recognized the importance of shaping correctly the magnetic field for a good performance of a Hall thruster.[9,10,45] The optimization of the magnetic field topology in the discharge chamber is a task of primordial importance in new designs. The magnetic field in the chamber is mainly radial and there is a general accord that a steep axial profile for $B_r(x)$ with the maximum field placed near the chamber exit is desirable. The reasons in favor of it would be:[8–10,45] (a) the magnetic field lines tend to focus the ions away from the walls, thus reducing wall losses; (b) the ion flow is more stable to fluctuations of the electrostatic potential; and (c) the thrust efficiency is found to be higher. This last point is the one we are going to analyze here; notice that the two first ones cannot be studied with the present model. Although point (c) is partially related to point (b), as Ref. 9 suggests, there is direct experimental evidence that the change of the magnetic field gradient modifies the structure of the discharge and, therefore, the thruster performances. In particular, it has been observed that, as the magnetic profiled becomes more pronounced, (a) the acceleration layer moves downstream[14] and (b) the discharge current decreases and the efficiency increases.[14,46] A partial exception to this last observation is provided by Ref. 11, which reports a maximum of efficiency for a rather pronounced magnetic shape.
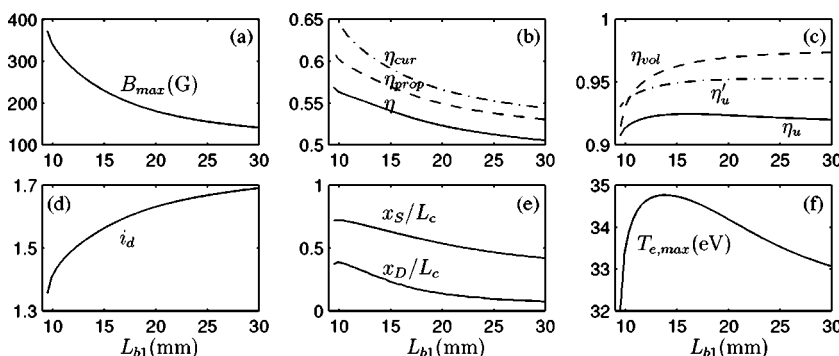


FIG. 7. Evolution of thruster performances with the characteristic internal length of the magnetic field strength, defined in Eq. (1). The discharge voltage is 300 V and the rest of geometrical and operating parameters are as in Fig. 2.
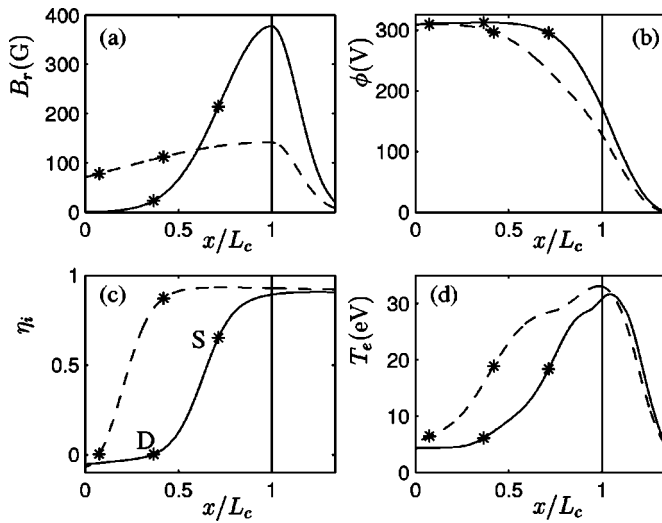
FIG. 8. Axial profiles of the discharge for two particular points of Fig. 7: $L_{b1} = 9.49$ mm (solid lines) and 30 mm (dashed lines).

Equation (1) defines the magnetic field shape we used in our simulations. The characteristic axial length of the internal profile is measured by the length $L_{b1}$. Figures 7(a)–7(f) plot the parametric continuation for $L_{b1}$; notice that the peak of the magnetic field is fixed at the chamber exit and the external shape is not modified ($L_{b2} = $const). Figures 8(a)–8(d) shows the plasma profiles for two disparate magnetic shapes: in the solid-lines case, the magnetic field is very small near the anode, whereas in the dashed-lines case, it is near uniform along the chamber.

The main features we observe as $L_{b1}$ is increased (and the magnetic field becomes more flat) are the following. First, $B_{max}(L_{b1})$ [Figs. 7(a) and 8(a)] decreases. The simulations yield $B_{max} \propto L_{b1}^{-1}$ with a relative error of an 8%. This behavior is justified by the scaling laws (11) and (12) and agrees with the idea that the magnetic integral, $\int B_r(x)dx$, is a relevant parameter on the discharge response.[45] Second, the increase of $B_r(x)$ near the anode reduces the ion-backstreaming region [Figs. 7(e) and 8(c)]; then, since $L_{DS}$ is weakly affected, the acceleration region moves upstream (as the experiments confirm). Third, wall-energy losses increase with $L_{SP}$ and the propulsive efficiency decreases [Fig. 7(b)]. Four, since the propellant utilization is affected weakly by $L_{b1}$,[27] the thrust efficiency decreases too.

Although $T_{e,max}(L_{b1})$ does not change much [Fig. 7(f)], the temperature profile [Fig. 8(d)] is affected by the position

of the acceleration region and the complex energy balance. In particular, observe the small plateaus around the saturation value (30 eV) of the plasma temperature; they are due to the approximate balance between the ohm heating and the wall cooling of the plasma. Similar plateaus are found in the profiles of $T_e$ of the rest of the cases.

No numerical solution is found for a characteristic length below $L_{b1} \simeq 9.5$ mm, the solid-line case of Fig. 8. A turning point on the parametric curves of Fig. 7 is detected there. We tried to continue the parametric curves into a second branch, with $L_{b1}$ increasing again, but the continuation algorithms did not converge.

## VI. INFLUENCE OF THE CHAMBER LENGTH

The optimization of the channel length $L_c$ is an important aspect of the Hall thruster design. However, detailed data on the effect of modifying $L_c$ is scarce. In Ref. 12 it is found experimentally that the current utilization and the efficiency decrease as the chamber length is increased. In addition, it is argued (but not verified experimentally) that the propellant utilization $\eta_u$ must increase with $L_c$ increasing, and it is concluded that the maximum efficiency must be obtained for an intermediate value of the chamber length. The effects of modifying the chamber length are analyzed experimentally in Ref. 13 too. It is found that (for each $\dot{m}_A$) there is an optimum $L_c$ that maximizes the propellant utilization and, as a result, the efficiency.

Figures 9(a)–9(f) depict our parametric results when $L_c$ is modified. In order to separate the influence of $L_c$ from that of the internal shape of the magnetic field, we keep $L_{b1}/L_c$ = const; however, external lengths, such as the magnetic gradient length, $L_{b2}$, and the distance to the neutralizer, $L_{cat}$, were not scaled with $L_c$. The axial profiles for cases $L_c$ = 17 mm and 42.5 mm are plotted in Figs. 10(a)–10(d); the use of a dimensionless abscissa, $x/L_c$, allows us a more comprehensive comparison of these disparate cases.

The adjustment of $B_{max}(L_c)$ follows $B_{max} \propto L_c^{-1}$ (with a relative error of a 3%), due to the same reasons than in the continuation on $L_{b1}$ (notice that $L_{b1}/L_c$ is constant here). For short chambers, the ionization efficiency (and the voltage utilization) increase with $L_c$ [Figs. 9(c) and 10(b)]; for long enough chambers, $\eta_u$ becomes practically independent of $L_c$.[27] An interesting (and no obvious) result related to the discharge response is that the acceleration region does not move towards the chamber exhaust, as $L_c$ is reduced; indeed,
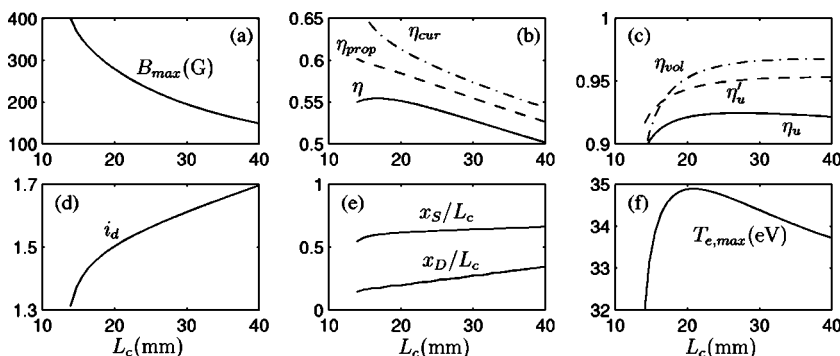


FIG. 9. Evolution of thruster performances with the channel length, keeping the ratio $L_{b1}/L_c$ constant at 0.6. The discharge voltage is 300 V and the rest of geometrical and operating parameters are as in Fig. 2.
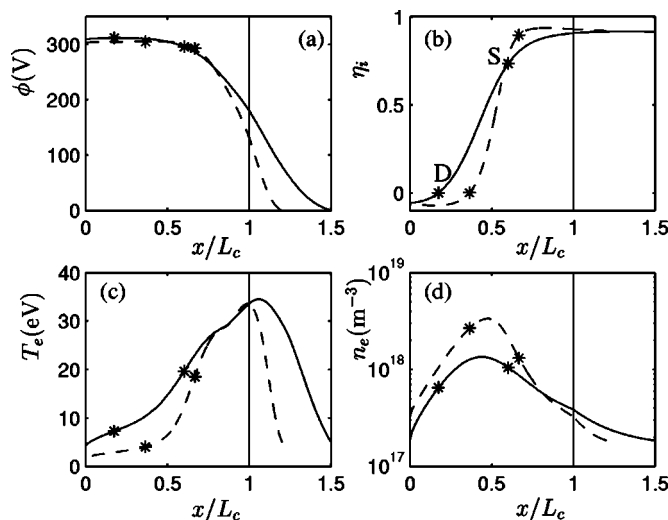
FIG. 10. Axial profiles of the discharge for two particular points of Fig. 9: $L_c = 17$ mm (solid lines) and 42.5 mm (dashed lines).

$L_{SP}/L_c$ increases weakly [Fig. 9(e)] and this behavior is justified by Eq. (11). This last fact and the shorter ionization layer explains that $L_{BD}$ takes most of the change of $L_c$. The increase of $L_{SP}$ with $L_c$ augments the wall-energy losses and reduces the propulsive efficiency [Fig. 9(b)]. Finally, the experimental evidence is confirmed; $\eta$ is maximum for an intermediate chamber length ($L_c = 16.5$ mm in our simulations) and this optimum length comes out from the trade-off between the opposite behaviors of $\eta_{prop}(L_c)$ and $\eta_u(L_c)$.

**Loss of stationary solutions**

The parametric continuations on $L_c$ stop to yield valid solutions for $L_c$ below 13.7 mm, approximately. Therefore, the four parametric studies we have carried out show that our stationary model do not yield solutions when (i) the mass flow rate is too low, (ii) the magnetic field inside the chamber is too pronounced (i.e., too low in the anode region), and (iii) the chamber length is too short. We are not sure on whether the exact cause of these behaviors is physical or numerical. There are three significant coincidences in the respective limit cases for each parameter: (i) the dimensionless current, $i_d$, reaches a minimum value of around 1.3, (ii) the ionization is not very efficient and tends to occupy most of the channel, and (iii) the maximum plasma temperature approaches the saturation value. There are relevant differences too, such as (i) the length of the ion-backstreaming region is large for the case of $L_{b1}$, but it is small in the two other cases, and (ii) the efficiency behaves differently for the three limit cases. The coincidences on a minimum value of $i_d$ and a deficient ionization suggest a physical reason for the loss of solutions. Our solution class (stationary and with a high propellant utilization) becomes increasingly difficult to sustain as $i_d$ approaches one. Thus, the loss of solutions could be related to a sharp transition to another operational regime, either oscillatory or with a low efficiency. (In the first version of the present axial model,[39] which considered neither heat conduction nor lateral wall losses, a stationary, low-efficiency regime was clearly determined, with no continuous transition, apparently, to the high-efficiency regime.) The

coincidences on the behavior of $T_{e,max}$ can be due to either physical or numerical reasons. When $T_{e,max}$ crosses the saturation value, $T_1$, the energy balance is strongly modified by the sharp change on the value of $P_{wall}$.[27] On the numerical side, the continuation routines have difficulties in crossing these parametric regions and could be nonconvergent. On the physical side, it could happen that a stationary energy equilibrium could not be sustained longer. In conclusion, further work is needed to clarify the discharge response around the limit cases of the parametric continuations.

## VII. CONCLUSIONS

A recent stationary, macroscopic model of the discharge in a Hall thruster is found to be very suitable to investigate the influence of four central parameters on the discharge response. Many of the principal trends observed experimentally have been reproduced and physically understood. Scaling laws of interest have been proposed and checked.

The main conclusions that have been reached are the following.

(1) The thrust efficiency is mainly the product of the ionization and propulsive efficiencies. The propulsive efficiency measures the relative useful power, is lower than the ionization efficiency, and should be the main focus of design optimization. A high propulsive efficiency is favored by (moderately) large discharge voltages, large magnetic field gradients, and short chamber lengths. A high propellant utilization is favored mainly by high enough mass flows and chamber lengths. In particular, these behaviors explain that there is an optimum length chamber that maximizes the thrust efficiency.

(2) The operation of dual-mode thrusters at constant power has shown a larger efficiency in the high-thrust mode, but differences with the high-$I_{sp}$ mode are not very large, thanks to the opposite trends of the propulsive and ionization efficiencies.

(3) The optimum adjustment law for $B_{max} \propto V_d^p$ yields $p \sim 0.5$ when wall-energy losses dominate and $p \sim 1$ otherwise. This law comes out mainly from the characteristics of the acceleration region. The adjustment for $B_{max}(L_c)$ is mainly based on the preservation of the magnetic integral (i.e., the global electron axial diffusion). The adjustment required for $B_{max}(\dot{m}_A)$ is small.

(4) As a general rule, the position and extension of the three quasineutral regions of the discharge are largely affected by the four parameters we have studied.

(5) Stationary solutions at low discharge voltages require low magnetic fields and very high discharge currents, which penalizes strongly the propulsive efficiency.

(6) Stationary solutions are lost for small mass flows, small chamber lengths, and large magnetic axial gradients. The reasons for it are not totally clear yet. They seem related to difficulties on attaining high ionization and keeping a stationary energy balance.

The good results obtained with these parametric studies confirm the model as a useful tool to carry out quick predesign studies of Hall thruster chambers. This does not exclude (but makes more necessary) to improve its weakest points,

related to phenomena that are not fully understood yet. Reference 27 identifies (i) the role and level of turbulent diffusion and (ii) the effects on the electron distribution function of the interaction with the chamber ceramic walls, as the main aspects requiring further research.

## ACKNOWLEDGMENTS

[1] M. Martínez-Sánchez and J. Pollard, J. Propul. Power **14**, 688 (1998).

[2] *Proceedings of 38th Joint Propulsion Conference, Indianapolis, IN*, edited by American Institute of Aeronautics and Astronautics (Washington, DC, 2002).

[3] R. S. Jankovsky, D. T. Jacobson, C. J. Sarmiento, L. R. Piñero, D. H. Manzella, R. R. Hofer, and P. Y. Peterson, paper AIAA 2002-3675 in Ref. 2.

[4] R. Spores and M. Birkan, paper AIAA 2002-3558 in Ref. 2.

[5] S. Tverdokhlebov *et al.*, paper AIAA 2002-3562 in Ref. 2.

[6] *Proceedings of the 28th International Electric Propulsion Conference, Toulouse, France*, edited by Electric Rocket Propulsion Society (Cleveland, OH, 2003).

[7] G. Saccoccia, paper IEPC 03-341 in Ref. 6.

[8] V. Kim, J. Propul. Power **14**, 736 (1998).

[9] V. Zhurin, H. Kaufman, and R. Robinson, Plasma Sources Sci. Technol. **8**, R1 (1999).

[10] A. Morozov and V. Savelyev, *Reviews of Plasma Physics* (Kluwer Academic, New York, 2000) Vol. 21, Chap. 2.

[11] V. Gavryushin, V. Kim, V. Kozlov, K. Kozubsky, G. Popov, A. V. Sorokin, M. Day, and T. Randolph, in *Proceedings of the 30th Joint Propulsion Conference, Indianapolis, IN*, edited by American Institute of Aeronautics and Astronautics (Washington, DC, 1994) paper AIAA 94-2858.

[12] K. Komurasaki, K. Mikami, and D. Kusamoto, in *32nd Joint Propulsion Conference, Lake Buena Vista, FL*, edited by American Institute of Aeronautics and Astronautics (Washington, DC, 1996) paper AIAA 96-3194.

[13] J. Ashkenazy, Y. Raitses, and G. Appelbaum, Phys. Plasmas **5**, 2055 (1998).

[14] Y. Raitses, J. Ashkenazy, and G. Appelbaum in *Proceedings of the 34th Joint Propulsion Conference, Cleveland, OH*, edited by American Institute of Aeronautics and Astronautics (Washington, DC, 1998) paper AIAA 98-3640.

[15] *Proceedings of the 27th International Electric Propulsion Conference, Pasadena, CA, USA*, edited by Electric Rocket Propulsion Society (Cleveland, OH, 2001).

[16] B. Pote and R. Tedrake, paper IEPC-01-035 in Ref. 15.

[17] J. Haas and A. Gallimore, Phys. Plasmas **8**, 652 (2001).

[18] *Proceedings 37th Joint Propulsion Conference, Salt Lake City, UT*, edited by American Institute of Aeronautics and Astronautics (Washington, DC, 2001).

[19] D. Manzella, D. Jacobson, and R. Jankovsky, paper AIAA-2001-3774 in Ref. 18.

[20] L. Mason, R. Jankovsky, and D. Manzella, paper AIAA 2001-3773 in Ref. 18.

[21] R. Hofer and A. Gallimore, paper AIAA 2002-4111 in Ref. 2.

[22] N. Gascon, M. Dudeck, and S. Barral, Phys. Plasmas **10**, 4123 (2003).

[23] A. Bouchoule, A. Lazurenko, V. Vial, V. Kim, V. Kozlov, and A. Skrylnikov, paper IEPC 03-211 in Ref. 6.

[24] R. R. Hofer and R. H. R. Jankovsky, paper IEPC 03-142 in Ref. 6.

[25] *Proceedings of the 39th Joint Propulsion Conference, Huntsville, AL*, edited by American Institute of Aeronautics and Astronautics (Washington, DC, 2003).

[26] Y. Raitses, D. Staack, L. Dorf, and N. Fisch, paper AIAA 2003-5153 in Ref. 25.

[27] E. Ahedo, J. Gallardo, and M. Martínez-Sánchez, Phys. Plasmas **10**, 3397 (2003).

[28] J. M. Fife, Ph.D. thesis, Massachusetts Institute of Technology, 1998.

[29] J. Boeuf and L. Garrigues, J. Appl. Phys. **84**, 3541 (1998).

[30] G. Hagelaar, J. Bareilles, L. Garrigues, and J. Boeuf, J. Appl. Phys. **91**, 5592 (2002).

[31] E. Ahedo, J. Gallardo, and M. Martínez-Sánchez, Phys. Plasmas **9**, 4061 (2002).

[32] E. Ahedo, P. Martínez-Cerezo, and M. Martínez-Sánchez, *SP-465: Third Spacecraft Propulsion Conference, Cannes (Francia)*, edited by European Space Agency (Noordwijk, The Netherlands, 2000) pp. 323–330.

[33] E. Ahedo, J. Gallardo, F. Parra, and C. P. Trigo, paper IEPC-03-331 in Ref. 6.

[34] E. Ahedo, D. Escobar, C. Pérez, and J. Rus, paper AIAA 2003-4707 in Ref. 25.

[35] Y. Raitses, M. Guelman, J. Ashkenazy, and G. Appelbaum, J. Spacecr. Rockets **36**, 875 (1999).

[36] J. Fife, M. Martínez-Sánchez, and J. Szabo, in *Proceedings of the 33rd Joint Propulsion Conference, Seattle, WA*, edited by American Institute of Aeronautics and Astronautics (Washington, DC, 1997) paper AIAA 97-3052.

[37] E. Ahedo, Phys. Plasmas **9**, 4340 (2002).

[38] A. Bishaev and V. Kim, Sov. Phys. Tech. Phys. **23**, 1055 (1978).

[39] E. Ahedo, P. Martínez-Cerezo, and M. Martínez-Sánchez, Phys. Plasmas **8**, 3058 (2001).

[40] A. Cohen-Zur, A. Fruchtman, J. Ashkenazy, and A. Gany, Phys. Plasmas **9**, 4363 (2002).

[41] V. Khayms and M. Martínez-Sánchez, *Progress in Astronautics and Aeronautics*, edited by American Institute of Aeronautics and Astronautics (Washington, DC, 2000) Vol. 187, Chap. 9.

[42] V. Blateau, M. Martínez-Sánchez, O. Batishchev, and J. Szabo, paper IEPC 01-37 in Ref. 15.

[43] A. Morozov, Y. Esipchuk, G. Tilinin, A. Trofimov, Y. Sharov, and G. Y. Shchepkin, Sov. Phys. Tech. Phys. **17**, 38 (1972).

[44] J. Haas and A. Gallimore, in *36th Joint Propulsion Conference, Huntsville, Alabama*, edited by American Institute of Aeronautics and Astronautics (Washington, DC, 2000) paper AIAA 2000-3422.

[45] H. Kaufman, AIAA J. **23**, 78 (1985).

[46] V. Gavryushin and V. Kim, Sov. Phys. Tech. Phys. **26**, 505 (1981).

# A model of the two-stage Hall thruster discharge

E. Ahedo and F.I. Parra

*E.T.S.I. Aeronáuticos, Universidad Politécnica de Madrid, 28040 Madrid, Spain*

**Abstract**

The effect of a third, active electrode placed inside the ceramic chamber of a Hall thruster is analyzed. Both electron-collecting and electron-emitting modes are considered. Significant efficiency enhancement with respect to single-stage operation can be obtained for a good electron-emitting electrode, placed in an intermediate location of the acceleration region, and for an anode-to-electrode (inner-stage) potential significantly larger than the ionization potential. Optimum values of the electrode location and voltage are determined. The performance improvement is due to a reduction of energy losses to the chamber walls. This is the consequence of lower Joule heating and thus lower electron temperature in the outer stage. When the ionization process is efficient already in single-stage operation, (i) two-stage operation does not affect practically the propellant and voltage utilizations, and (ii) thrust efficiency decreases when the intermediate electrode works as an electron-collector.

PACS numbers: 52.75 Di

## I. Introduction

The basic two-stage configuration of a Hall thruster consists of introducing in the annular discharge chamber an additional electrode, which is biased to an intermediate potential between the upstream anode and the external cathode. Two-stage designs date back to the early times of Hall thruster development. Early Russian prototypes are reported in the review paper of Kaufman [1] (see Refs. 29 to 31 therein). Most two-stage designs are based on the idea of making the ion production process more independent of the acceleration process. The advantage would be that a high-current, low-voltage stage can be used to form the ions, while, simultaneously, the electron backflow can be minimized through the high-voltage accelerating stage, thereby maximizing acceleration efficiency [1].

Thus, a double role is assigned to the intermediate electrode: (i) to provide an additional control on the axial electric potential, and (ii) to deliver part of the electron current required for the gas ionization. The amount and *sign* of the current exchanged at the third electrode depend on the physical device and the potential bias between it and the surrounding plasma. To this respect, we distinguish between two basic types of electrodes: *passive* electrodes, capable only of collecting ions and electrons, and *active* electrodes, with the added capability of emitting electrons. Clearly, passive electrodes have a more limited ability to modify the characteristics of single-stage discharges, and only active electrodes can deliver a large electron current.

Two-stage designs for Stationary Plasma Thrusters (SPT), which have long ceramic chambers, tend to use active electrodes, whereas two-stage designs for Thrusters with Anode Layer (TAL), because of their short and metallic chambers, use passive electrodes. The strong, renewed interest on Hall thrusters over the last years has reached two-stage designs too. A recent two-stage TAL prototype is the D-80, a USA-Russia project. Experimental tests with this thruster have leaded to mixed conclusions. On the one hand, extensive tests made at NASA conclude that, in terms of efficiency, two-stage operation of the D-80 presents no clear advantage over single-stage operation [2]. On the other hand, a Russian set of experiments for the same thruster and constant anode-to-cathode (total) voltage finds that (i) the efficiency

is maximized for a certain anode-to-third-electrode (inner-stage) voltage and (ii) two-stage operation is preferable only for the high specific impulse mode [3].

Most recent two-stage SPT designs use, as third electrode, a heatable, annular plate or wire of tungsten, impregnated of a high electron emission material (BaO, $LaB_6$,...). Yamagiwa and Kuriki designed a prototype with annular electrodes in the inner and outer walls, although only the outer-wall electrode could be heated externally; increments of efficiency were found for two-stage operation, but the maximum efficiency never exceeded a 20% [4]. Fisch and colleagues tested two-stage configurations and declared that efficiencies were similar to conventional operation [5]. A prototype with an annular cathode wrapping most of the first stage, designed at Busek Co., showed no appreciable differences between the measured single-stage and two-stage performances [6]. Hofer and co-workers designed the P5-2 with an intermediate electrode located in the inner wall of the chamber. Although the electrode included a tungsten heating element to produce large electron emissions, tests were carried out without electrode heating (due to a fracture of the ceramic chamber and lack of time). It was concluded that the two-stage operation of P5-2 leads to higher thrust at the expense of efficiency [7].

This brief review shows that the performances of present, two-stage designs do not meet yet the expectations deposited on them. It remains an open question whether their limited success is caused by (a) insufficient understanding of the physics of two-stage discharges, (b) improper design or operation parameters, or (c) technical issues cancelling out any gain derived from two-stage operation. With respect to the first point there are very few theoretical studies of two-stage discharges. Fruchtman and Fisch [8], using a simple one-dimensional(1D) model (of the plasma acceleration region *only*), showed that an optimal distribution of *electron-emitting* electrodes reduces the electron heating in that region and thus enhances the thrust efficiency. For a single intermediate electrode they found that the maximum efficiency gain, at the optimum location and voltage of the third electrode, is lower than a 6%. In a parallel publication, Fruchtman, Fisch, and Raitses [9] analyzed a more complete 1D model of a two-stage discharge and showed that the efficiency can be enhanced *also* by using an *electron-collecting* electrode placed exactly at the sonic transition of the ion flow.

The main limitations of the model of Ref. [9] are: (i) to consider constant the electron temperature along the channel and for different operation conditions; (ii) to fix the *moving* sonic transition point at the location of the electrode; and (iii) to neglect the ion backstreaming region. In this paper we present a model that overcomes these drawbacks. It is based on the single-stage model of Ahedo *et al.* [10] and is applicable mainly to (i) thrusters with long ceramic chambers (SPT-type) and, therefore, large wall energy losses, and (ii) to electrodes with a large capability of exchanging electrons with the plasma discharge. Both the electron emission and collection modes of the electrode will be discussed, but the study will be focused on the more interesting one, the electron-emission mode. Beyond presenting the key physics governing each stage of the discharge, we carry out an extensive parametric study to determine the influence of the location and voltage of the third electrode, for given mass flow and total discharge voltage. The results of our model show that the efficiency can be improved significantly by using an electron-emitting electrode and suggest appropriate location and voltage for that electrode.

In several of the experiments commented previously, two-stage designs are envisaged in connection with dual-mode operation of Hall thrusters. Indeed, certain authors propose to use two-stage operation for the high specific impulse (i.e. high discharge voltage) mode, but to keep single-stage operation for the high thrust (i.e. moderate discharge voltage) mode. Clearly, 'dual-mode' and 'two-stage' are independent concepts. 'Two-stage' refers mainly to the thruster configuration, whereas 'dual-mode' refers to the operation conditions. In this paper we study the influence of the third electrode parameters, but a full parametric characterization of a two-stage thruster (and, in particular, its dual mode operation) is beyond the goals of this work.

The rest of the paper is organized as follows. In Section II we present the two-stage model and the parameters that determine the plasma response. In Section III, we derive some analytical laws useful to evaluate the numerical solutions. In Section IV, we discuss the behavior of two-stage discharges and determine the influence of the location and voltage of the third electrode. Conclusions and final comments are presented in Sec. V.

## II. Formulation of the model

### A. Hypotheses

The two-stage model is a natural extension of the single-stage model presented in Ref. [10]. Sketches of the two-stage discharge are shown in Fig. 1. The main features of the discharge model are the following.

1) The model is stationary, macroscopic, and considers three plasma populations: ions($i$), electrons($e$), and neutrals($n$).

2) The average Debye length of the plasma, $\lambda_D$, is assumed to be much smaller than the typical length of the axial gradients (which usually is a fraction of the chamber length, $L_c$). Thus, plasma quasineutrality applies everywhere except in Debye sheaths around the chamber walls.

3) The equations for the axial response consider plasma magnitudes that are radially-averaged values of the corresponding two-dimensional(2D) variables. For instance, the $r$-averaged electrostatic potential is defined as

$$\phi(x) = \frac{1}{A(x)} \int_{r_{in}}^{r_{out}} \bar{\phi}(x, r) 2\pi r dr, \tag{1}$$

with $\bar{\phi}(x, r)$ the 2D potential, $r_{in}(x)$, $r_{out}(x)$, and $A(x)$, the inner radius, the outer radius, and the radial area of the plasma jet, respectively.

4) The magnetic field for the 1D, axial response is assumed of the form $\boldsymbol{B} = B_r(x)\mathbf{1}_r$, $B_r(x) = B_{max}b_r(x)$, with $B_{max}$ and $b_r(x)$ the strength and normalized shape of the magnetic field, respectively. This magnetic field must be considered as an $r$-averaged field for the 1D model, where 2D features (such as the $x$-component of the field or the dependence on $r$ ) are ignored of necessity.

5) In addition to collisions with heavy species and wall collisionality, the electron diffusive motion is affected by turbulent (i.e. anomalous or Bohm-like) diffusion. We define the anomalous diffusion frequency as $\nu_{ano} = \alpha_{ano}\omega_e$, with $\omega_e = eB/m_e$ the electron gyrofrequency and $\alpha_{ano}$ the relative level of correlated azimuthal fluctuations [10, 11], which, in the absence

of a satisfactory theory, is assumed constant along the channel and is adjusted by fitting the model solutions to available experimental results.

6) The effects of the plasma interaction with the lateral walls are included in the axial equations as volumetric source terms. Their functional form are obtained from the radial model of Ahedo [13]. This considers the sheath/presheath/sheath structure between the lateral walls and takes into account secondary electron emission(SEE). For high SEE the charge-saturation of the negative (i.e. ion-attracting) sheaths prevents them from vanishing.

The novel features of the two-stage model are the following.

7) The two-stage discharge is accomplished through an intermediate electrode, placed inside the chamber. This $r$-averaged model does not distinguish whether the electrode is placed at the inner or outer wall. The electrode is treated similarly to the neutralization surface of the external cathode. The axial width of the electrode, $\Delta x_{int}$, is assumed to satisfy

$$\lambda_D \ll \Delta x_{int} \ll L_c, \tag{2}$$

so that we can consider that the exchange of electrical current at the intermediate electrode, $I_{d1}$, takes place at a single axial position, point R in Fig. 1. (In a 2D model this current would be delivered along the magnetic field line intersecting the electrode).

8) The two-stage discharge is controlled by the total discharge voltage, $V_d$, and the inner-stage voltage, $V_{d1}$; thus, the outer-stage voltage is $V_{d2} = V_d - V_{d1}$. Although it is electrically equivalent to operate on the pairs $(V_{d1}, V_d)$ and $(V_{d1}, V_{d2})$, to work with the first pair is found more convenient in order to interpret the plasma response. (In addition, since the third electrode can be placed at any axial location within the chamber, we will avoid the names ionization and acceleration voltages for $V_{d1}$ and $V_{d2}$, respectively, used by some authors.)

9) The currents exchanged at the intermediate electrode and at the external cathode, $I_{d1}$ and $I_{d2}$, respectively, are obtained as part of the plasma/thruster response. The cathode current, $I_{d2}$, is positive, but $I_{d1}$ can be either positive or negative. The total discharge current through the anode is $I_d = I_{d1} + I_{d2}$.

10) The voltages applied at each stage and the $r$-averaged values of the plasma potential

at sections A, R and P, satisfy

$$\phi_A - \phi_R = V_{d1} - V_{int}(I_{d1}), \qquad \phi_A - \phi_P = V_d - V_{cat}(I_{d2}). \tag{3}$$

Here, $V_{int}$ and $V_{cat}$ are the differences between the potentials of the respective electrodes and the $r$-averaged plasma potentials at sections R and P, respectively. The effective current-voltage curves of the electrodes, $V_{cat}(I_{d2})$ and $V_{int}(I_{d1})$, are supposed to be known. In general, the external cathode is of the hollow-cathode type and should work in the spot mode, characterized by emitting a high electron current with a relatively low potential voltage, $V_{cat} \sim 15 - 20\mathrm{V}$. The other function, $V_{int}(I_{d1})$, depends on the kind of electrode is used. Only the ideal, zero-impedance cases (i.e. $V_{cat}, V_{int} \ll V_d$) are treated in the present paper.

The rest of the hypotheses of the two-stage model are the same ones used in the single-stage model of Ref. [10]. Unless otherwise is stated, the nomenclature is the same too.

## B. Equations

Except for a non-neutral sheath at the anode, the plasma is quasineutral and satisfies the set of equations

$$\frac{d\Gamma_{xi}}{dx} = -\frac{d\Gamma_{xn}}{dx} = S_i - S_w, \tag{4}$$

$$\frac{d\Gamma_{xe}}{dx} = S_i - S_w + S_{Pe} + S_{Re}, \tag{5}$$

$$\frac{d}{dx}(m_i v_{xi}\Gamma_{xi}) = -en_e A\frac{d\phi}{dx} + m_i(v_{xn}S_i - v_{xi}S_w), \tag{6}$$

$$\frac{d}{dx}(m_i v_{xn}\Gamma_{xn}) = m_i(v_{xnw}S_w - v_{xn}S_i), \tag{7}$$

$$0 = -v_{xe}\omega_e - \nu_e v_{\theta e}, \tag{8}$$

$$0 = -\frac{d}{dx}n_e T_e + en_e\frac{d\phi}{dx} + \omega_e m_e n_e v_{\theta e}, \tag{9}$$

$$\frac{d}{dx}\left(\frac{5}{2}T_e\Gamma_{xe} + q_{xe}A\right) = e\Gamma_{xe}\frac{d\phi}{dx} - \alpha_i E_i S_i - \beta_e T_e S_w + \frac{5}{2}T_P S_{Pe} + \frac{5}{2}T_R S_{Re}, \tag{10}$$

$$\frac{dT_e}{dx} = -\frac{2m_e\omega_e^2}{5n_e T_e \nu_e}q_{xe}. \tag{11}$$

Here, $m_\alpha$, $n_\alpha$, $T_\alpha$, and $\boldsymbol{v}_\alpha$, with $\alpha = i, e, n$, have the conventional meaning, $q_{xe}$ is the axial heat conduction flux for the electrons, and $\Gamma_{x\alpha} = An_\alpha v_{x\alpha}$ are particle axial flows. The four source terms for plasma production,

$$
\begin{aligned}
S_i &= An_e\nu_i, & S_{Re} &= \delta(x - x_R)I_{d1}/e, \\
S_w &= An_e\nu_w, & S_{Pe} &= \delta(x - x_P)I_{d2}/e,
\end{aligned}
\tag{12}
$$

represent ionization, wall-recombination, and electron emission at the electrode and the cathode, respectively; $\delta(x)$ is the Dirac function. Notice that the 1D model treats similarly the volumetric term $S_i$ and the other three terms, which model the contributions of walls and electrodes. In Eq. (7), $v_{xnw}$ is the average axial velocity of neutrals generated by wall recombination. In Eq. (8),

$$
\nu_e = \nu_{en} + \nu_{ei} + \beta_m\nu_w + \alpha_{ano}\omega_e
\tag{13}
$$

is the perpendicular collision frequency for electrons, which includes the effects of collisions with neutrals and ions, secondary/primary electron exchanges at the lateral walls ('wall collisions'), and anomalous diffusion. In Eq. (10): $T_R$ and $T_P$ are the temperatures of the electrons exchanged at electrodes R and P, respectively; $\alpha_i E_i$ is the ionization energy cost (per ion); and $\beta_e T_e S_w$ represents the electron energy cost due to the interaction with the lateral walls. Expressions for $\nu_i$, $\nu_w$, $\nu_e$, $\alpha_i$, $\beta_m$, $\beta_e$, and $v_{xnw}$ are given in Ref. [10].

From the continuity equations the axial flows satisfy

$$
\Gamma_{xi}(x) + \Gamma_{xn}(x) = \dot{m}_A/m_i,
\tag{14}
$$

$$
\Gamma_{xi}(x) - \Gamma_{xe}(x) = \begin{cases} I_d/e, & x < x_R, \\ I_{d2}/e, & x_R < x < x_P, \end{cases}
\tag{15}
$$

with $\dot{m}_A$ the anode mass flow.


## C. Jump conditions across the intermediate electrode

In the limit of a thin electrode expressed by conditions (2), certain plasma magnitudes

experiment a jump across the electrode location, $x = x_R$. These jumps are determined from integrating the plasma equations from $x_R^-$ to $x_R^+$. Notice that the first part of condition (2) implies that the discharge can afford the exchange of electrical current at point R without creating any non-neutral double-layer. Thus, any possible jump of the electric potential across point R must come out from the plasma quasineutral equations.

In the model we are considering, only the electron equations for particle number and energy, Eqs. (5) and (10), are affected by the exchange of current at the intermediate electrode. Then, the integration of the equations across point R yields that $v_{xi}$, $n_e$, $T_e$, and $\phi$ remain constant, whereas the jumps of the electron axial flows of particles and energy satisfy

$$\Gamma_{xeR}^+ - \Gamma_{xeR}^- = I_{d1}/e, \tag{16}$$

$$(q_{xeR}^+ - q_{xeR}^-)A_c = (T_R - T_{eR})5I_{d1}/2e, \tag{17}$$

with $T_{eR}$ the electron temperature at point R, and $T_R$ the temperature of the electrons exchanged at the intermediate electrode. These equations express the conservation of the electron density and energy across the electrode location. Since $n_{eR}^+ = n_{eR}^-$, the jump of the electron current implies a jump of the electron axial velocity,

$$v_{xeR}^+ - v_{xeR}^- = I_{d1}/en_{eR}A_c \tag{18}$$

(notice that $v_{xe} < 0$).

### D. Boundary conditions and structure of the discharge

The boundary conditions of the plasma equations for the two-stage case consist of those ones of the single-stage model plus the above jump conditions across point R. In the limit of zero intermediate current, $I_{d1} = 0$, we pretend the two-stage model to recover the *normal operation class* of solutions of Ref. [10]. These present an axial structure consisting of the regions sketched in Fig. 1.

First, there is the negative anode sheath (region AB). The sheath potential, $\phi_{AB} \equiv$

9

$\phi_B - \phi_A > 0$, is self-adjusted in order that the electron flow from the channel is the flow collected by the anode. The sheath/plasma transition (point B) is defined by a sonic Bohm condition on the ion reverse flow.

According to Ref. [10], the normal operation class of solutions exists only for the ion reverse current at the anode, $I_{iA} = e\Gamma_{xiA}$, satisfying

$$0.514 \times 10^{-2} < -I_{iA}/I_d < 11.4 \times 10^{-2}. \tag{19}$$

The lower limit of $|I_{iA}|$ corresponds to $\phi_{AB} = 0$, that is to the vanishing of the negative anode sheath. The upper limit corresponds to plasma flow conditions that seem not to allow a stationary presheath/sheath transition [12]. Therefore, the range defined by Eq. (19) is independent of any current exchange at an intermediate electrode and applies to two-stage operation too.

Points D and S in Fig. 1 correspond to zero and (forward) sonic ion velocities and are determined as part of the solution. Points E and P define the chamber exit surface and the beam neutralization surface. Region BD is the ion backstreaming region, which is characterized by a large pressure gradient, a near-zero electric field, and weak gas ionization. Region DS is the main ionization region, and regions SE and EP are the internal and external acceleration regions, where most of the electric potential drop takes place. Ionization and wall recombination frequencies tend to compensate each other in the acceleration regions [10]; therefore, ion and electron flows are almost constant there. Notice that magnetic effects are still significant in the external acceleration region EP.

Point S is determined as part of the solution and its location changes with the parameters controlling the thruster operation point. The model admits to place the third electrode (point R) anywhere inside the chamber, so that point S can be at any side of the electrode R. Nevertheless, we will deal mainly with parametric regions where point S is located inwards of point R since, for an electron-emitting electrode, this assures that the intermediate current is used mainly to ionize the gas. Notice that Fruchtman et al. [9] claimed that the operation of the third electrode forces an abrupt sonic transition to occur exactly at the electrode location,

and thus *imposed* the condition $x_R = x_S$ to all their two-stage solutions.

### E. Input parameters for the integration

The geometrical, operational, and phenomenological parameters needed to integrate the two-stage model are the following.

1) The chamber dimensions: radial width $h_c$, radial area $A_c$, and axial length $L_c$ (we take $x_A = 0$ and $x_E = L_c$).

2) The distance between the chamber exit and the neutralization surface, $L_{EP} \equiv x_P - x_E$.

3) The location of the intermediate electrode, $L_{AR} \equiv x_R$.

4) The temperature $T_1$ of primary electrons that produces a 100% SEE yield from the walls. The model yielding Eq. (A12) of Ref. [10] is used to compute the effective SEE yield.

5) The anode mass flow rate, $\dot{m}_A$, and the average axial velocity of the emitted gas, $v_{xnA}$.

6) The total and inner-stage voltages, $V_d$ and $V_{d1}$.

7) The temperature of the electrons emitted by the cathode, $T_P$. Since all electrons at point P come from the cathode, one has $T_{eP} = T_P$.

8) The temperature of the intermediate electron current, $T_R$. We take $T_R = T_{eR}$ for an electron-collecting electrode, and $T_R = T_P$ for an electron-emitting one.

9) Three empirical parameters: the Bohm parameter measuring the level of turbulent diffusion [$\alpha_{ano}$ in Eq. (A23) of Ref. [10]]; the plasma wall-recombination factor [$\tilde{\nu}_w$ in Eq. (A6) of Ref. [10]]; the accommodation factor for the axial velocity of the recombined ions [$a_w$ in Eq. (13) of Ref. [10]].

10) The axial profile of the radial magnetic field. The shape of this profile, $b_r(x)$, is kept fixed, whereas the maximum magnetic field strength, $B_{max}$, is adjusted in order that condition (19) is satisfied (i.e. the solution presents a negative anode sheath). For the rest of parameters given, this restricts the range of values of the maximum magnetic field strength, $B_{max}$, to a thin variation band (of around a 10%, according to Fig. 6 of Ref. [12]).

### III. Analytical relations of interest

## A. Energy balance

The external electrical power spent in a two-stage discharge is

$$P_d = I_d V_{d1} + I_{d2} V_{d2} = I_d V_d - I_{d1} V_{d2}. \tag{20}$$

Defining

$$P_\alpha(x) = \Gamma_{x\alpha} \left( \frac{1}{2} m_i v_{x\alpha}^2 + \frac{5}{2} T_\alpha \right) + q_{x\alpha} A \tag{21}$$

as the axial energy flow carried by species $\alpha$, the useful power extracted from the thruster is

$$P_{use} = P_{iP} + P_{nP} \simeq \sum_{\alpha=i,n} \frac{1}{2} \dot{m}_{\alpha P} v_{x\alpha P}^2. \tag{22}$$

(Since our model is not reliable at the far plume, we do not integrate beyond point P and thrust and useful power will be computed from plasma values at point P.) The $r$-averaged energy balance of the whole plasma allows us to evaluate the different contributions to the energy losses, $P_{loss} = P_d - P_{use}$. Equation (10) yields the axial variation of the energy flow of the electron population. From the equations of ions and neutrals the total energy flow of ions and neutrals satisfy

$$\frac{d}{dx}(P_i + P_n) = -e\Gamma_{xi} \frac{d\phi}{dx} - S_w \left[ \frac{5}{2} T_i + \frac{1}{2} m_i (v_{xi}^2 - v_{xnw}^2) \right] \tag{23}$$

(the ion temperature, $T_i$, neglected in Eq. (6), is included here for a consistent balance of the total energy of the heavy species). Adding Eqs. (10) and (23), and integrating for each stage of the discharge, one has

$$I_d \phi_{RA} = (P_i + P_n + P_e) \Big|_A^{R^+} + \int_A^R (Q_{wall} + Q_{ion}) dx + \frac{5 T_R}{2e} I_{d1}, \tag{24}$$

$$I_{d2} \phi_{PR} = (P_i + P_n + P_e) \Big|_{R^+}^P + \int_R^P (Q_{wall} + Q_{ion}) dx + \frac{5 T_P}{2e} I_{d2}, \tag{25}$$

with

$$Q_{ion} = \alpha_i E_i S_i, \qquad Q_{wall} = \left[ \frac{1}{2} m_i (v_{xi}^2 - v_{xnw}^2) + \frac{5}{2} T_i + \beta_e T_e \right] S_w, \tag{26}$$

12

the local losses (per unit of axial length) due to ionization and plasma interaction with the lateral walls, respectively. The dimensionless parameter $\beta_e$, measuring the radial losses to the walls, increases dramatically in zones where the SEE yield approaches a 100% (i.e. $T_e \simeq T_1$) and the lateral sheaths become space-charge saturated [13].

Adding Eqs. (3), (24), and (25), the energy losses can be written as

$$P_{loss} = P_{ion} + P_{wall} + P_{ano} + P_{int} + P_{plu}, \tag{27}$$

where

$$P_{ion} = \int_A^P Q_{ion} dx, \qquad P_{wall} = \int_A^P Q_{wall} dx, \qquad P_{ano} = -(P_i + P_n + P_e)|_A,$$

$$P_{int} = I_{d1}(V_{int} - \frac{5}{2}\frac{T_R}{e}), \quad P_{plu} = I_{d2}(V_{cat} - \frac{5}{2}\frac{T_P}{e}) + P_{eP}, \quad (28)$$

represent ionization, heat deposited at lateral walls, heat deposition at the anode, losses due to the current exchanged at the intermediate electrode, and losses in the near-plume, respectively.

## B. Partial efficiencies

The thrust satisfies

$$F = \sum_{\alpha=i,n} \dot{m}_{\alpha P} v_{x\alpha P}. \tag{29}$$

Partial efficiencies of interest are defined as in Ref. [14]:

$$\eta = F^2/2\dot{m}_A P_d, \qquad \eta_{prop} = P_{use}/P_d, \qquad \eta_u = \dot{m}_{iP}/\dot{m}_A,$$

$$\eta_{vol} = m_i v_{xiP}^2/2eV_d, \qquad \eta_{cur} = I_{iP}V_d/P_d \quad (30)$$

mean thrust and propulsive efficiencies, and propellant, voltage, and (generalized) current utilizations, respectively. The difference between the thrust and propulsive efficiencies comes from the incomplete ionization, which means that the ejected plasma beam includes two heavy

species with different velocities. One has [14]

$$\eta \simeq \eta_u \eta_{prop}, \quad \eta_{prop} \simeq \eta_{vol} \eta_{cur}, \quad \eta_{cur} \simeq \eta_u I_m V_d / P_d, \tag{31}$$

with $I_m = e\dot{m}_A / m_i$ and $I_m V_d$ the ideal maxima of ion current and useful power, respectively (for given values of the two main operation parameters, $\dot{m}_A$ and $V_d$). The analysis of single-stage discharges shows that $\dot{m}_A$ and $V_d$ affect mildly both $\eta_{vol}$ and $\eta_u$ (within the operation regime of interest to us) [14]. Therefore the most promising way of enhancing $\eta$ is to increase $\eta_{cur}$ by reducing the energy losses and thus $P_d$. Since $P_{ano}$ and $P_{plu}$ are small, and there is little margin to decrease the ionization losses, a two-stage design must focus on reducing $P_{wall}$. This can be accomplished by limiting the plasma temperature in the acceleration regions in order to avoid the presence of regions with charge-saturated sheaths, which lead to large energy depositions at the walls.

## C. Scaling laws for the magnetic field

Once an axial shape of the magnetic field is selected, the value of the magnetic field strength, $B_{max}$, is adjusted in order to provide the correct diffusion of the axial electron flow across the chamber [and a reverse flow of ions within the range of Eq. (19)]. Approximate solutions of the plasma equations, discussed in Ref. [14], give the scaling law for the parametric dependence of $B_{max}$ on $V_d$ for single-stage operation. Using the same approximations than there, scaling laws for the first and second acceleration regions (regions SR and RP in Fig. 1) are

$$\sqrt{\frac{2eV_d}{m_i}} - \sqrt{\frac{2eV_{d1}}{m_i}} \simeq \frac{I_{d2} - I_{iP}}{I_{iP}} \{\bar{\nu}_d\}_{RP} L_{RP}, \tag{32}$$

$$\sqrt{\frac{2eV_{d1}}{m_i}} - \sqrt{\frac{2e\phi_{SA}}{m_i}} \simeq \frac{I_d - I_{iP}}{I_{iP}} \{\bar{\nu}_d\}_{SR} L_{SR}, \tag{33}$$

where: {} means average value over the respective region;

$$\bar{\nu}_d = \frac{m_e}{m_i} \frac{\omega_e^2}{\nu_e} \tag{34}$$

14

is a normalized perpendicular collision frequency of electrons (with $\bar{\nu}_d \propto B_{max}/\alpha_{ano}$ if turbulent diffusion dominates); $L_{RP} \equiv x_P - x_R$ is known; and $L_{SR} = x_R - x_S$ changes with the operation point. To complete these two scaling laws we need a third one for the length of the ionization and backstreaming regions, $L_{AS} = L_{AR} - L_{SR}$. There is no simple, correct expression for that length, but

$$L_{AS} \propto \{\bar{\nu}_d \nu_i\}_{AS}^{-1/2} \tag{35}$$

can be accepted as a rough estimate [14, 15]. These three scaling laws will be used later to interpret the plasma response and the dependence of $B_{max}$ on $V_{d1}$ and $x_R$.

## IV. Parametric investigation of the two-stage operation

### A. Evolution with the intermediate voltage

Numerical results are presented for the same thruster considered in Refs. [10] and [14], which simulates a SPT-100. Figure 2(a)-(f) analyze the influence of the first-stage voltage, $V_{d1}$, on the performances, for a fixed position of the intermediate electrode. The total discharge voltage and the mass flow are kept constant so that the variation on the discharge power is related directly to the exchange of current at the electrode. Main input parameters of the thruster are listed in the caption of Fig. 2; the chamber length is $L_c = 25$mm and the electrode is placed at 14.5 mm from the anode. The axial shape of the magnetic field, $b_r(x)$, is the same one plotted in Fig. 2 of Ref. [10]. For each operation point, the magnetic field strength, Fig. 2(a), has been adjusted in order that $-I_{iA}/I_d$ lie in the interval $0.012 - 0.025$.

Figures 3(a)-(e) depict axial profiles of the plasma response for three particular points of Fig. 2. One-stage operation ($I_{d1} = 0$ and dashed-line curves of Fig. 3) is achieved for $V_{d1} = 18$V and yields a thrust efficiency of 52%. As $V_{d1}$ is increased from that floating value, electron current is emitted into the discharge at point R. The solid-line curves of Fig. 3 depict the discharge response for $V_{d1} = 137$ V (i.e. $V_{d1}/V_d \simeq 46\%$), when the intermediate current is $I_{d1} \simeq 1.3$ A and the thrust efficiency is maximum and equal to 62%. The dash-and-dot curves of Fig. 3 plot the response for $V_{d1} = 196$ V, when $I_{d1} \simeq 1.5$ A and $\eta \simeq 60\%$.

The evolution of $I_{d1}(V_{d1}) = I_d - I_{d2}$ can be seen in Fig. 2(b). As both the total discharge current and the ion final current, $I_d$ and $I_{iP}$, are found to change weakly with $V_{d1}$, it turns out that the increments of $I_{d1}$ are followed by decrements of the same magnitude of both the electron current emitted by the cathode, $I_{d2}$, and the outer-stage reverse current of electrons, $I_{d2} - I_{iP}$. For the cases plotted in Fig. 3 and for $V_{d1}$ increasing, this reverse electron current decreases from 1.88 A to 0.46A and 0.25 A. Since a certain reverse electron current is needed to sustain the quasineutral discharge in the outer stage, the low value of $I_{d2} - I_{iP}$ for $V_{d1} = 196$V could explain partially the numerical difficulties we have found to obtain solutions for larger values of $V_{d1}$. [To this respect, we do not see any theoretical obstacle in the model preventing the existence of solutions for higher values of $V_{d1}$. Indeed, the model would allow $V_{d1}$ to approach $V_d$ and the intermediate electrode to become the effective cathode].

At the floating-potential (or single-stage) case, the ionization region ends at $x_S = 12.9$mm, near the location of the intermediate electrode. The potential drop in the backstreaming and ionization regions is practically independent of the intermediate electrode operation; one has $\phi_{SA} \equiv \phi_A - \phi_S \sim T_{eS}/2e$ or, more specifically, $\phi_{SA} = 7.4$ V and 6.9 V for $V_{d1} = 18$ V and 137 V, respectively. Since $\phi_{SA}$ is small, the potential drop in the inner acceleration region, $\phi_{RS} \equiv \phi_S - \phi_R$, tends to be proportional to $V_{d1}$. Then, as $V_{d1}$ becomes larger and in order to accommodate the larger potential difference $\phi_{RS}$, point S moves away from point R [Fig. 2(c)]. At the maximum efficiency case ($V_{d1} = 137$V) point S is placed at $x_S = 8.1$mm, almost at mid-distance from the anode and the intermediate electrode.

Figure 2(e) shows that the propellant utilization is affected weakly by the intermediate electrode operation (in agreement with the conclusions of Ref. [10]). The small variation of $\eta_u(V_{d1})$ seems to be due to the variation of the maximum electron density in the ionization region [Fig. 3(e)]. Then, $\eta \simeq \eta_u \eta_{prop}$ presents the same evolution with $V_{d1}$ than $\eta_{prop}$ [Fig. 2(e)]. The propulsive efficiency depends on the useful and lost power, both shown in Fig. 2(f). We observe that $P_{wall}$ is the dominant contribution to $P_{loss}$, and $P_{use}$ varies weakly with the intermediate electrode operation. As a result, the maxima of $\eta_{prop}(V_{d1})$ and $\eta(V_{d1})$ correspond to the minimum of $P_{wall}(V_{d1})$ approximately.

As commented in Sec. III, $P_{wall}$ is strongly affected by the temperature profile. Since

the increase of $V_{d1}$ means a reduction of both $V_{d2}$ and $I_{d2}$, the plasma heating, the electron temperature, and the wall energy losses will be lower in the outer-stage (region RP). But, simultaneously, the increase of $V_{d1}$, means a larger plasma heating in the inner acceleration region SR. As a consequence, for large enough values of $V_{d1}$, the charge-saturation of the lateral sheaths tends to disappear from region RP and to appear in region SR. This is well illustrated by the three temperature profiles plotted in Fig. 3(d) and the behavior of the maximum electron temperature, $T_{e,max}(V_{d1})$, in Fig. 2(d). The change of tendency of $T_{e,max}(V_{d1})$ at $V_{d1} \sim 105V$ is due to the change on the location of the maximum temperature, from region RP to region SR. The fact that wall energy losses increase largely when there is a large axial zone with sheath saturation, explains that the minima of $T_{e,max}(V_{d1})$ and $P_{wall}(V_{d1})$ [Figs. 2(d) and 2(f)], are close to each other. The main conclusion is that maximum efficiency is obtained when the two-stage operation generates a rather flat temperature profile, with few zones with charge-saturated sheaths.

The small variation of the total discharge current with $V_{d1}$, Fig. 2(b), is due to the following. In one stage operation (and for $\dot{m}_A$ given), $I_d$ is determined mainly by the amount of power losses through the expression $I_d \simeq \eta_u \eta_{vol}(e\dot{m}_A/m_i) + P_{loss}/V_d$. In two stage operation this expression becomes

$$I_d \simeq \eta_u \eta_{vol} \frac{e\dot{m}_A}{m_i} + \frac{P_{loss} + I_{d1}V_{d2}}{V_d}. \tag{36}$$

Thus, from Eqs. (20) and (36), $I_d \sim const$ means that the gain in discharge power is $I_{d1}V_{d2}$ and this comes almost entirely from reducing $P_{wall}$. Since $I_{d1}V_{d2}$ is of the order of the reduction of Joule heating in the outer stage, it turns out that $I_d \sim const$ is mainly the result of the balance between Joule heating and wall energy losses in the outer stage.

Figure 2(a) shows that a significant increase of $B_{max}$ with $V_{d1}$ is needed to keep the two-stage discharge within the normal operation class (i.e. with a negative anode sheath and an ion backstreaming region); $B_{max}$ doubles from single-stage to efficient two-stage operation. Equation (33) provides the basic relationship to understand the behavior of $B_{max}(V_{d1})$: the increase of $V_{d1}$ requires to increment $(L_{AR} - L_{AS})B_{max}$, and this is accomplished by a larger $B_{max}$ [which, according to Eq. (35), yields a shorter $L_{AS}$ too]. The plasma equations leading

17

to Eq. (33) [see Eq.(9) of Ref. [14]] provide the physical explanation in terms of plasma magnitudes. A larger potential jump between R and S means a larger increment of $v_{xi}$ and, because of plasma quasineutrality, of $v_{xe}$ too. The increment of $v_{xe}$ satisfies

$$\Delta v_{xe} \sim - \int_S^R dx \ \bar{\nu}_d \Gamma_{xe}^2 / \Gamma_{xi}^2 \tag{37}$$

and thus is almost proportional to $\bar{\nu}_d$.

The variation of the magnetic field strength affects the electron flow in the following way. In the outer stage, the balance between a larger $B_{max}$ and lower electron current and electric field is given by Eq. (32), which basically states that

$$B_{max} \propto \frac{V_d^{1/2} - V_{d1}^{1/2}}{I_{d2} - I_{iP}}. \tag{38}$$

In the ion backstreaming region, Eqs. (8) and (9), together with $I_d \sim$ const, indicate that the electron pressure increases nearly proportional to the magnetic field,

$$\{n_e T_e\}_{BD} \propto \{|\boldsymbol{B}|\}_{BD} \propto B_{max}; \tag{39}$$

Fig. 3 shows that this pressure increment comes from the temperature increase in the near-anode region.

There is no experimental data that could guide us on the variation of the anomalous diffusion parameter, $\alpha_{ano}$, with the operation conditions of a two-stage thruster. Thus, we used the same value, $\alpha_{ano} \simeq 1.24\%$, for all cases computed in the paper. (This value was adjusted in Ref. [10] by fitting single-stage solutions to experimental results of the SPT-100 thruster.) However, results are totally valid for other values of $\alpha_{ano}$, because of $B_r(x)$ and $\alpha_{ano}$ appear in the equations only in one parameter, the perpendicular collision frequency $\bar{\nu}_d$, defined in Eq. (34). Thus, any solution of the discharge computed here is valid for pairs $(B_r(x), \alpha_{ano})$ that keep $\bar{\nu}_d(x)$ invariant. When turbulent diffusion dominates over the rest of collisional effects, that condition reduces to keep $B_r(x)\alpha_{ano}^{-1}$ invariant, Then, were $\alpha_{ano}$ vary with the operation point, Fig. 2(a) would represent the way the ratio $B_{max}\alpha_{ano}^{-1}$ (instead

of $B_{max}$) needs to be adjusted; the same is true with Eqs. (38) and (39). Therefore, the turbulent diffusion level affects the magnetic field strength that must be applied, but not the maximum efficiency gain that can be achieved.

## B. The electron-collecting mode

Figure 2 includes also results for the intermediate electrode operating as an electron-collector. When $V_{d1}$ decreases from the floating value of 17.9 V, the current at the intermediate electrode, $I_{d1}$, starts to be negative. Our results show that this operation regime is clearly disadvantageous: part of the reverse electron current emitted by the external cathode is heated at the outer-stage and collected back at point R without performing any useful task (i.e. ionization). Figure 2(d)-(f) illustrate the extra heating of the plasma, with a negative impact on energy losses and efficiency. At the same time, a lower potential drop in region AR does not produce any relevant enhancement of the propellant utilization.

With respect to the position of the ionization region, Fig. 2(c) shows that, as $V_{d1}$ decreases, point S approaches the intermediate electrode and eventually crosses it; one has $V_{d1} = 9.1$ V and $I_{d1} = -0.3$ A when $x_S = x_R = 14.5$ mm. Computations with point S outwards of point R were not performed since new and interesting results were not foreseen. When the intermediate electrode is placed upstream of the ionization region, (i.e. $x_D > x_R$), it is expected to act as the main anode; this could be the situation in some experiments with the P5-2 [7].

Fruchtman *et al.* [9] found that the thruster efficiency can be improved significantly by using an electron-collecting electrode. The discrepancy with our conclusions is explained from differences in both the model and the cases presented. On the one hand, they consider single-stage cases where ionization covers the whole channel and the values of $\eta_{vol}$ and $\eta_u$ are relatively low (whereas we depart from single-stage cases with $\eta_u > 80\%$ and $\eta_{vol} > 90\%$). For such cases the main role of the intermediate electrode seems to be to modify the electric potential profile in order to force the ionization region to occupy only one part of the channel, thus enhancing the propellant and voltage utilizations. On the other hand, although

recognizing the importance of the temperature evolution along the chamber, they take, for simplicity, $T_e(x)$ (and the ionization rate) constant and the *same value* for single-stage and two-stage operations. Thus, by avoiding to solve the energy equation, they do not realize that the energy losses tend to increase in the electron-collecting mode, penalizing the current utilization and thrust efficiency.

## C. Influence of the location of the intermediate electrode

Figures 4(a)-(f) present the results of a bi-parametric study on the influence of the position and the bias voltage of the intermediate electrode, $x_R$ and $V_{d1}$, on the thruster performance (for fixed values of $V_d$ and $\dot{m}_A$). The investigation covers a wide range of variation (over a 50%) of both $V_{d1}/V_d$ and $x_R/L_c$. The solid thick lines represent the single-stage operation or floating-potential case for the intermediate electrode. The dashed thick lines correspond to $x_R = x_S$, when the ion sonic point lies exactly at the intermediate electrode position. The change on the magnitude of the magnetic field profile in Fig. 4(a) reflects the adjustment required by $B_{max}(x_R, V_{d1})$ for the plasma discharge to lie within the normal operation regime.

Figure 4(b) plots the fraction of electron current exchanged at the intermediate electrode, $I_{d1}/I_d$, which reaches up to a 30%. Figure 4(c) plots the evolution of the efficiency, $\eta(x_R, V_{d1})$. The asterisk represents the point of maximum efficiency, about 62%, which is reached for $x_R = 14.5$mm and $V_{d1} = 137$V (the solid-line case of Fig. 3). Therefore, for this thruster and $V_d \sim 300$V, the ideal two-stage discharge model yields a 19% of efficiency improvement with respect to single-stage operation. As important as this result is the fact that $\eta(x_R, V_{d1})$ remains close to that maximum for a wide interval of voltages and positions of the electrode. For instance, one has $\eta > 0.60$ for $V_{d1} = 125$V and $x_R$ in the interval 11-18 mm, or for $x_R = 14.5$ mm and $V_{d1}$ in the range 100-200 V.

We saw in Sec. IV.A that $\eta_u$ is practically independent of $V_{d1}$ (in the region of interest, $V_{d1} \sim 100 - 150$V). Figure 4(d) shows that $\eta_u$ depends weakly on $x_R$. Then, the behavior of $\eta_{prop}(x_R, V_{d1}) \simeq \eta/\eta_u$ is similar to that of $\eta(x_R, V_{d1})$. Since the voltage utilization is always high, the behavior of the thrust function $F(x_R, V_{d1})$, Fig. 4(e), is similar to that of $\eta_u$. More

outward electrode positions yield larger values of $F$, but larger values of $P_d$ too, Fig. 4(f). To maximize the thrust and minimize the discharge power, the inner-stage voltage must be in the interval $V_{d1} \sim 120 - 150$ V.

The common two-stage design, which places the intermediate electrode between the ionization and acceleration regions and applies a low inner-stage voltage [1], would correspond here to $V_{d1} \sim 20 - 40$V and $x_R \sim x_S$. Figure 5(a)-(e) shows the two-stage performance for $V_{d1} = 30$V when the location of the third electrode varies from $x_R = 10$ mm to 17 mm. As the electrode is placed inwards, the relative emission current increases up to a 20%. This leads to about a 10% increment of the propulsive efficiency, but also to a reduction of both $\eta_u$ and $\eta_{vol}$. As a result of these opposite trends the gain in thrust efficiency is rather modest (from 52% to 54%). Again for this case, the electrode operation as an electron collector (for $x_R > 16$ mm) leads to a decrement of performances; $\eta_u$ and $\eta_{vol}$ increase, in agreement with Ref. [9], but, because of energy losses, $\eta_{prop}$ decreases in a larger proportion.

Fruchtman and Fisch [8] used a simple 1D model of the acceleration region to determine the optimal location and voltage of an intermediate electrode. They found that the maximum efficiency gain of a *generic* two-stage thruster is about a 6% for low $\eta$, and reduces to about a 3% for $\eta = 52\%$. We try to explain next the discrepancy between this 3% and the 19% of gain for the particular thruster treated here. First, their model ignores completely the ionization and backstreaming regions: with our notation, it can be said that they assume $L_{AS} = 0$, $\phi_{AS} = 0$, and $\eta \propto \eta_{cur}$. Second, in order to determine the optimal third electrode conditions they *assume* that $I_{iP}$ and $\bar{\nu}_d$ are independent of $V_{d1}$ and $x_R$, whereas the discharge current $I_d$ is a free parameter. With these simplifications and constraints, the optimal third electrode parameters are

$$\frac{V_{d1}}{V_d} \sim 2\%, \qquad \frac{\{\bar{\nu}_d\}_{SR} L_{SR}}{\{\bar{\nu}_d\}_{SP} L_{SP}} \sim 4.5\%,$$

values that differ largely with ours. In addition, the reverse electron current at the inner-stage, $I_d - I_{iP}$, changes by more than a 300% from the single-stage case to the optimal two-stage case. Our model shows that the changes on the upstream regions and its coupling with the acceleration region cannot be neglected; for instance, the length $L_{AS}$ is neither negligible nor

constant. But the principal point explaining the large discrepancy with Fruchtman-Fisch, lies on the assumptions made on $I_d$ and $\bar{\nu}_d$. Our solutions for the whole channel *do show* that $I_{iP}$ and $I_d$ remain near constant for most third-electrode conditions, whereas $\bar{\nu}_d$ (i.e. $B_{max}$) must be adjusted for each case. As commented before, the fact that $I_d$ remains almost invariant is a consequence of the electron energy balance. Therefore, although the electron temperature is absent from the definition of $\eta_{cur}$ and from Eqs. (32) and (33), the energy balance is essential to solve correctly the problem.

### V. Conclusions

The present model of a two-stage discharge shows that a good electron-emitting electrode inserted in the acceleration region of the chamber enhances the thruster efficiency. The improvement is significant for thrusters where energy losses are dominated by the interaction with the lateral walls, like thrusters with long ceramic chambers (i.e SPT-type) and operating at mid- and high- discharge voltages.

For the mid-power, mid-voltage thruster studied in this paper, the efficiency increases from 52% for single-stage operation, to 62% for best two-stage operation. As important as this increment is that the efficiency can be kept close to its maximum two-stage value for a relatively wide range of positions and voltages of the intermediate electrode. A two-parameter investigation on the influence of the electrode position and voltage on the performance of that specific thruster concludes that (i) the best location is at an intermediate point within the internal acceleration region, and (ii) the optimum first-stage voltage is about 40-50% of the total discharge voltage.

Two-stage designs and models have generally put the emphasis on improving the efficiency of the ion beam, which basically means to improve the propellant and voltage utilizations. On the contrary, our idea has been to depart from a single-stage design with high values of these ionization-related efficiencies and to focus on reducing the electron energy losses to the walls in the acceleration region. It turns out that the insertion of part of the electron reverse current near the ionization region reduces the temperature in the acceleration region

without affecting practically the propellant and voltage utilizations. Maximum efficiency is obtained for a two-stage operation point where the profile of the electron temperature is rather flat and the temperature peak is near its minimum value, thus minimizing the zones with charge-saturated sheaths.

Other conclusions of the present study are the following. First, to solve the electron energy equation is essential to determine the thruster performances and thus constitutes a major advance over previous models. Second, the operation at different inner-stage voltages requires to adjust the strength of the magnetic field; to zeroth order, the magnetic strength increases inversely proportional to the electron reverse current in the outer stage. Third, two-stage discharges with low inner-stage voltages do not lead to relevant efficiency increments. And four, an electron-collecting electrode deteriorates the thruster efficiency, at least when the ionization process is already efficient in single-stage operation.

The present paper was aimed to understand the main physical aspects of two-stage discharges and to evaluate the improvements of efficiency. Certainly, several relevant aspects and modelling issues require further studies. First, there is the optimization of the thruster design, beyond determining the optimal position and voltage of the third electrode. In particular, the optimum axial shape of the magnetic field for two-stage operation should be investigated. This could differ from the single-stage one with its pronounced peak at the exit of the chamber, matching the peak of the electric field.

Second, a performance study for the operational range of discharge voltages and mass flows is primordial for two-stage thrusters envisaged for variable thrust operation. Two-stage operation is specifically proposed for the high specific impulse mode, when the mass flow is lowest and the ionization process can become inefficient. For this case, two-stage operation could help to increase $\eta_u$ too.

Third, there are limitations inherent to the 1D model that must be evaluated. In particular, 2D effects related to (i) the inner or outer location of the electrode and (ii) the topography of the magnetic field lines could have a significant impact on the plasma response.

Four, the two-stage model must be extended to intermediate electrodes with non-zero impedance. The extension is simple for the case of low impedance if the current-voltage

characteristic of the electrode is known. But the present model is not directly applicable to low emission and passive electrodes. In this last case, the electron-emission mode is in fact an ion-collection mode and requires to modify the ion conservation equation. The benefits of SPT-type thrusters with a intermediate passive electrode are dubious, since the ion-collection regime seems to imply a reduction of the final ion beam flow.

Five, for the two-stage thrusters discussed here, the efficiency gain is based mainly on the reduction of the wall energy losses. These are very sensitive to the plasma-wall interaction model and the uncertainties of this model are transferred directly to our results. Although the radial model of Ref. [13] provides a plausible and self-consistent physical view of that interaction, it is also known that it tends to overestimate the particle and energy losses [10]. One part of this seems to be due to the 2D ion dynamics but the main part is likely due to the assumption of a quasi-Maxwellian distribution function of primary electrons near the walls. Recent works [16, 17] have suggested a strong distortion of the tail of the electron distribution caused by both magnetic mirroring and incomplete replenishment of collected electrons. The re-collection by the walls of part of the SEE can modify the energy losses too [18]. At present, the consequences of these phenomena on the different terms modelling the wall losses have been quantified only partially. The main issue is that a reduction of the relative weight of wall energy losses will possibly imply a reduction of the maximum efficiency gain obtained from two-stage thrusters.

Finally, attention must be paid to technical aspects that can reduce and even cancel the benefits obtained from the improvement of the plasma performances. These technical issues would include, at least, (i) the power spent to heat the third electrode, (ii) the possible contamination of the chamber walls generated by electrode eroded material [19], (iii) the reduction of lifetime and reliability due to the more complex design and fabrication of the chamber, and (iv) the larger mass of the whole thruster.

# References

[1] H. Kaufman, AIAA Journal **23**, 78 (1985).

[2] D. Jacobson, R. Jankovsky, V. Rawlin, and D. Manzella, High voltage TAL performance, in *37th Joint Propulsion Conference, Salt Lake City, UT*, AIAA-2001-3777, American Institute of Aeronautics and Astronautics,Washington, DC, 2001.

[3] A. Solodukhin, A. Semenkin, S. Tverdokhlebov, and A. Kochergin, Parameters of D-80 anode layer thruster in one- and two-stage operation modes, in *27th International Electric Propulsion Conference, Pasadena, CA, USA*, IEPC-01-032, Electric Rocket Propulsion Society, Cleveland, OH, 2001.

[4] Y. Yamagiwa and K. Kuriki, J. Propulsion and Power **7**, 65 (1991).

[5] N. Fisch, Y. Raitses, L. Dorf, and A. Litvak, J. Applied Physics **89**, 2040 (2001).

[6] B. Pote and R. Tedrake, Performance of a high specific impulse Hall thruster, in *27th International Electric Propulsion Conference, Pasadena, CA, USA*, IEPC-01-035, Electric Rocket Propulsion Society, Cleveland, OH, 2001.

[7] R. Hofer, P. Peterson, A. Gallimore, and R. Jankovsky, A high specific impulse two-stage Hall thruster with plasma lens focusing, in *7th International Electric Propulsion Conference, Pasadena, CA, USA*, IEPC-01-036, Electric Rocket Propulsion Society, Cleveland, OH, 2001.

[8] A. Fruchtman and N. Fisch, Phys. Plasmas **8**, 56 (2001).

[9] A. Fruchtman, N. Fisch, and Y. Raitses, Phys. Plasmas **8**, 1048 (2001).

[10] E. Ahedo, J. Gallardo, and M. Martínez-Sánchez, Physics of Plasmas **10**, 3397 (2003).

[11] G. Janes and R. Lowder, Physics of Fluids **9**, 1115 (1966).

[12] E. Ahedo, J. Gallardo, and M. Martínez-Sánchez, Physics of Plasmas **9**, 4061 (2002).

[13] E. Ahedo, Physics of Plasmas **9**, 4340 (2002).

[14] E. Ahedo and D. Escobar, Journal of Applied Physics **96**, 983 (2004).

[15] E. Ahedo, P. Martínez-Cerezo, and M. Martínez-Sánchez, Physics of Plasmas **8**, 3058 (2001).

[16] N. Meezan and M. Capelli, Physical Review E **66**, 036401 (2002).

[17] K. Sullivan, J. Fox, O. Batischev, and M. Martínez-Sánchez, Kinetic study of wall effects in SPT, in *40th Joint Propulsion Conference, Fort Lauderdale, FL*, AIAA-2004-3777, American Institute of Aeronautics and Astronautics,Washington, DC, 2004.

[18] E. Ahedo and F. I. Parra, Model of radial plasma-wall interactions in a Hall thruster, in *38th Joint Propulsion Conference, Indianapolis, IN*, AIAA 2002-4106, American Institute of Aeronautics and Astronautics,Washington, DC, 2002.

[19] Y. Raitses, D. Staack, and N. Fisch, Plasma characterization of Hall thruster with active and passive segmented electrodes, in *2002 38th Joint Propulsion Conference, Indianapolis, IN*, AIAA-2002-3954, American Institute of Aeronautics and Astronautics,Washington, DC, 2002.

## Figure captions

Figure 1: Sketch of the two-stage discharge model. The anode is at point $A$ (with $x_A = 0$), the thruster exhaust at point $E$, the cathode neutralization surface at point $P$, and the third electrode at point R. The total and inner-stage discharge voltages, $V_d$ and $V_{d1}$, are known, whereas the inner- and outer-stage currents, $I_{d1}$ and $I_{d2}$, are part of the solution; $I_d = I_{d1} + I_{d2}$ is the total discharge current. Points D and S correspond to zero and sonic velocities of the ion flow, and are part of the solution. Point B is the anode-sheath transition. Regions AB, BD, DS, SR, RP correspond to electron-repelling sheath, ion backstreaming region, main ionization layer, inner-stage acceleration region, and outer-stage acceleration region. $\Gamma_{x\alpha} = A n_\alpha v_{x\alpha}, \ \alpha = i, e, \dots$ are axial flows of particles of each of the plasma species.

Figure 2: Evolution of thruster parameters with the inner-stage voltage when the intermediate electrode is placed at $x_R = 14.5$mm. Other input parameters are $L_c = 25$mm, $L_{EP} = 8.5$mm, $A_c = 40$cm$^2$, $V_d = 296$V, $\dot{m} = 4.78$mg/s, $T_{eP} = 4.4$eV, $\alpha_{ano} \simeq 0.0124$, $T_1 \simeq 39.93$eV, $\tilde{\nu}_w \simeq 0.191$. The function $B_{max}(V_{d1})$, in plot (a), is an input too. The dashed vertical line corresponds to single-stage
operation or floating-case of the intermediate electrode.

Figure 3: Axial response for three particular points of Fig. 2: $V_{d1} =$18 V (dashed lines), 137 V (solid lines), and 196 V (dash-and-dot lines). The intermediate electron current are $I_{d1} =$0 A, 1.3 A, and 1.5 A, respectively. The asterisks represent points R, E, and P. Plots (b) and (c) show dimensionless particle flows of ions and electrons, $\eta_\alpha(x) = m_i \Gamma_{x\alpha}(x)/\dot{m}_A, \alpha = i, e$.

Figure 4: Level lines of main parameters characterizing the thruster response, as functions of the third-electrode position and inner-stage voltage, $x_R$ and $V_{d1}$, respectively. The rest of thruster parameters are as in Fig. 2; in particular, $V_d = 296$V, $\dot{m}_A = 4.78$mg/s, and $\alpha_{ano} \simeq 0.0124$. Thick solid lines represent single-stage operation or the floating case of the third electrode. Thick dashed lines correspond to $x_R = x_S$.

Figure 5: Evolution of thruster parameters with the location of the third electrode for $V_{d1} = 30$ V. The rest of thruster parameters are as in Fig. 2. The vertical, dashed line corresponds to single-stage operation, $I_{d1} = 0$.
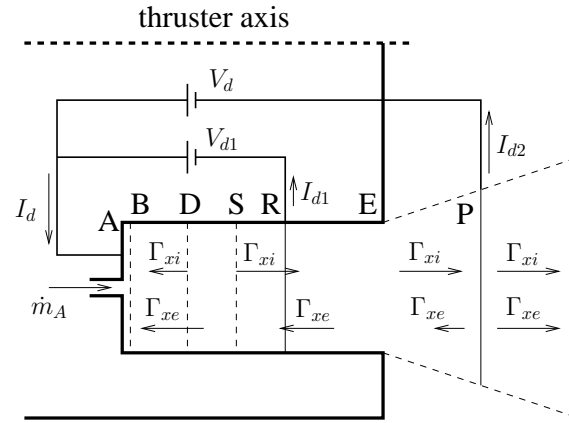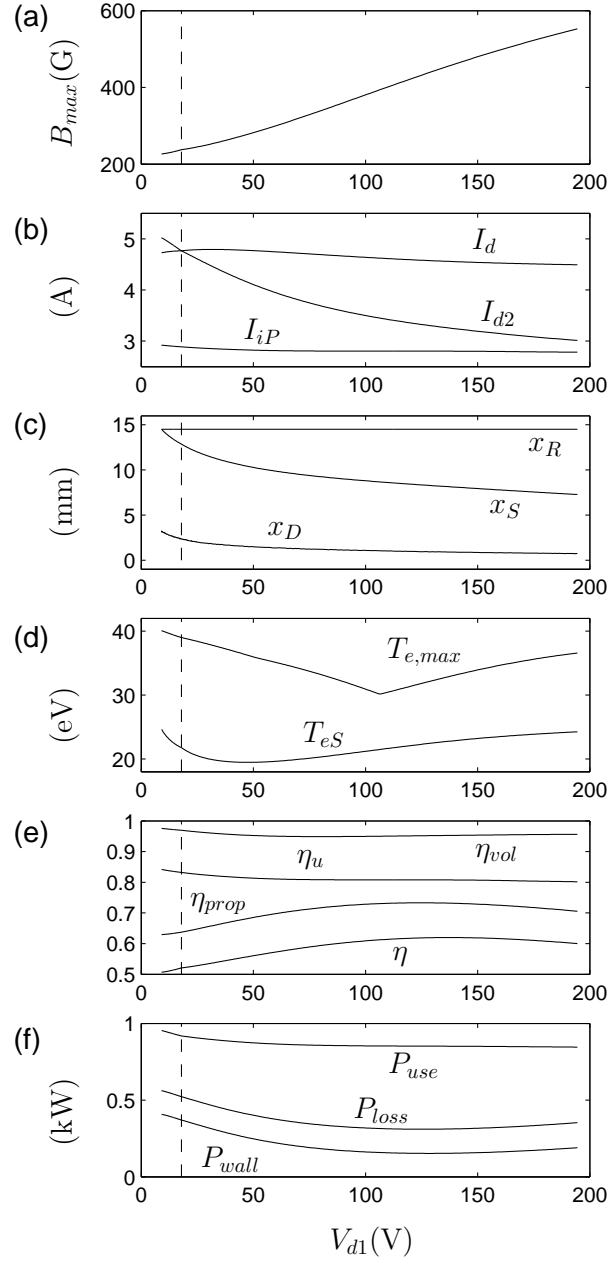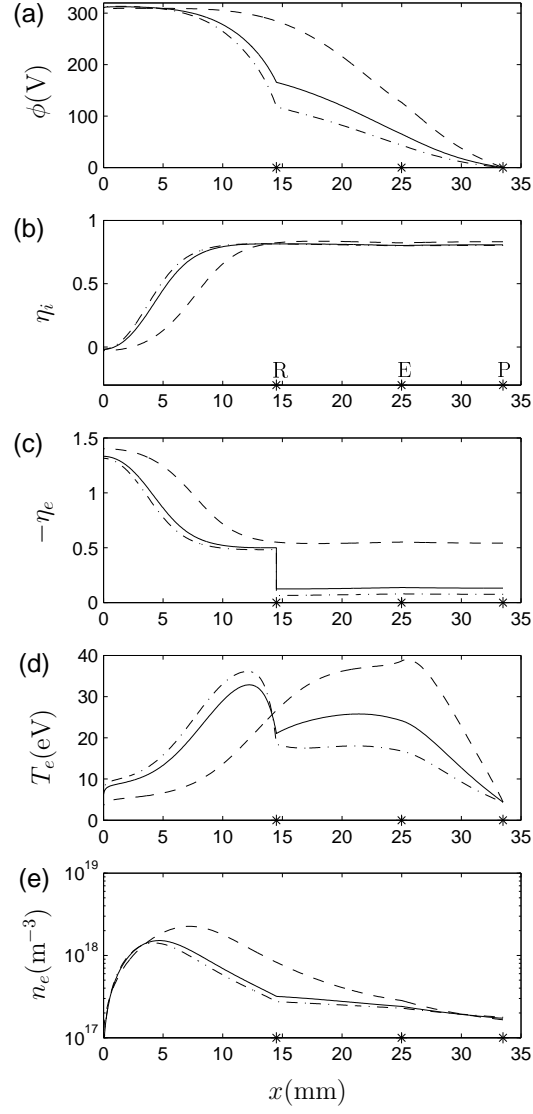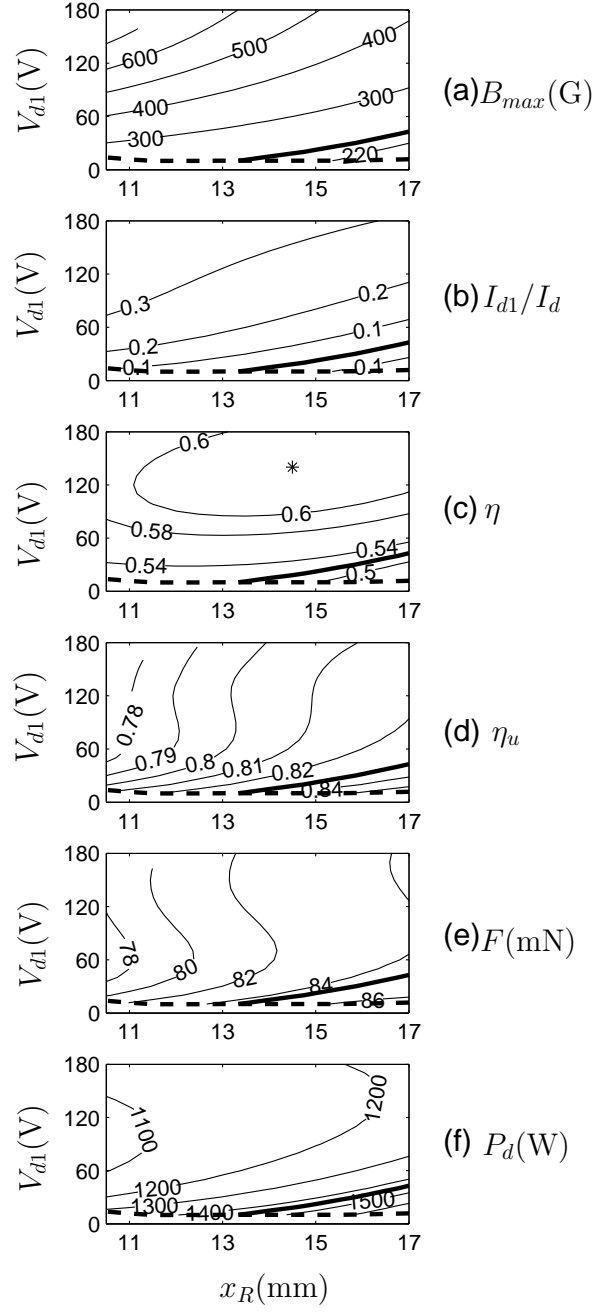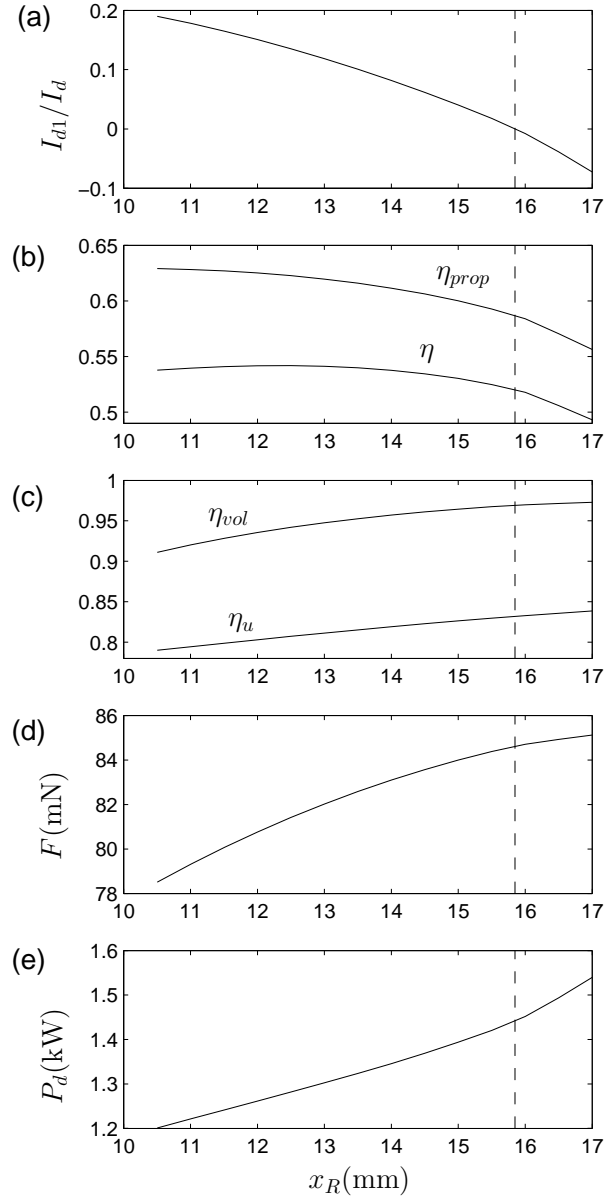
# A NO-ANODE-SHEATH REGIME OF THE HALL THRUSTER DISCHARGE

**Juan Rus and Eduardo Ahedo**

E.T.S.I. Aeronáuticos, Universidad Politécnica de Madrid, Spain

## ABSTRACT

The transition from a negative- to a no-anode-sheath regime of the Hall thruster discharge is analyzed. The no-sheath regime is reached when lowering the discharge voltage. The parameter interval of this regime is very small and the current-voltage curve is not monotonic. Inertia effects on the electron dynamics limit the azimuthal velocity to a value much lower than the diffusive value based on the Hall parameter.

Key words: Hall thruster; modelling; sheaths.

## 1. INTRODUCTION

### 1.1. The normal operation regime

For typical operation conditions of the Hall thruster, the quasi-closed drift, diffusive limit applies to the electron flow moving from the chamber exit towards the anode. In terms of electron velocities this means [Ahedo et al. (2003)]

$$v_{\theta e} \simeq -\frac{\omega_e}{\nu_e} v_{xe}, \qquad |\boldsymbol{v}_e| \simeq v_{\theta e} \ll \bar{c}_e, \qquad (1)$$

where $\bar{c}_e = \sqrt{8 T_e / \pi m_e}$ is the random velocity, $v_{xe}$ and $v_{\theta e}$ are the axial and azimuthal fluid velocities, $\omega_e$ is the electron gyrofrequency, and $\nu_e$ is the total collision frequency (which includes contributions from collisions with neutrals and ions, wall collisionality, and Bohm diffusion).

In order that, in steady-state operation, the electron current collected at the anode coincides with the small diffusive current of the quasineutral discharge a negative-potential sheath is formed around the anode of the thruster [Fig. 1]. Applying typical Maxwell-Boltzmann conditions across that sheath and the conservation of the electron current, the self-adjusted potential drop in the sheath, $\phi_{AB}$, satisfies

$$\exp \frac{-e\phi_{AB}}{T_{eB}} = \frac{n_{eA}}{n_{eB}} = \frac{-v_{xeB}}{\bar{c}_e/4}, \qquad (2)$$

where points A and B refer to the anode and the sheath/presheath transition.

Clearly the electric field in the quasineutral region next to the anode sheath has the same sign than the electric field inside the Debye sheath, and thus accelerates the ions towards the anode. Therefore, the existence of a negative sheath implies the formation of an ion back-streaming region [BD in Fig. 1], separating the anode from the main ionization layer (DS). As it is well known, the sheath/presheath transition is defined by the Bohm sonic condition for the velocity of the attracted species (i.e. ions); for $T_i \ll T_e$ the Bohm condition reads

$$v_{xiB} = -\sqrt{\frac{T_{eB}}{m_i}}. \qquad (3)$$

From Eqs. (2) and (3), the sheath potential drop depends directly on the ion backstream-

ing current:

$$\frac{e\phi_{AB}}{T_{eB}} = \ln\left(\sqrt{\frac{m_i}{2\pi m_e}}\,\frac{|I_{iB}|}{I_d + |I_{iB}|}\right), \qquad (4)$$

with $I_d = I_i(x) - I_e(x)$ the discharge current, $I_\alpha = e n_e v_{x\alpha} A_c$ ($\alpha = i, e$) the species current (with $I_e$ negative and $I_i$ changing sign at point D), and $A_c$ the chamber cross-section area. For good thruster operation one expects $I_{iB}/I_d$ to be small (less than 10%, say), so that $I_{eB} \sim -I_d$.

The existence of the ion-backstreaming region and the anode sheath has been reported experimentally by Bishaev & Kim (1978) and is well documented in recent review papers [Kim (1998); Zhurin et al. (1999)]. The models of the whole discharge of Fife (1998) and Ahedo et al. (1998, 2002) include these two regions.

## 1.2. The vanishing of the negative sheath

From Eq. (4), the sheath vanishes when the relative ion backcurrent is

$$\frac{|I_{iB}|}{I_d} = \sqrt{\frac{2\pi m_e}{m_i}}; \qquad (5)$$

for xenon, this means $-I_{iB}/I_d \simeq 0.5\%$. In terms of parameters governing the whole discharge, Ahedo et al. showed that $-I_{iB}/I_d$ decreases when the discharge voltage, $V_d$, decreases or the strength of the radial magnetic field, $B_{max}$, increases [see Figs. 5 and 7 of Ahedo et al. (2000) and Fig. 6 of Ahedo et al. (2002)]. The same trends were obtained posteriorly by Cohen-Zur et al. (2002). Therefore, these models conclude that the no sheath limit is reached for *low* values of $V_d$.

Ahedo et al. limited their study to the negative sheath regime. On the one hand, the negative sheath regime seems to correspond to normal (and optimal) operation conditions of the thruster; according to Zhurin et al., solutions with no negative sheath present an extra source of inefficiency (i.e. the electron acceleration towards the anode) and can result in the discharge easily becoming extinguished. On the other hand, the diffusive model of the electrons fails when the no sheath limit (NSL)
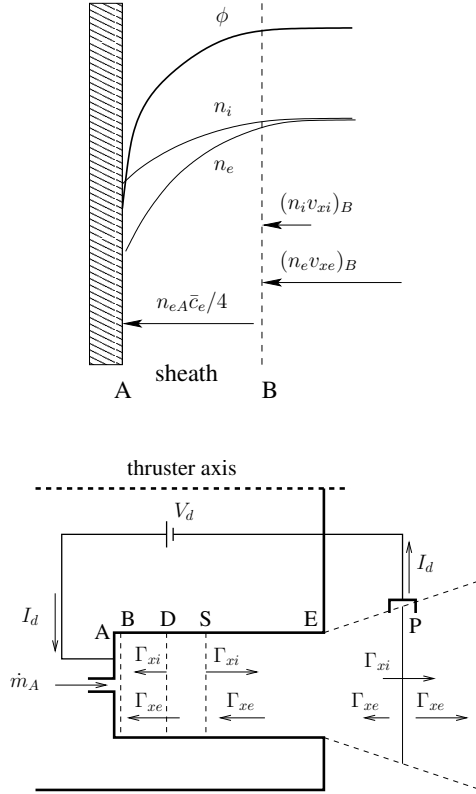


Figure 1. *(Top) The anode sheath. (Bottom) Sketch of the whole discharge model. The anode is at point A (with $x_A = 0$), the thruster exhaust at point E, and the cathode neutralization surface at point P, Points D and S correspond to zero and sonic velocities of the ion flow, and are part of the solution. Point B is the anode-sheath transition. Regions AB, BD, DS, SP correspond to electron-repelling sheath, ion backstreaming region, main ionization layer, and acceleration region. $\Gamma_{x\alpha} = A n_\alpha v_{x\alpha}$, $\alpha = i, e, ...$ are axial flows of particles of each of the plasma species.*

is approached [Ahedo et al. (2001)]. According to Eqs. (1) and (2), at the NSL one has

$$-v_{xeB} \simeq 0.4\sqrt{\frac{T_{eB}}{m_e}}, \quad v_{\theta eB} \simeq -v_{xeB}\frac{\omega_{eB}}{\nu_{eB}}. \tag{6}$$

Although the Hall parameter at the anodic end of the chamber, $(\omega_e/\nu_e)_B$, differs much for different Hall thrusters, in most cases it is still large. As a consequence, the electron directed energy in the near anode zone, $(m_e/2)(v_{xe}^2+v_{\theta e}^2)$, is of the order or even larger than the thermal energy, $T_e$. Ahedo et al. (2002) pointed out the relevance of inertial effects on the electron dynamics in such situation.

### 1.3. A no sheath regime

Dorf et al. (2002) have been the first to study the transition from the negative-sheath regime to a no-sheath regime. They assert that the two regimes differ only on the boundary conditions at the anode. For the no-sheath regime, Eq. (3) must be substituted by

$$v_{xeB} = -\sqrt{\frac{T_{eB}}{2\pi m_e}} \tag{7}$$

[that is, Eq. (2) with $\phi_{AB} = 0$] and expect to find $0 < -v_{xiB} < \sqrt{T_{eB}/m_i}$. (For convenience we will keep naming point B to the end point of the quasineutral model, even when it coincides with point A).

Dorf et al. analyze the regime transition applying these boundary conditions into a simple model of the discharge, which considers the temperature profile as an *input* of the model and *invariant* for all operation points analyzed. Also, they use the electron diffusive model with no discussion on inertial effects. Contrary to the results of Ahedo et al. they find that the no sheath regime corresponds to *high* values of $V_d$. The same trend is found in a second paper [Dorf et al. (2003)], which differs from the first one on the magnetic field strength and the electron dynamics near the anode.

The goals of this paper are twofold. First, to formulate a valid model for the electron dy-

namics in the near anode region when inertial effects must be taken into consideration. Second, to extend the model of Ahedo et al. (where the computation of the temperature profile is a relevant part) to the no sheath regime, using the boundary conditions proposed by Dorf et al..

### 2. INERTIAL EFFECTS ON THE ELECTRON AZIMUTHAL VELOCITY

When $v_{\theta e} \gg |v_{xe}|$, Ahedo et al. (2002) showed that inertia effects affects mainly the azimuthal velocity and proposed the following momentum equations [used by Barral et al. (2003) too]:

$$0 = -\frac{1}{n_e}\frac{d}{dx}n_e T_e + e\frac{d\phi}{dx} + m_e \omega_e v_{\theta e}, \tag{8}$$

$$v_{xe}\frac{dv_{\theta e}}{dx} = -\nu_e v_{\theta e} - v_{xe}\omega_e. \tag{9}$$

The diffusive limit corresponds to take zero the left-hand side of the last equation. The axial discharge model of Ahedo et al. completes these two equations with seven more, which determine the nine plasma variables: $n_e$, $v_{xe}$, $v_{\theta e}$, $T_e$, $q_{xe}$, $v_{xi}$, $n_n$, $v_{xn}$, and $\phi$.

A correct numerical integration of Eq. (9) must avoid exponentially-divergent modes and thus requires to proceed along the direction of the electron motion, that is from cathode P to anode A in Fig. 1. However, this is not feasible for the set of nine equations, due to other mathematical constraints of the system. Indeed, the integration carried out in Ahedo et al. (2002) (with $v_{\theta e}$ diffusive) is divided in three parts (from the sonic point S to P, from point S towards point B, and from point B towards S) and a posterior iteration is needed to adjust the spatial profiles of the three parts and the desired thruster parameters.

Therefore, if inertia effects want to be considered, we must solve an approximate set of equations. he following procedure is proposed:

1. To avoid Eq. (9) and to use instead an approximate equation for $v_{\theta e}$ which could
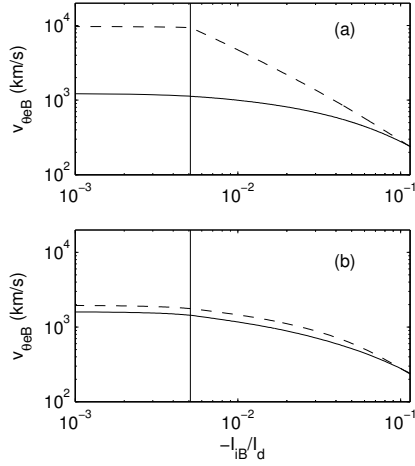
*Figure 2. Comparison between approximate (dashed) and correct (solid) solutions of $v_{\theta eB}$ for the (a) diffusive and (b) the inertia/diffusive models, Eqs.(10) and (11), respectively. The vertical line marks the no sheath limit. Thruster parameters corresponds to a SPT-100 and are similar to those used in Case 2 of Ahedo et al. (2003)]*

be integrated with the rest of plasma equations with the mentioned 3-part integration

2. To compute $v_{\theta e}(x)$ in a post-process from Eq. (9) and to compare with the approximate solution, $v'_{\theta e}$, obtained before.

Two different approximate models of the azimuthal velocity were tested. The first one was just the diffusive model,

$$v'_{\theta e} = -v_{xe}\frac{\omega_e}{\nu_e}. \qquad (10)$$

Figure 2(a) compares the 'diffusive' and 'correct' values of $v_{\theta e}$ at the anode sheath transition (where differences are largest) for typical parameters of a SPT-100 thruster. The differences become significant for $-I_{iB}/I_d < .05$. At the no-sheath limit, the diffusive approximation overestimates the azimuthal velocity by nine times. Therefore, a better model of $v_{\theta e}$ is needed in order to study correctly no sheath solutions.

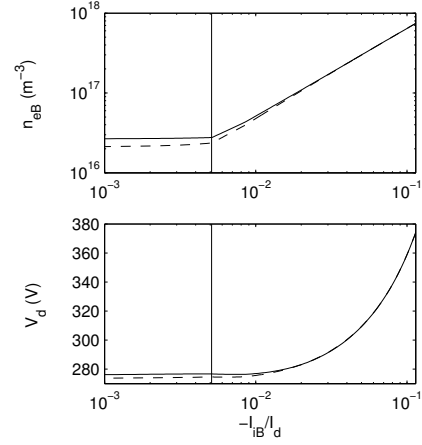The second approximate model of the azimuthal velocity is a mixed inertial/diffusive



*Figure 3. Discharge voltage and plasma density at the anode sheath transition when the diffusive (dashed) and the inertia/diffusive (solid) models for $v_{\theta e}$ are used. The vertical line marks the no sheath limit. Rest of parameters as in Fig. 2.*

one, where inertial effects are assumed to matter only in the near anode region. The equations we use are

$$v'_{\theta e} = \begin{cases} v'_{\theta e,0} + v'_{\theta e,1} & \text{for} \quad x < x_t \\ -v_{xe}\dfrac{\omega_e}{\nu_e} & \text{for} \quad x > x_t \end{cases} \qquad (11)$$

with $v'_{\theta e,0}$ and $v'_{\theta e,1}$ the solutions of

$$\frac{dv'_{\theta e,0}}{dx} = -\omega_e, \qquad (12)$$

$$\frac{dv'_{\theta e,1}}{dx} = -v'_{\theta e,0}\frac{\nu_e}{v_{xe}}, \qquad (13)$$

and $x_t$ a convenient point to match the two types of solutions in Eq. (11). Figure 2(b) shows that this second model gives reasonable approximations of $v_{\theta eB}$; errors are less than a 20% (again differences are largest at the plotted point B).

Figure 3 compares the values of $V_d(I_{iB})$ and $n_{eB}(I_{iB})$ for the two approximate models of the azimuthal velocity. In spite that $v_{\theta e}$ is overestimated up to one order of magnitude when using the diffusive model, this does not produce significant errors on the rest of the plasma variables. The reason is that inertial effects, although large, are very localized near
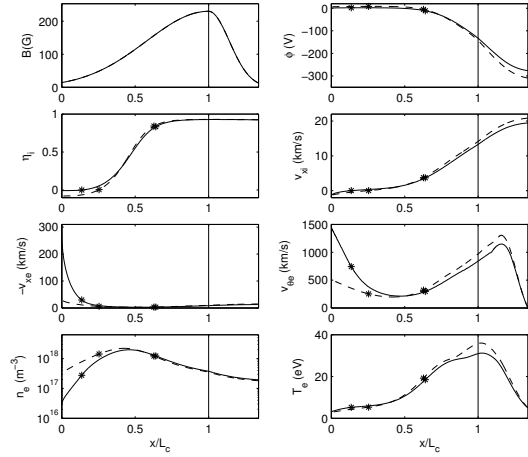
*Figure 4. Negative-sheath regime. Axial profiles of plasma variables for $-I_{iB}/I_d = 5 \times 10^{-2}$ (dashed lines) and $5 \times 10^{-3}$ (solid lines; no sheath limit) The vertical line marks the channel exit. Rest of parameters as in Fig. 2.*

the anode. In any case, a good-enough solution of $v_{\theta e}$ is needed to evaluate correctly the electron energy deposited at the anode, which is equal to

$$P_{anode,e} = A_c(n_e v_{xe})_B[2T_e + \frac{1}{2}m_e(v_{\theta e}^2 + v_{xe}^2)]_B. \quad (14)$$

A final observation is that the above inertia/diffusive model has been validated for cases where $(\omega_e/\nu_e)_B$ is large. For thrusters [or models, such as Dorf et al. (2003)] with $(\omega_e/\nu_e)_B \ll 1$, inertial effects on $v_{\theta e}$ can be important far from the anode (in the region where $\omega_e/\nu_e$ is about one and presents a large spatial gradient) and, in addition, inertial effects on $v_{xe}$ must be considered near the anode.

## 3. COMPARISON OF THE NEGATIVE- AND NO-SHEATH REGIMES

Figures 4 and 5 show axial profiles of the main plasma variables for a negative-sheath solution, the no sheath limit, and the zero ion backstreaming limit. The discharge voltage is the parameter defining the different
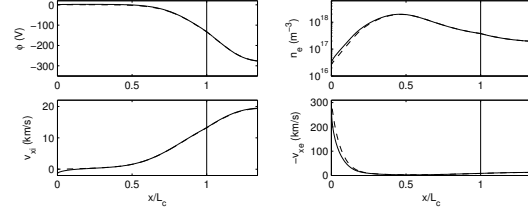


*Figure 5. No-sheath regime. Axial profiles of plasma variables for $-I_{iB}/I_d = 5 \times 10^{-3}$ (solid lines; no sheath limit) and 0 (solid lines; zero ion backcurrent limit). The vertical line marks the channel exit. Rest of parameters as in Fig. 2.*

cases, whereas the rest of control parameters remained unchanged; in particular, the magnetic field strength is constant ($B_{max} \simeq 230$ G). The inertial/diffusive model of the azimuthal velocity has been used in the computations. The spatial profiles show the following. First, the NSL is reached for low values of $V_d$. Second, the temperature profile and, in particular, its peak, $T_{e,max}$, do not remain constant. And third, the parametric interval for the no sheath regime is very narrow.

Figure 6 shows the evolution of the main plasma parameters between the limit cases depicted in Figs. 4 and 5. Although $I_{iB}$ is plotted as the abcissa, the real control parameter is $V_d$. We observe, first, that the no-sheath regime corresponds to a practically constant (and low) value of $V_d$, which means that this regime is ill-defined in terms of that parameter; in fact $V_d(I_{iB})$ is not monotonic there. Second, the variation of the peak electron temperature with $V_d$ is natural: it is due to the Joule heating in the acceleration regime, which is almost proportional to $V_d$. The plots show that variations are relatively large: $\partial \ln T_{e,max}/\partial \ln V_d > 2$ for most of the negative sheath regime. This feature is surely marking the difference with the results Dorf et al., who treat $T_e(x)$ as an invariant input to their model. Third, point D of zero ion velocity moves towards the anode (as $I_{iB}$ decreases), but point S and the acceleration region remain invariant. Thus, the extension of the ionization region spreads towards the anode, which explains the decrease of

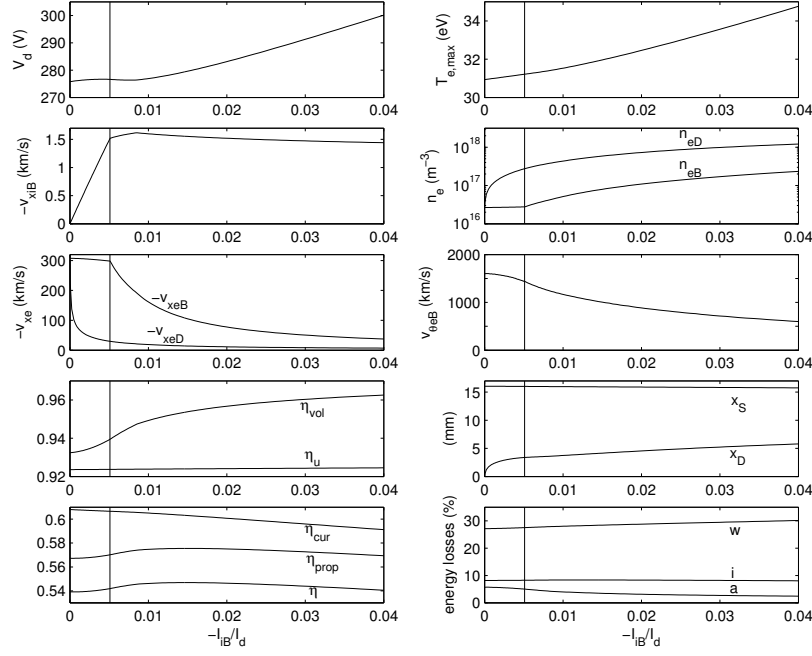$$\eta_{vol} = \dot{m}_{i\infty}v_{xi\infty}^2/2eV_d.$$

*Figure 6. Evolution of main plasma parameters with the ion-reverse current at the anode. Rest of parameters as in Fig. 2. The vertical line marks the no sheath limit. In the last plot 'w', 'i', and 'a' mean wall, ionization and anode losses, respectively.*

The propellant utilization, $\eta_u = \dot{m}_{i\infty}/\dot{m}_A$, depends on the production/recombination equilibrium on the acceleration region, which justifies that it remains almost constant with $I_{iB}$. The mild changes on $v_{xiB}$ and of $v_{xeB}$ within the negative- and no-sheath regimes, respectively, are due to $T_{eB}$, which lies between 3 and 5eV. One has

$$n_{eB}, v_{xeB}^{-1} \propto |I_{iB}|, \qquad (15)$$

for the negative sheath regime, and

$$n_{eB} \sim \text{const}, \qquad v_{xiB} \propto |I_{iB}|, \qquad (16)$$

for the no sheath regime. Whereas $v_{xeB}$ increase by one order of magnitude, the increment of $v_{\theta e}(I_{iB})$ is only 2.5 times because of the limitation due to inertia. One has

$$\frac{m_e v_{\theta eB}^2/2}{2T_{eB}} \sim 0.7 - 0.9 \qquad (17)$$

in the no-sheath regime. This implies that the increase of the anode energy losses when moving into the no-sheath regime is moderate,

and anode losses continue to be a secondary contribution to the total energy losses. Wall losses decrease with $V_d$ because of the evolution of $T_{e,max}(V_d)$. The opposite tendencies of the wall and anode energy losses explain the maximum of both the propulsive efficiency,

$$\eta_{prop}(I_{iB}) \equiv P_{use}/P_d$$

and the thrust efficiency,

$$\eta \equiv F^2/2\dot{m}_A P_d \simeq \eta_u \eta_{prop}$$

[see Ahedo & Escobar (2004) for the efficiency definitions and relationships].

Figure 7 plots the discharge current and the efficiency versus the discharge voltage for the same cases than Fig. 6; note that the magnetic field profile is invariant, with a maximum field strength, $B_{max}$, of 230G. This figure emphasizes that (i) the operation point of maximum efficiency is within the negative sheath regime, and (ii) the no sheath regime is bad defined in terms of $V_d$. The most interesting observation with respect to the current-voltage (C-V) curve is whether the regime transition of
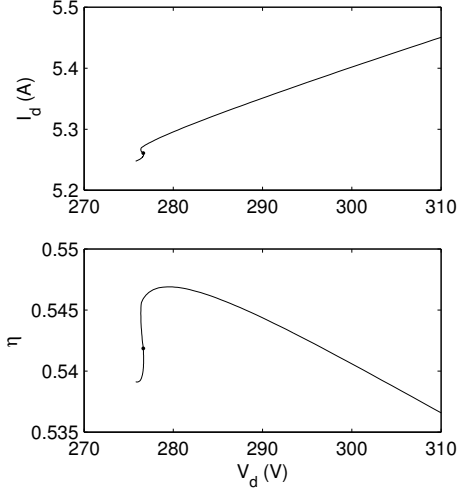
*Figure 7. Current-voltage and efficiency-voltage curves for the case of Fig. 6 ($B_{max} = 230$ G). The dot in the curves correspond to the regime transition.*
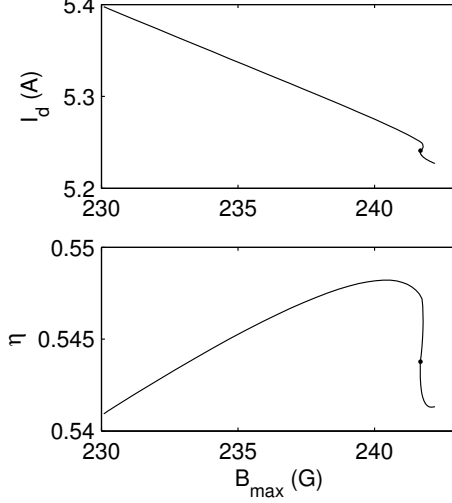


*Figure 8. Discharge current and efficiency versus the magnetic field strength for $V_d = 300$ V. Rest of parameters as in Fig. 6. The dot in the curves correspond to the regime transition.*

our model is related to the classical knee observed in experimental C-V curves around the transition between the low and high efficiency regimes, represented by $d \ln I_d / d \ln V_d \gg 1$ and $\ll 1$, respectively [Morozov et al. (1972); Kaufman (1985)]. Were this hypothesis true, the non-monotonicity of $V_d(I_d)$ and the low plasma density near the anode, $n_{eB}$, for the no sheath regime would be related to the fluctuating response and the discharge extinguishion observed in the low efficiency regime.

The transition from negative- to no-sheath regimes can also be achieved by keeping constant the discharge voltage and varying the magnetic field strength, $B_{max}$. Figure 8 illustrates this situation. Following the format of Fig. 7, we have plotted the discharge current and the efficiency versus $B_{max}$ for $V_d = \text{const} = 300$ V. The negative sheath decreases with $B_{max}$ increasing, and the no-sheath regime corresponds to high values of $B_{max}$. As in the previous investigation with $V_d$, maximum efficiency takes place within the negative-sheath regime and the no-sheath regime is narrow and bad-defined in terms of $B_{max}$. Adding to this last fact that the discharge current, $I_d$, decreases with $B_{max}$,

we venture a correspondence between these responses and the experimental ones, where $I_d$ decreases with $B_{max}$ until a certain (optimum) value of $B_{max}$ is reached, when a strong fluctuating response appears [Kim (1998)].

## 4.  CONCLUSIONS

The analysis of the no sheath regime requires, first, to consider inertial effects on the electron dynamics. The electron inertia reduces largely the ratio between the azimuthal and axial velocities and, as a consequence, the increase of energy losses at the anode.

The no sheath regime is confirmed to correspond to low discharge voltages (and high magnetic field strengths). This disagreement with the results of Dorf et al. is explained by the temperature profile, which cannot be assumed to be invariant with the discharge voltage. [This is one more example of the central role played by the electron distribution function and the energy balance in the Hall thruster response.]

The no sheath regime is small and bad defined in terms of control parameters. Results suggest a possible correspondence between these theoretical results around the no sheath limit and extended experimental observations about (i) the presence of strong fluctuations, (i) the transition to the low efficiency regime, and (ii) the existence of an optimum magnetic field.

Since this last subject merits more attention and the present no sheath regime is too narrow to extract reliable conclusions, work is in progress to extend the present no sheath regime into a second no-sheath regime (with $v_{xiB} = 0$ and $-v_{xeB} > \bar{c}_e/4$) and a positive sheath regime (with $-v_{xeB} = \sqrt{T_e/m_e}$, possibly).

## ACKNOWLEDGMENTS

## REFERENCES

Ahedo E., Escobar D., 2004, Journal of Applied Physics (in press)

Ahedo E., Martínez-Cerezo P., Martínez-Sánchez M., 2000, In: SP-465: 3rd Spacecraft Propulsion Conference, Cannes (Francia), 323–330, European Space Agency, Noordwijk, The Netherlands

Ahedo E., Martínez-Cerezo P., Martínez-Sánchez M., 2001, Physics of Plasmas, 8, 3058

Ahedo E., Gallardo J., Martínez-Sánchez M., 2002, Physics of Plasmas, 9, 4061

Ahedo E., Gallardo J., Martínez-Sánchez M., 2003, Physics of Plasmas, 10, 3397

Barral S., Makowski K., Peradzynski Z., Gascon N., Dudeck M., 2003, Phys. Plasmas, 10, 4137

Bishaev A., Kim V., 1978, Sov. Physics-Tech. Physics, 23, 1055

Cohen-Zur A., Fruchtman A., Ashkenazy J., Gany A., 2002, Physics of Plasmas, 9, 4363

Dorf L., Semenov V., Raitses Y., Fisch N., 2002, In: 38th Joint Propulsion Conference, Indianapolis, IN, AIAA 2002-4246, American Institute of Aeronautics and Astronautics,Washington, DC

Dorf L., Semenov V., Raitses Y., 2003, Applied Physics Letters, 83, 2551

Fife J.M., 1998, Hybrid-PIC Modeling and Electrostatic Probe Survey of Hall Thrusters, Ph.D. thesis, Massachusetts Institute of Technology

Kaufman H., 1985, AIAA Journal, 23, 78

Kim V., 1998, J. Propulsion Power, 14, 736

Morozov A., Esipchuk Y., Tilinin G., et al., 1972, Soviet Physics-Tech. Physics, 17, 38

Zhurin V., Kaufman H., Robinson R., 1999, Plasma Sources Sci. Technol., 8, R1

# On the near-anode region of the Hall thruster discharge

E. Ahedo

*E.T.S.I. Aeronáuticos, Universidad Politécnica de Madrid, Spain*

## Abstract

In the normal response of a Hall thruster discharge, a negative potential sheath is formed at the anode. It is found that the classical negative-sheath model starts to fail when the electron axial velocity becomes of the order of the thermal velocity. A new presheath/sheath model, which takes into account all inertial terms in the electron dynamics, is developed. The model yields the continuous transition negative to positive sheath potential regimes. The general expression of the Bohm condition, which defines the sheath transition, involves the temperatures and the axial velocities of both ions and electrons. There does not exist a no sheath regime, as assumed in recent papers.

## 1 Introduction

Dorf et al.[1, 2] have been the first to study the transition from negative- to no- sheath regimes around the anode of the Hall thruster discharge. For the no sheath regime they propose a single modification of the classical boundary conditions used in the negative-sheath regime. Their analysis is supported on a simplified model of the discharge, which considers the temperature profile along the chamber as an *input* of the model and *invariant* for all operation points analyzed. In addition, the classical electron *diffusive* model is used in both regimes. Their model yields that the no sheath regime corresponds to *high* values of the discharge voltage, $V_d$ (for the rest of parameters fixed).

Ahedo and co-workers have studied the negative sheath regime up to the no-sheath limit, with models that compute, for each $V_d$, the temperature profile as part of the solution [3, 4, 5]. They find that (a) the no-sheath limit is reached for *low* values of the discharge voltage, and (b) *inertial effects* on the electron dynamics become relevant near the anode before the no-sheath limit is reached.

In order to revise the discrepancies between the two models, Rus and Ahedo [6] have carried out an analysis of the regime transition proposed by Dorf et al., departing from the model of Ahedo et al. [5] and including partial inertial effects on the

electron equations. Their main conclusions are the following.

1. For the no-sheath regime, inertial effects strongly bound the azimuthal velocity to values of the order of the electron thermal velocity. As a consequence, the electron azimuthal-to-axial velocity ratio near the anode is typically one order of magnitude lower than the Hall parameter value used in the diffusive model.

2. The transition to the no-sheath regime is reached for low values of the discharge voltage (also, for high values of the magnetic field strength, $B_{max}$).

3. The temperature profile and, in particular, the peak temperature do not remain constant with $V_d$. This difference on the treatment of the temperature explains the discrepant results of Dorf et al..

4. The maximum thruster efficiency is reached within the negative-sheath regime. The decrease of efficiency within the no-sheath regime is due to the larger electron energy losses at the anode.

5. The parametric region of the no-sheath regime is small and ill-defined, as Figs. 6 to 8 of Ref. [6] illustrate. Multiple solutions can be obtained for the same $V_d$.

6. The multiplicity of solutions for the no-sheath regime, and the change of trend of the discharge current, $I_d$, with $V_d$ and $B_{max}$ around
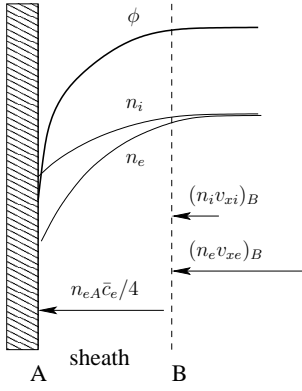
Figure 1: The negative anode sheath.

the no sheath limit, could be related with well reported experimental observations, like the existence of an optimum B-field, the transition to a low ionization regime, and the increase of discharge fluctuations.

Together with a more complete understanding and simulation of the physical processes of the discharge, our interest on the no-sheath regime is on the confirmation of these last conjectures. In order to achieve it, the no-sheath regime should be continued parametrically into a no ion-backcurrent regime and, then, into a positive-sheath regime. Preliminary studies of these regimes have unveiled new aspects of the plasma behavior near the anode, which are at the origin of this paper.

## 2    Classical anode region model

A detailed exposition of the classical treatment of the near anode region was presented by Rus and Ahedo.

For typical operation conditions, the quasi-closed drift, diffusive limit applies to the electron flow moving from the chamber exit towards the anode. In terms of electron velocities this means

$$|\boldsymbol{v}_e| \simeq v_{\theta e} \ll \bar{c}_e, \qquad (1)$$

$$v_{\theta e} \simeq -\frac{\omega_e}{\nu_e} v_{xe}, \qquad (2)$$

where $\bar{c}_e = \sqrt{8T_e/\pi m_e}$ is the random velocity, $v_{xe}$ and $v_{\theta e}$ are the axial and azimuthal macroscopic velocities, $\omega_e$ is the electron gyrofrequency, and $\nu_e$ is the electron total collision frequency. In order that the electron current collected at the anode coincides with the small diffusive current of the quasineutral discharge, a negative-potential sheath is formed around the anode, Fig. 1. Assuming a

quasi-Maxwellian electron population in the anode vicinity, the potential drop, $\phi_{AB}$, in that sheath satisfies

$$\exp \frac{-e\phi_{AB}}{T_{eB}} = \frac{n_{eA}}{n_{eB}} = \frac{-v_{xeB}}{\bar{c}_e/4}, \qquad (3)$$

where points A and B refer to the anode and the sheath/presheath transition. The transition from the quasineutral plasma to the sheath requires that the velocity of the attracted species (the ions, in this case) satisfy the Bohm condition

$$v_{xiB} = -\sqrt{\frac{T_{eB}}{m_i}} \qquad (4)$$

(in this section the usual simplification $T_{iB} \ll T_{eB}$ is applied). From Eqs. (3) and (4), the sheath potential depends directly on the ion backstreaming current:

$$\frac{e\phi_{AB}}{T_{eB}} = \frac{1}{2} \ln \left( \frac{m_i}{2\pi m_e} \frac{I_{iB}^2}{(I_d - I_{iB})^2} \right), \qquad (5)$$

with $I_d = I_i(x) - I_e(x)$ the discharge current, $I_\alpha = en_e v_{x\alpha} A_c$ ($\alpha = i, e$) the species current (both negative near the anode), and $A_c$ the chamber cross-section area.

From Eqs. (3) and (5) the sheath vanishes (i.e. $\phi_{AB} = 0$) when the axial electron velocity and the relative ion backcurrent satisfy

$$-v_{xeB} = \sqrt{\frac{T_{eB}}{2\pi m_e}}, \qquad (6)$$

$$\frac{|I_{iB}|}{I_d} = \sqrt{\frac{2\pi m_e}{m_i}}; \qquad (7)$$

for xenon, this happens at $-I_{iB}/I_d \simeq 0.5\%$.

Dorf et al. propose to continue beyond the no-sheath limit with a no-sheath regime, where Eq. (6) is used as anode condition instead of Eq. (4). The rest of the discharge boundary conditions would be unaffected and they expect

$$0 < -v_{xiB} < \sqrt{\frac{T_{eB}}{m_i}} \qquad (8)$$

to be satisfied. (For convenience we will keep naming point B to the end point of the quasineutral model, even when it coincides with point A).

The no-sheath regime of Dorf et al. finishes when $v_{xiB} = 0$ and the ion backstreaming region disappears. Were that regime correct, its natural parametric continuation would be a *second no-sheath regime* with

$$v_{xiB} = 0, \qquad \sqrt{\frac{T_{eB}}{2\pi m_e}} < -v_{xeB} < \sqrt{\frac{T_{eB}}{m_e}}, \qquad (9)$$

2

followed by a *positive sheath regime* with

$$-v_{xeB} = \sqrt{\frac{T_{eB}}{m_e}} \qquad (10)$$

(and a free plasma parameter to be identified). These boundary conditions make evident that some effects neglected heretofore are indeed relevant and should be included in the plasma equations. The subjects to be revised are:

1. The computation of the potential drop in Eq. (3) is based on an electron population with a small axial drift, and thus must be modified for $v_{xe} \sim \bar{c}_e$.

2. Inertial effects on the electron dynamics were disregarded totally by Dorf et al., and considered only for $v_{\theta e}$ by Rus and Ahedo. When $v_{xe} \sim \bar{c}_e$ and, certainly, for a positive sheath regime, inertia affects the evolution of $v_{xe}$ too. Indeed, condition (10) is obtained from the electron equations only if inertia on $v_{xe}$ is considered.

3. The electric field near the sheath is proportional to the temperature of the repelled species. Thus, for a positive sheath, with $v_{xiB} \simeq 0$, the ion temperature, $T_i$, although small compared to $T_e$, is fundamental.

## 3 New anode region model

In order to evaluate the relevance of the above considerations, a more general model of the region around the anode is analyzed. The model consists of sheath and presheath/quasineutral submodels. Only central aspects of this model have been studied already.

### 3.1 Sheath model

The analysis here is limited to the computation of the sheath potential drop. Let us consider the negative-sheath case, with the electrons as the repelled species. The electron distribution function at the sheath transition point B is assumed to be a drifted-Maxwellian,

$$f_e(\boldsymbol{w}) = n_{eB}\left(\frac{m_e}{2\pi T_{eB}}\right)^{3/2} \exp\frac{m_e(\boldsymbol{w}-\boldsymbol{v}_{eB})^2}{-2T_{eB}} \quad (11)$$

with $\boldsymbol{v}_{eB} = v_{xeB}\mathbf{1}_x + v_{\theta eB}\mathbf{1}_\theta$ the macroscopic drift velocity and $\boldsymbol{w}$ the particle velocity. For a given potential drop $\phi_{AB}$, the integration on $\boldsymbol{w}$ of the
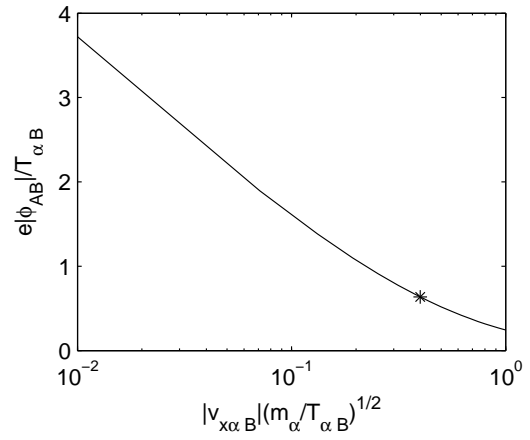


Figure 2: Sheath potential drop versus the perpendicular macroscopic velocity of the repelled species (called $\alpha$). The asterisk represents the case $|v_{xeB}| = \bar{c}_{eB}/4$.

differential axial particle flux yields

$$|g_{xeA}| = n_{eB}\sqrt{\frac{T_{eB}}{2\pi m_e}}\exp(-u^2) + n_{eB}|v_{xeB}|\frac{\text{erfc}u}{2}, \quad (12)$$

as the particle flux collected by the anode, with

$$u = \sqrt{\frac{e\phi_{AB}}{T_{eB}}} - \sqrt{\frac{m_e v_{xeB}^2}{2T_{eB}}}. \qquad (13)$$

Notice that $|g_{xeA}|$ recovers correctly the two asymptotic limits:

$$|g_{xeA}| = \sqrt{\frac{T_{eB}}{2\pi m_e}}n_{eB}\exp\left(-\frac{e|\phi_{AB}|}{T_{eB}}\right) \qquad (14)$$

for $|v_{xeB}| \ll \bar{c}_e$, and

$$|g_{xeA}| = |v_{xeB}|n_{eB} \qquad (15)$$

for $|v_{xeB}| \gg \bar{c}_e$.

A steady-state sheath must satisfy

$$|g_{xeA}| = |g_{xeB}| \equiv n_{eB}|v_{xeB}| \qquad (16)$$

and this condition determines the steady-state value of $\phi_{AB}$. Equations (12) and (16) yield

$$\sqrt{\pi}\sqrt{\frac{m_e v_{xeB}^2}{2T_{eB}}}\,(2 - \text{erfc } u) = \exp(-u^2) \qquad (17)$$

as the implicit function for $e\phi_{AB}/T_{eB}$ in terms of $v_{xeB}/\sqrt{T_{eB}/m_e}$.

This function is plotted in Fig. 2. Notice that $\phi_{AB}$ does not vanish except for $v_{xeB}(T_{eB}/m_e)^{-1/2} \to \infty$. In particular, $e\phi_{AB}/T_{eB} = 0.64$ and $0.24$ for

$v_{xeB} = \bar{c}_{eB}/4$ and $\sqrt{T_{eB}/m_e}$, respectively. At this last point the sheath potential changes from negative to positive, as we will see below. For a positive sheath, ions take the role of repelled species and the potential drop, $\phi_{AB} < 0$, is obtained from the ion flow properties. The preceding analysis and Fig. 2 are applicable if one just changes subscript $e$ for $i$.

## 3.2 Presheath model

In the present version, it includes all inertia terms on the electron dynamics, but, all aspects that are not essential for the plasma response near the anode, have been simplified. The simplified features are:

1. Zero plasma production.

2. Constant ion and electron temperatures.

3. Constant values of the electron gyromotion and collision frequencies, with $\nu_e \leq O(\omega_e)$.

Then, the quasineutral model consists of

$$g_{x\alpha} = n_e v_{x\alpha} = \text{const}, \quad \alpha = i, e, \tag{18}$$

$$(m_i v_{xi}^2 - T_i)\frac{1}{v_{xi}}\frac{dv_{xi}}{dx} = -e\frac{d\phi}{dx}, \tag{19}$$

$$(m_e v_{xe}^2 - T_e)\frac{1}{v_{xe}}\frac{dv_{xe}}{dx} = e\frac{d\phi}{dx} + m_e(\omega_e v_{\theta e} - \nu_e v_{xe}), \tag{20}$$

$$v_{xe}\frac{dv_{\theta e}}{dx} = -\omega_e v_{xe} - \nu_e v_{\theta e}. \tag{21}$$

Subscript B has been omitted for the constant magnitudes: $g_{x\alpha}$ $T_e$, $T_i$, $\omega_e$, and $\nu_e$. Notice that all these magnitudes (in particular the ion and electron fluxes) are inputs of the model, which is valid only in a limited region around the anode.

From Eq. (18) the two axial velocities are related by

$$\frac{v_{xi}}{v_{xe}} = \frac{g_{xi}}{g_{xe}} = \frac{I_{iB}}{I_d - I_{iB}} \sim \frac{I_{iB}}{I_d}. \tag{22}$$

Also, Eq. (19) yields a explicit expression for $\phi(v_{xi})$,

$$e\phi + \frac{1}{2}m_i v_{xi}^2 - T_i \ln v_{xi} = \text{const}. \tag{23}$$

Adding Eqs. (19) and (20), one has

$$\left[m_e v_{xe}^2 + m_i v_{xi}^2 - (T_e + T_i)\right]\frac{1}{v_{xe}}\frac{dv_{xe}}{dx} =$$
$$m_e(\omega_e v_{\theta e} - \nu_e v_{xe}) \tag{24}$$

which does not include the electric field. Using Eq. (22) to eliminate $v_{xi}$ in Eq. (24), it turns out

that Eqs. (21) and (24) constitute a closed set to determine $v_{xe}(x)$ and $v_{\theta e}(x)$. Once they are known, Eqs. (18), (22), and (23) yield $n_e(x)$, $v_{xi}(x)$, and $\phi(x)$.

Since $v_{xe}$ cannot become zero, Eqs. (21) and (24) state that the *only* singular point (which we identify with point B) of this plasma corresponds to

$$m_e v_{xeB}^2 + m_i v_{xiB}^2 = T_e + T_i. \tag{25}$$

This expression is the generalized Bohm condition for this plasma, and includes both $v_{xeB}$ and $v_{xiB}$. If both sides are multiplied by $n_{eB}$, it establishes that the total (ion plus electron) pressure and axial momentum flux coincide at the singular/sonic point B.

It is important to observe that, were $d\phi/dx$ an external electric field, Eqs. (19) and (20) would yield that the ion and electron flows present singular/sonic points at $v_{xi} = \sqrt{T_i/m_i}$ and $v_{xe} = \sqrt{T_e/m_e}$, respectively. However, when the electric field is self-adjusted by the quasineutral plasma, it acts as an additional pressure force and the above two points are just regular ones for the plasma flow. In particular, setting $v_{xi} = \sqrt{T_i/m_i}$ in Eq. (19), it just turns out that the electric field is zero.

Using Eq. (22) and the Bohm condition (25), the ion and electron axial velocities at point B satisfy

$$v_{xiB}^2 = \frac{Tg_{xi}^2}{m_i g_{xi}^2 + m_e g_{xe}^2},$$
$$v_{xeB}^2 = \frac{Tg_{xe}^2}{m_i g_{xi}^2 + m_e g_{xe}^2}, \tag{26}$$

where we call $T = T_e + T_i$.

There are three distinguished regimes:

$$\frac{g_{xi}}{g_{xe}} \gg \sqrt{\frac{m_e}{m_i}} : \ v_{xiB}^2 \simeq \frac{T}{m_i}, \ v_{xeB}^2 \ll \frac{T}{m_e}, \tag{27}$$

$$\frac{g_{xi}}{g_{xe}} \sim \sqrt{\frac{m_e}{m_i}} : \ v_{xiB}^2 \sim \frac{T}{m_i}, \ v_{xeB}^2 \sim \frac{T}{m_e}, \tag{28}$$

$$\frac{g_{xi}}{g_{xe}} \ll \sqrt{\frac{m_e}{m_i}} : \ v_{xiB}^2 \ll \frac{T}{m_i}, \ v_{xeB}^2 \simeq \frac{T}{m_e}. \tag{29}$$

Regime (27) corresponds to the classical diffusive limit for the electrons. Regime (29) represents the opposite situation: a negligible ion flux and plasma dynamics dominated by the electron flow, with Bohm condition determining $v_{xeB}$ mainly. Regime (28) represents the intermediate case with same order ion and electron kinetic energies.

Since $v_{xe} < 0$ and $v_{\theta e} > 0$, the right-hand-side of Eq.(24) never vanishes. As a consequence, point B is necessarily singular with

$$\frac{dv_{xi}}{dx}\Big|_B, \frac{dv_{xe}}{dx}\Big|_B, \frac{dn_e}{dx}\Big|_B, \to +\infty, \tag{30}$$
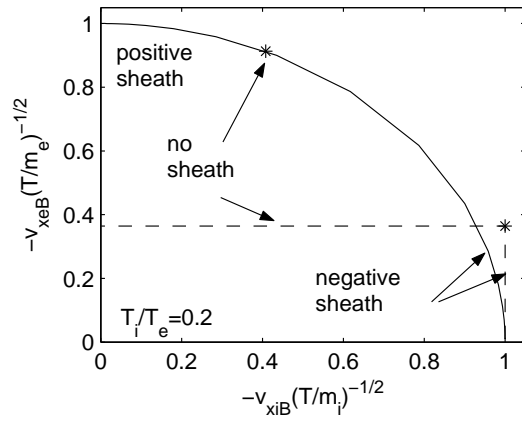
4

Figure 3: The parametric curve for the ion and electron axial velocities at the transition point B. The solid line corresponds to the present model. The dashed line is the model of Dorf et al., used by Rus and Ahedo too. Asterisks represent transition cases.

and

$$\left.\frac{d\phi}{dx}\right|_B \times \text{sign}(m_i v_{xiB}^2 - T_i) \to +\infty. \qquad (31)$$

These derivatives are infinite in the quasineutral scale, of the order of the Larmor radius,

$$l_e = (T_e/m_e)^{1/2}\omega_e^{-1}.$$

In fact, they are indicating the transition to the much smaller spatial scale of the sheath, where gradients are proportional to the inverse of the Debye length.

The sign of $d\phi/dx|_B$ determines whether the sheath is positive or negative. Thus, an important conclusion is that there is a *single no-sheath case* separating the negative- and positive- sheath regimes. It is characterized by

$$\frac{g_{xi}}{g_{xe}} = \sqrt{\frac{m_e T_i}{m_i T_e}}: \quad v_{xiB}^2 = \frac{T_i}{m_i}, \quad v_{xeB}^2 = \frac{T_e}{m_e}, \qquad (32)$$

and the electric field at the anode satisfies

$$e\left.\frac{d\phi}{dx}\right|_B = -\frac{T_i}{T_i + T_e}m_e(\omega_e v_{\theta eB} - \nu_e v_{xeB}). \qquad (33)$$

For the rest of the cases, the sheath potential drop can be obtained from Fig. 2.

## 3.3   Results

Figure 3 plots the parametric curve for the values of $v_{xi}$ and $v_{xe}$ at point B, Eq. (26), and indicates the regions of the negative and positive sheath regimes,

separated by the single no-sheath point. The dimensionless curve of Fig. 3 is universal; only the position of the no-sheath point depends on the value of $T_i/T_e$. The vertical part of the dashed line of Fig. 3 corresponds to the 'classical' negative-sheath model (i.e. $v_{xeB} \ll \sqrt{T/m_e}$) ordinarily used by Ahedo et al., whereas the horizontal part corresponds to the no sheath regime of Dorf et al.. The comparison shows that the negative-sheath model is basically correct for the parametric region where it is ordinarily used (that is, until the vicinity of the 'old' no-sheath limit).

Figure 4 depicts the evolution with the ion back-current of important plasma magnitudes at point B. For the computation of $\phi_{AB}$ the curve of Fig. 2 has been used; for $v_{\theta eB}$ the quasineutral model has been integrated for each value of the Hall parameter. The dashed lines represent the results for the model of Dorf et al., except for the plots of $v_{\theta eB}$, where they represent the diffusive limit, Eq. (2). For low enough ion currents, $v_{\theta eB}$ is bounded to the order of the electron thermal velocity, almost independently of the value of the Hall parameter. Indeed, the diffusive limit is less applicable near the anode the *larger* is the Hall parameter. The dependence of the sheath potential on the ion backcurrent (for $T_{iB}/T_{eB} \ll 1$) is given by Eq. (5) for a negative sheath with $|v_{xeB}| \ll \sqrt{T_{eB}/m_e}$, and by

$$\frac{e|\phi_{AB}|}{T_{iB}} = \frac{1}{2}\ln\left(\frac{m_e}{2\pi m_i}\frac{T_{iB}}{T_{eB}}\frac{I_d^2}{I_{iB}^2}\right) \qquad (34)$$

for a positive sheath with $|v_{xiB}| \ll \sqrt{T_{iB}/m_i}$.

Figure 5 illustrates the evolution of the spatial profiles of the plasma variables in the near-anode region, for different ion currents to the anode, covering both the negative and positive sheath regimes; dashed lines represent the no-sheath case and $l_e$ is the electron gyroradius. The profiles of the electric potential present a maximum where $v_{xi} = -\sqrt{T_i/m_i}$, Eq. (19). As $|v_{xiB}|$ decreases from $\sqrt{T/m_i}$, this maximum moves toward the anode and disappears finally in the positive sheath regime. Notice that the electron velocities do not vary much within the positive sheath regime.

As $T_i/T_e$ decreases the parametric interval of the positive sheath regime is reduced, and the spatial profiles within that regime become more flat. With respect to the effect of the Hall parameter, it affects only $v_{\theta e}$ as long as $\omega_e/\nu_e \gg 1$. The interesting case of a Hall parameter which is large far from the anode and small near the anode [2], needs a separate study.

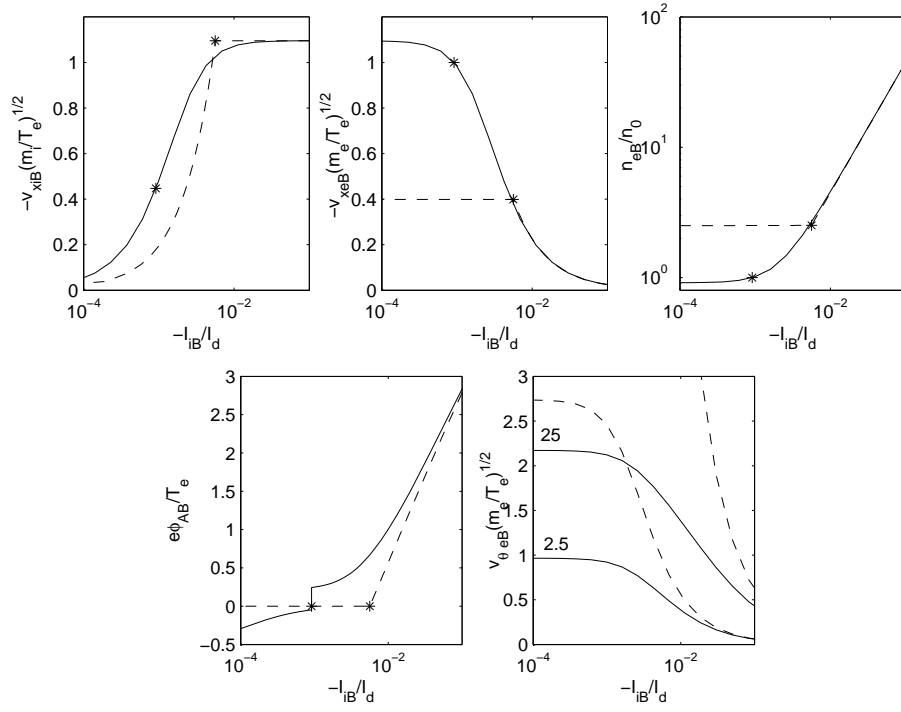For a negative sheath and $|v_{xeB}| \ll \sqrt{T_e/m_e}$, the presheath/sheath problem is equivalent to the

Figure 4: Evolution with the ion back-current of plasma parameters at the anode sheath; $n_0 = I_d/eA_c\sqrt{T_e/m_e}$. The temperature ratio is $T_i/T_e = 0.2$. The computations of $v_{\theta eB}$ are for $\omega_e/\nu_e = 2.5$ and $25$. Dashed lines represent the model of Dorf et al., except for $v_{\theta eB}$, where they represent the diffusive limit. Asterisks mark transition points.
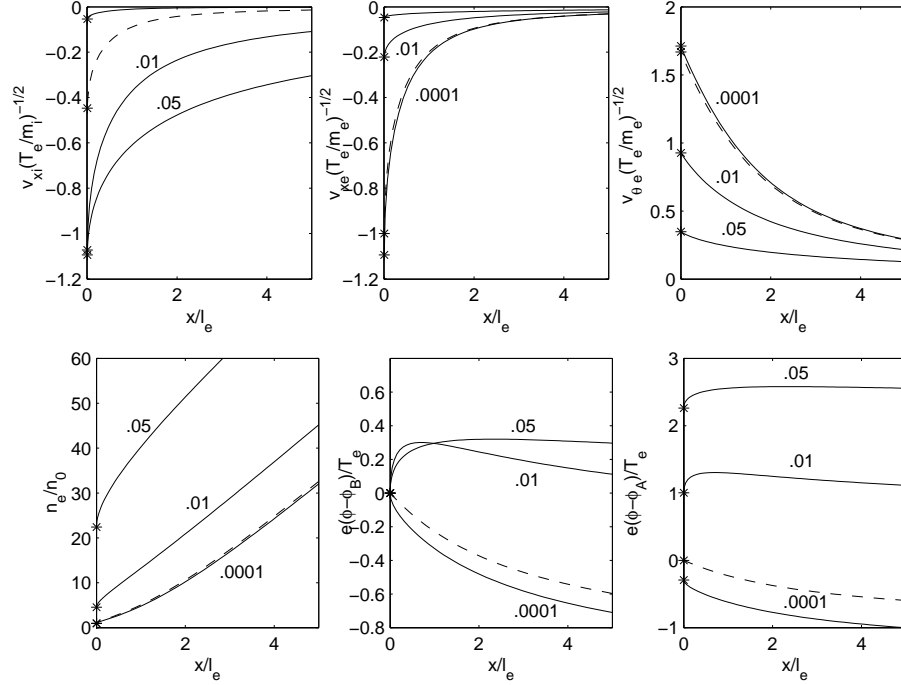


Figure 5: Different plasma profiles for $\omega_e/\nu_e = 10$, $T_i/T_e = .2$, xenon, and several values of the relative ion backcurrent: solid lines correspond to $-I_{iB}/I_d = 0.05$, $0.01$, and $0.0001$; dashed lines represent the no-sheath case ($-I_{iB}/I_d \simeq 0.009$). Asterisks correspond to point B.

6

standard one of the plasma-wall interaction in an unmagnetized medium (since the attracted species is unmagnetized). For a positive sheath and $|v_{xiB}| \ll \sqrt{T_i/m_i}$, the problem reduces to a standard one again, that of the plasma-wall interaction for a magnetic field parallel to the wall. This problem was treated in detail by Ahedo [7] for a planar geometry, but the extension to the present geometry is automatic. An asymptotic solution for the presheath and $\omega_e/\nu_e \gg 1$ was derived; see Fig. 5 of Ref. [7]. The solution distinguishes between a 'far' diffusive region and a 'near' inertial region. Also, for $\omega_e/\nu_e \gg 1$, it yields

$$\frac{v_{\theta eB}}{\sqrt{T_e/m_e}} \simeq \sqrt{2\ln(\omega_e/\nu_e)}, \qquad (35)$$

confirming that $v_{\theta eB}$ is bounded to the order the electron thermal velocity, and

$$L_{pre} \sim [2\ln(\omega_e/\nu_e)]^{-1/2} l_e \qquad (36)$$

for the characteristic gradient length of the presheath, $L_{pre}$.

A feature not considered in either Ref. [7] or the present model, are ionization effects. For an ionization frequency, $\nu_i$, much smaller than $\omega_e$, ionization is important already in the near-anode region for

$$|I_{iB}|/I_d \leq O(\nu_i/\omega_e). \qquad (37)$$

Formally, $v_{xiB} = 0$ never becomes zero since this would imply $e|\phi_{AB}|/T_{iB} \to \infty$ in Eq. (34). In practice, the parametric interval for the positive sheath regime can be very narrow.

## 4    Conclusions

A new model of the near anode region that covers the whole regimes of negative and positive sheaths has been derived. The classical formulation of the negative sheath regime, which corresponds to the normal operation regime of a Hall thruster, continues to be valid, but there is not a no-sheath regime. The sheath transition is determined by a generalized Bohm condition which relates the total (ions plus electrons) kinetic and thermal energies of the plasma.

The complete integration of the discharge equations from anode to cathode, with inclusion of electron inertial effects and the correct conditions at the anode sheath, remains to be done. This can be a hard-to-solve problem if we take into account the numerical difficulties pointed out by Rus and Ahedo with respect to the electron equations.

From the results of Rus and Ahedo, we expect the positive sheath regime to be small and to correspond to low values of the discharge voltage. It is more unclear whether this regime will be ill-defined in terms of control parameters.

## Acknowledgments

## References

[1] L. Dorf, V. Semenov, Y. Raitses, and N.J. Fisch. Hall thruster modeling with a given temperature profile. In *38th Joint Propulsion Conference, Indianapolis, IN*, AIAA 2002-4246. American Institute of Aeronautics and Astronautics, Washington, DC, 2002.

[2] L. Dorf, V. Semenov, and Y. Raitses. Anode sheath in Hall thrusters . *Applied Physics Letters*, 83(13):2551 − 2553, 2003.

[3] E. Ahedo, P. Martínez-Cerezo, and M. Martínez-Sánchez. 1-D performance analysis of a Hall thruster. In *SP-465: 3rd Spacecraft Propulsion Conference, Cannes (France)*, pages 323–330, Noordwijk, The Netherlands, 2000. European Space Agency.

[4] E. Ahedo, J.M. Gallardo, and M. Martínez-Sánchez. Model of the plasma discharge in a Hall thruster with heat conduction. *Physics of Plasmas*, 9(9):4061–4070, 2002.

[5] E. Ahedo, J.M. Gallardo, and M. Martínez-Sánchez. Effects of the radial-plasma wall interaction on the axial Hall thruster discharge. *Physics of Plasmas*, 10(8):3397–3409, 2003.

[6] J. Rus and E. Ahedo. A no-anode-sheath regime of the Hall thruster discharge. In *SP-555: 4th Spacecraft Propulsion Conference, Sardinia (Italy)*, Noordwijk, The Netherlands, 2004 (to be published). European Space Agency.

[7] E. Ahedo. Structure of the plasma-wall interaction in an oblique magnetic field. *Physics of Plasmas*, 4:4419–4430, 1997.